OUKA
The University of Osaka
Institutional Knowledge Archive

Title	Structural basis for the reaction mechanism and mechanism of escaping from product inhibition in heme oxygenase
Author(s)	杉島, 正一
Citation	大阪大学, 2004, 博士論文
Version Type	VoR
URL	https://hdl.handle.net/11094/1509
rights	
Note	

The University of Osaka Institutional Knowledge Archive : OUKA

https://ir.library.osaka-u.ac.jp/

The University of Osaka

理学9557

Structural basis for the reaction mechanism and mechanism of escaping from product inhibition in heme oxygenase

(ヘムオキシゲナーゼの反応機構と反応物阻害回避機構に関する構造生物学的研究)

Doctoral thesis

Masakazu Sugishima

February 2004

Graduate School of Science

Osaka University

Structural basis for the reaction mechanism and mechanism of escaping from product inhibition in heme oxygenase

(ヘムオキシゲナーゼの反応機構と

反応物阻害回避機構に関する構造生物学的研究)

Doctoral thesis

Masakazu Sugishima

February 2004

Graduate School of Science

Osaka University

Abbreviations

biliverdin(Fe); biliverdin IXα-iron chelate

biliverdin(Fe)-HO; HO in complex with biliverdin(Fe)

CN^--heme-HO; heme-HO bound to cyanide

CO-heme-HO; heme-HO bound to carbon monoxide

CPR; NADPH-cytochrome P450 reductase

cyt b_5; cytochrome b_5

cyt b_{562}; cytochrome b_{562}

ENDOR; electron nuclear double resonance

ESR; electron spin resonace

Hb; hemoglobin

heme-HO; HO in complex with heme

HO; heme oxygenase

N_3^--heme-HO; heme-HO bound to azide

NO-heme-HO; heme-HO bound to nitric oxide

Mb; myoglobin

OEB; octaethylbilindione

RR; resonance Raman

sGC; soluble form of guanylate cyclase

Contents

General introduction

Physiological functions of HO

Iron is a crucial element for a vast number of cellular processes, including ATP generation (respiratory chain), oxygen transport (Hb), and detoxification (cytochrome P450). It has functions within heme or iron–sulfur clusters, or directly bound to proteins. Disorders of iron metabolism are quite common in the human population, for instance, anemia caused by the dietary iron deficiency. Normally in humans, about 1 mg of iron is supplied from foods, and at the same time an equal amount is eliminated from the body. Remarkably, this dietary iron accounts for only 1–3% of the needs of iron. Most of that is provided from the degradation of free heme, which is mainly produced by the degradation of senescent erythrocytes. Heme oxygenase (HO, EC 1.14.99.3), which was firstly purified and

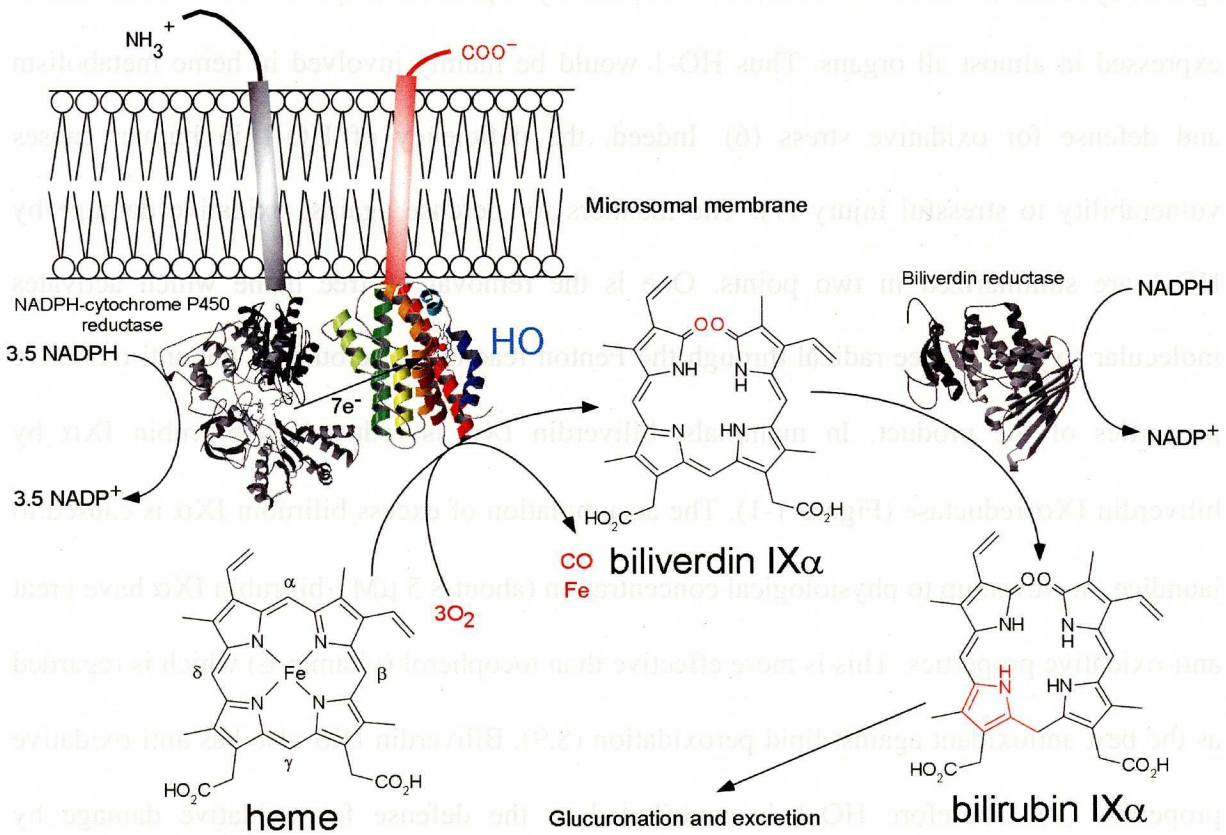

Figure 1-1. **Heme degradation pathway in mammals.**
The porphyrin ring of heme is oxidatively cleaved by HO, producing biliverdin, iron, and CO. Biliverdin is further converted to bilirubin by biliverdin reductase. Bilirubin is conjugated with glucronic acid by UDP-glucuronyl transferase to increase its solubility and then excreted into the bile.

characterized by Tenhunen *et al.* from the microsomal fraction of rat liver and spleen (1,2), plays a central role in the heme degradation pathway (Figure 1-1) (3). Iron recovered by HO would follow detoxification pathways involving either sequestration by ferritin or extracellular efflux by transferrin and lactoferrin. The most important fuction of HO is the iron homeostasis.

Moreover, two major functions of HO in mammals have been recently proposed; the defense for oxidative stress and the production of CO as a signaling molecule (Figure 1-2). Two isozymes are known in mammals; HO-1 (33 kD) and HO-2 (36 kD), both of which catalyze the same reaction and its mechanism is identical (4), whereas their inducibility and organic specifity of expression differ. HO-1 is highly inducible by its substrate, heme, and various non-heme substances such as heavy metals, bromobenzene, endotoxin, oxidizing agents, cytokines, NO, and UVA (5). HO-1 is mainly expressed in spleen and liver, but this is expressed in almost all organs. Thus HO-1 would be mainly involved in heme metabolism and defense for oxidative stress (6). Indeed, the deficiency of HO-1 in human causes vulnerability to stressful injury (7). The manners for defense against oxidative damage by HO-1 are summarized in two points. One is the removal of free heme which activates molecular oxygen to free radical through the Fenton reaction. The other is the anti-oxidative properties of the product. In mammals, biliverdin IXα is reduced to bilirubin IXα by biliverdin IXα reductase (Figure 1-1). The accumulation of excess bilirubin IXα is caused to jaundice, however, up to physiological concentration (about 8.5 μM), bilirubin IXα have great anti-oxidative properties. This is more effective than tocopherol (vitamin E) which is regarded as the best antioxidant against lipid peroxidation (8,9). Biliverdin IXα also has anti-oxidative properties (9). Therefore HO-1 is contributed to the defense for oxidative damage by removing free heme, pro-oxidant, and producing bilirubin IXα and biliverdin IXα, anti-oxidant.

In addition to the iron homeostasis and defense for oxidative stress, the functions via CO, by-product of HO reaction, are supposed for HO-1 that vasodilation, anti-platelet aggregation, anti-proliferation, anti-apotopsis, and inhibition of pro-inflammatory cytokine production (10,11). Only HO reaction is the known source of endogeneous CO. The molecular target of CO is unknown, but two canditates are proposed (Figure 1-2). One is the soluble form of guanylate cyclase (sGC), which is activated by NO binding to the heme moiety (12). CO can also bind to heme in sGC and can activate although this effect is very small compared to NO *in vitro*. However, it was recently reported that YC-1, which is a small artificial compound and has similar structure to biliverdin, can activate sGC bound to CO comparable to NO (13). Biliverdin and bilirubin don't have such property, but the unknown compound modified from biliverdin may promote the activation of sGC by CO. Another target for CO is p38 mitogen activating protein kinase signaling pathway where CO affects to the anti-inflammation and anti-apoptosis although the direct target involved in this patyway is unknown (10).

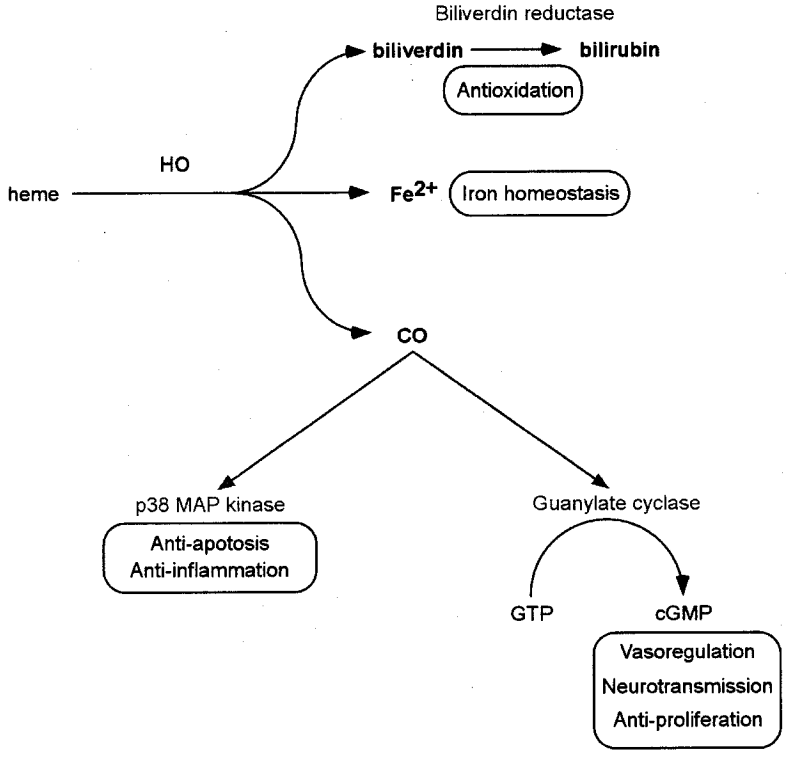

Figure 1-2. **Summary of physiological functions of HO products.** The products of HO, biliverdin, Fe^{2+}, and CO, are involved in several physiological functions. Fe^{2+}; Iron homeostasis. Biliverdin and bilirubin; Antioxidation. CO; second messenger for several reactions.

HO-2, constitutively expressed in nerve cell and testis, would also function to produce CO as a signalling molecule in neuron. But its target is also unknown. In plants and cyanobacteria, HO functions to synthesize biliverdin, which is a precursor of open-chain tetrapyrrol chromophores, such as phycobilins and phytochromobilins (14). In some pathogenic bacteria, HO is involved in iron supply from host (15).

Reaction scheme of HO

One cycle of HO reaction (Figure 1-3, (16-25)) consists of three sequential steps of heme oxidation utilizing molecular oxygen and reducing equivalents from NADPH-cytochrome P450 reductase (CPR), in mammals (1,26), or ferredoxin, in plants and cyanobacteria (27). In this reaction, heme acts as co-factor activating O_2 as well as substrate.

The notable features of HO reaction are classified into three categories. One is the activation mechanism of molecular oxygen bound to the heme iron. Spectroscopic features of heme-HO are similar to Mb rather than cytochrome P450, indicative that the electronic structure of heme is simiar to that of Mb (28-31). As well known, Mb does not activate O_2, only binds O_2. How does heme-HO activate O_2? The mechanism of O_2 activation is well studied in cytochrome P450; the mechanism, so called "push-pull" mechanism, is the combination of electron donation from the proximal ligand (thiol group in cytochrome P450) and charge-relay system from O_2 to water and distal residues (Figure 1-4) (16). In this mechanism, O=O bond is heterolitically cleaved and oxyferryl species is produced. Similar mechanism is also believed in peroxidase and other heme containing monooxygenase (16). But in HO, oxyferryl species is not produced in the reaction and ferric hydrogen peroxide is active species in HO reaction (Figure 1-3).

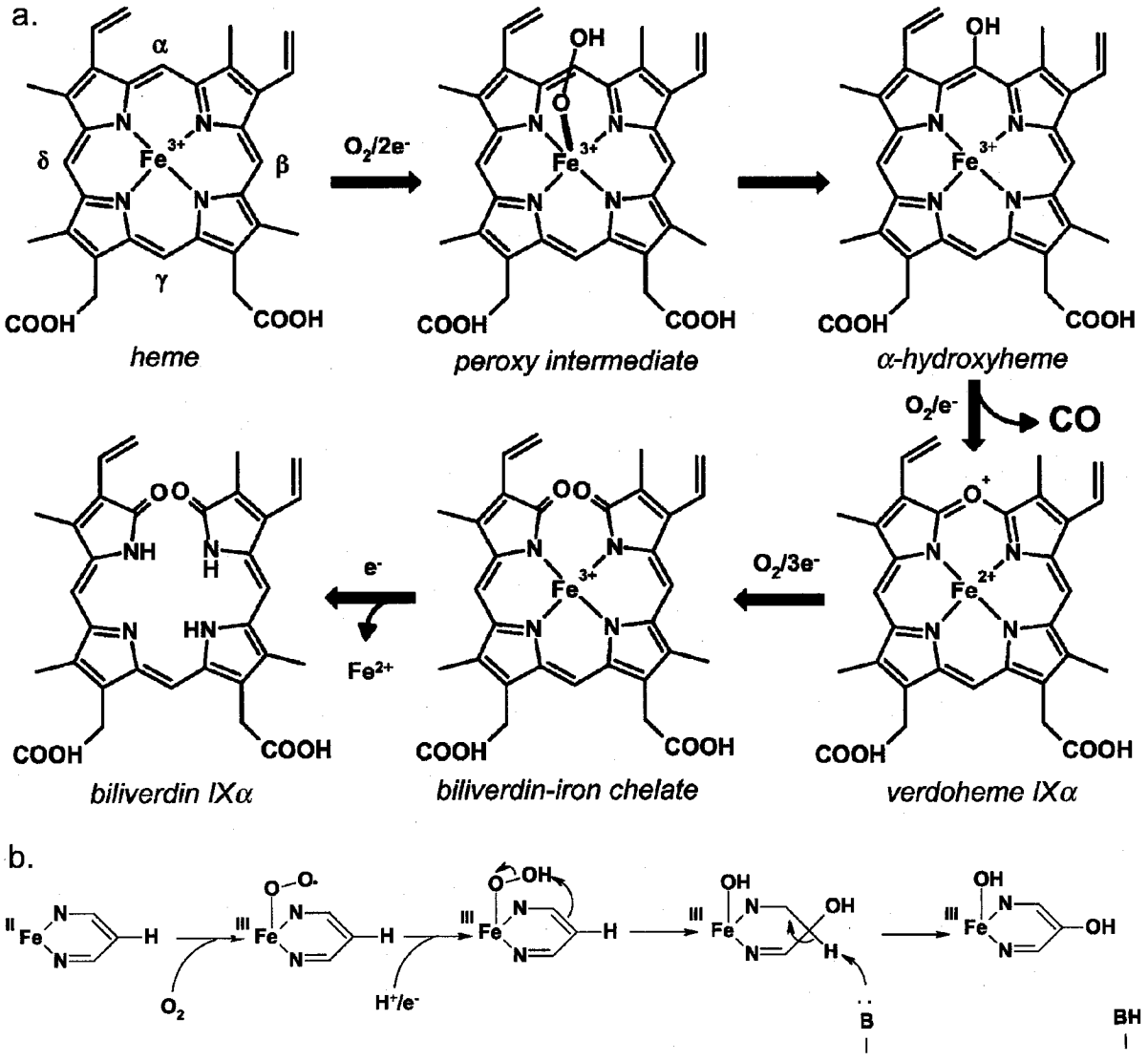

Figure 1-3. **Reaction scheme of HO.**

a. In the first step, heme bound to HO is hydroxylated at the α-*meso* carbon, yielding α-hydroxyheme. In this reaction step, molecular oxygen bound to heme iron is activated to ferric hydrogen peroxide. The second step is the conversion of α-hydroxyheme to verdoheme IXα with the concomitant release of the α-*meso* carbon as CO. Lastly, the oxygen bridge of verdoheme IXα is cleaved, producing biliverdin IXα-iron chelate. Ferrous iron ion is smoothly released by the reduction of biliverdin IXα-iron chelate, then biliverdin IXα is released from HO. b. Schematic diagram of the proposed hydroxylation mechanism of heme, the first step of HO reaction. Around the α-*meso* carbon of heme is shown for clarity. The π electrons of porphyrin ring are directly donated to hydrogen peroxide bound to the heme iron, then the α-*meso* carbon of heme is hydrolylated. Thus it is required to achieve the regispecific reaction that the hydrogen peroxide bound to heme iron is directed to the α-*meso* carbon and the π electrons of porphyrin ring are localized at the double bond including the α-*meso* carbon.

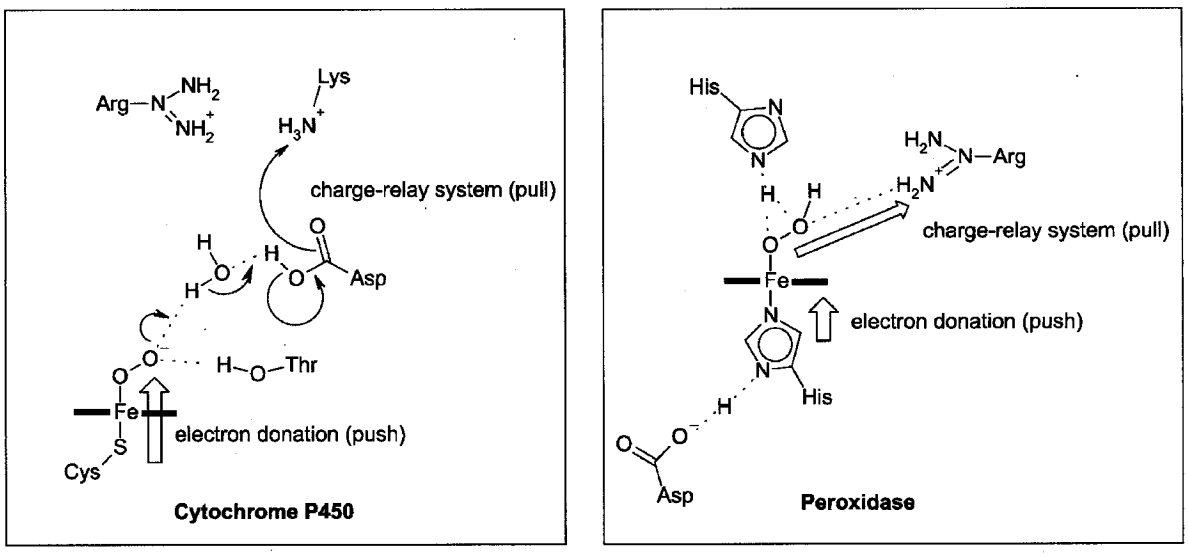

Figure 1-4. **Reaction mechanism proposed in cytochrome P450 and peroxidase**

Second notable feature is the regiospecificity of the reaction. The regiospecificity of HO reaction would be physiollogically important because only bilirubin IXα, last product of HO-biliverdin reductase system, is hydrophobic although other isomers, bilirubin IXβ, IXγ, and IXδ, are hydrophilic. Hydrophilic groups of bilirubin IXα form intramolecular hydrogen-bonds, thus these groups cannot be hydrated. Considering the proposed hydroxylation mechanism of heme (Figure 1-3b), the regiospecific oxidation of heme would be achieved by two factors; the direction of O_2 bound to heme iron and the localization of π-electron at the double bond including the α-*meso* carbon. The locallization of electron is suggested on the basis of the HO reactions of the chemically modified hemes (32,33) but the direction of the distal ligand was unknown.

Third feature is the discrimination between O_2 and CO. In general, CO is a competitive inhibititor of O_2 binding to heme iron because CO strongly binds to the ferrous heme iron rather than O_2 does. In case of Mb, the affinity of CO is 30~100 fold greater than that of O_2 affinity (34). O_2 must bind to heme-HO where CO produced in HO reaction is locally concentrated. To overcome this dilemma, the affinity of O_2 to heme-HO is increased and that

of CO is suppressed (35), however, this molecular mechanism was unknown.

Crystal structure of rat ferric heme-HO-1

In my master's course, I prepared rat ferric heme-HO-1 complex and determined its crystal structure (36). I summarize here the results as the background of this thesis. Rat HO-1 consists of 289 amino acids and has a hydrophobic membrane-binding domain at the C-terminus. Recombinant rat HO-1, in which the C-terminal membrane-spanning region had been truncated, was expressed in *E. coli* JM109 and purified (figure 1-5, (37-39)). The truncated rat HO-1 shows an activity identical to that of native HO-1 using NADPH-cytochrome P450 reductase as sodium ascorbate for reductants. All HO described in this thesis is this truncated HO-1. Truncated HO-1 in complex with heme was crystallized in the condition that PEG 4000 was used for precipitant (38).

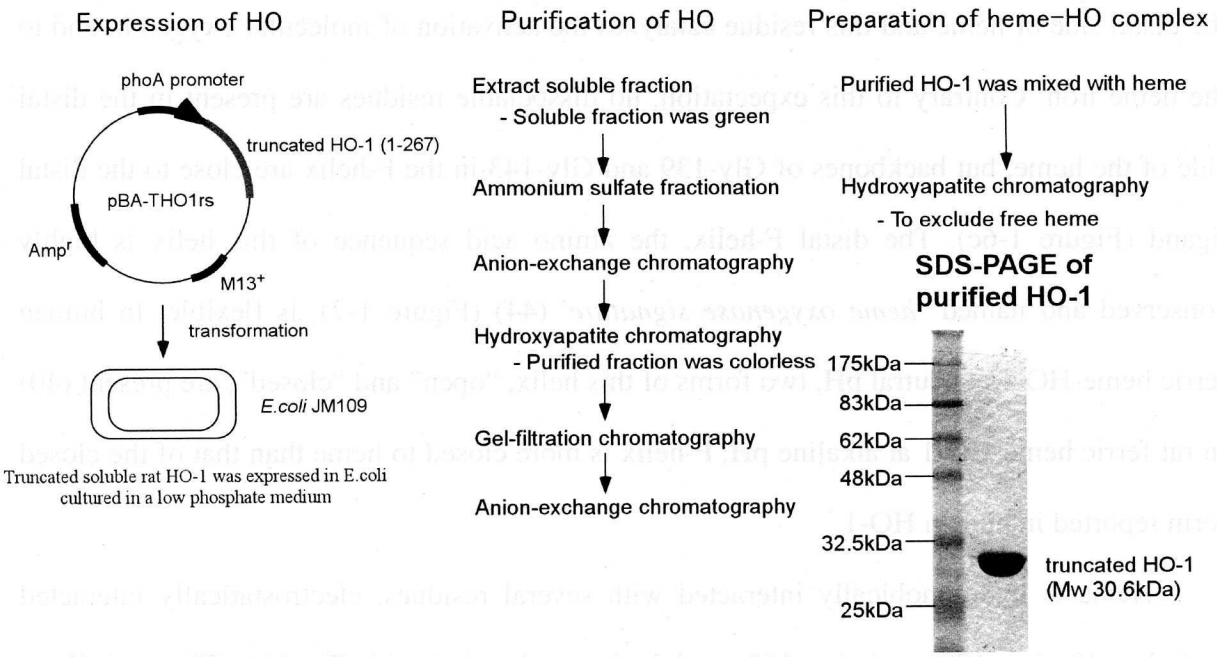

Figure 1-5. **Expression and purification of rat HO-1.**
Truncated rat HO-1 was expressed in *E. coli* JM109 and purified using ammonium sulfate fractionation and chromatography techniques using anion-exchange (Q sepharose HP, Amersham Biosciences, and POROS HQ, Applied Biosystems), hydroxyapatite (CHT typeI, Bio-Rad Laboratories), and size-exclusion (Sephacryl S-200 HR, Amersham Biosciences) columns. Heme-HO complex was prepared by leaving the mixture solution of hemin and HO for one hour on ice and purified using hydroxyapatite column.

The determined sturucture has a novel folding, consisting of eight helices, A through H. The heme is sandwiched between the proximal helix, A (Leu-13~Glu-29), and distal kinked helix, F (Leu-129~Met-155) (Figure 1-6a) (36). Poulos *et al.* also determined the crystal structures of ferric heme-HO complexes of human (40) and *Neisseria meningitidis* (41) which are simlar to rat heme-HO structure.

The side-chain of His-25 in the A-helix serves as the proximal heme ligand, as predicted by spectroscopic and site-directed mutagenesis analyses (42,43). Proximal histidine in heme-HO is neutral as in Mb on the basis that the spectroscopic characters of heme-HO is similar to that of Mb (28-31). Neutral histidine cannot donate electron strongly to the distal side of the heme. This is one of the differences between HO and cytochrome P450 or peroxidase; cysteine or acidic histidine, which can donate electron, serves as the proximal ligand (Figure 1-4). Before the crystal structure was determined, it was predicted based on the "push-pull" mechanism (Figure 1-4) that the dissociable residues as histidine are located in the distal side of heme and this residue catalyzes the activation of molecular oxygen bound to the heme iron. Contrary to this expectation, no dissociable residues are present in the distal side of the heme, but backbones of Gly-139 and Gly-143 in the F-helix are close to the distal ligand (Figure 1-6c). The distal F-helix, the amino acid sequence of this helix is highly conserved and named '*heme oxygenase signature*' (44) (Figure 1-7), is flexible. In human ferric heme-HO-1 at neutral pH, two forms of this helix, "open" and "closed", are present (40). In rat ferric heme-HO-1 at alkaline pH, F-helix is more closed to heme than that of the closed form reported in human HO-1.

Heme is hydrophobically interacted with several residues, electrostatically interacted with Lys-18, Lys-179, and Arg-183, and hydrogen-bonded with Tyr-134 (Figure 1-6b,c). These interactions would determine the orientation of heme binding. Indeed, the R183D and R183E mutants altered the regiospecificity of HO reaction (45).

Although the crystal structures of these heme-HO complexes gave significant insights in

the enzymatic reaction, detailed reaction mechanism as well as characteristic features of HO reaction remained to be clarified. That is, how does HO incorporate substrates and release products? How does HO achieve the regiospecificity of the reaction? How is O_2 incorporated in verdoheme in the presence of CO produced in the previous step? To answer these questions, I started the crystallographic studies of various reaction intermediates of HO, which include an unstable intermediate induced by the laser irradiation at cryogenic temperature. Aside from the crystallographic studies, I incorporated molecular dynamics simulation to see the migration of the produced CO in the hemepocket of HO and RR spectroscopy to characterize the novel ligand binding mode to the heme iron, with which the crystallographic results were substantiated.

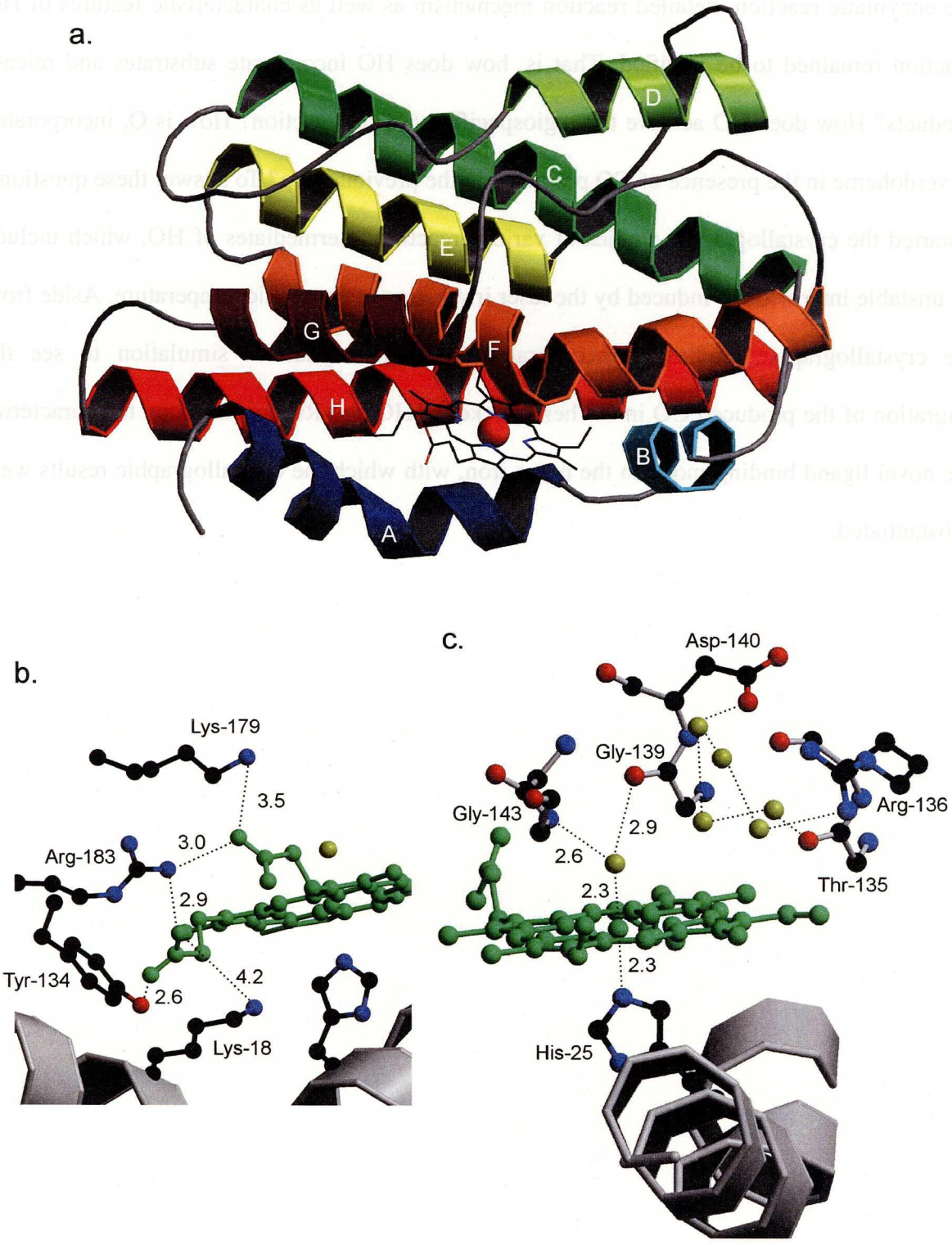

Figure 1-6. **Crystal structure of rat ferric heme-HO-1 complex**
a. Ribbon diagram of ferric heme-HO-1 complex. b. Electrostatic and hydrogen-bond interactions of heme propionates. Heme and water were colored green and yellow, respectively. Dashed lines indicate electrostatic and hydrogen-bond interactions of heme propionates and numerals indicate distances of interacted atoms. c. The structure of distal side of heme. Dashed lines indicates interactions of heme iron, its ligands, fixed water molecules in distal hemepocket, and HO residues. These figures were prepared with MOLSCRIPT (125) and RASTER3D (126).

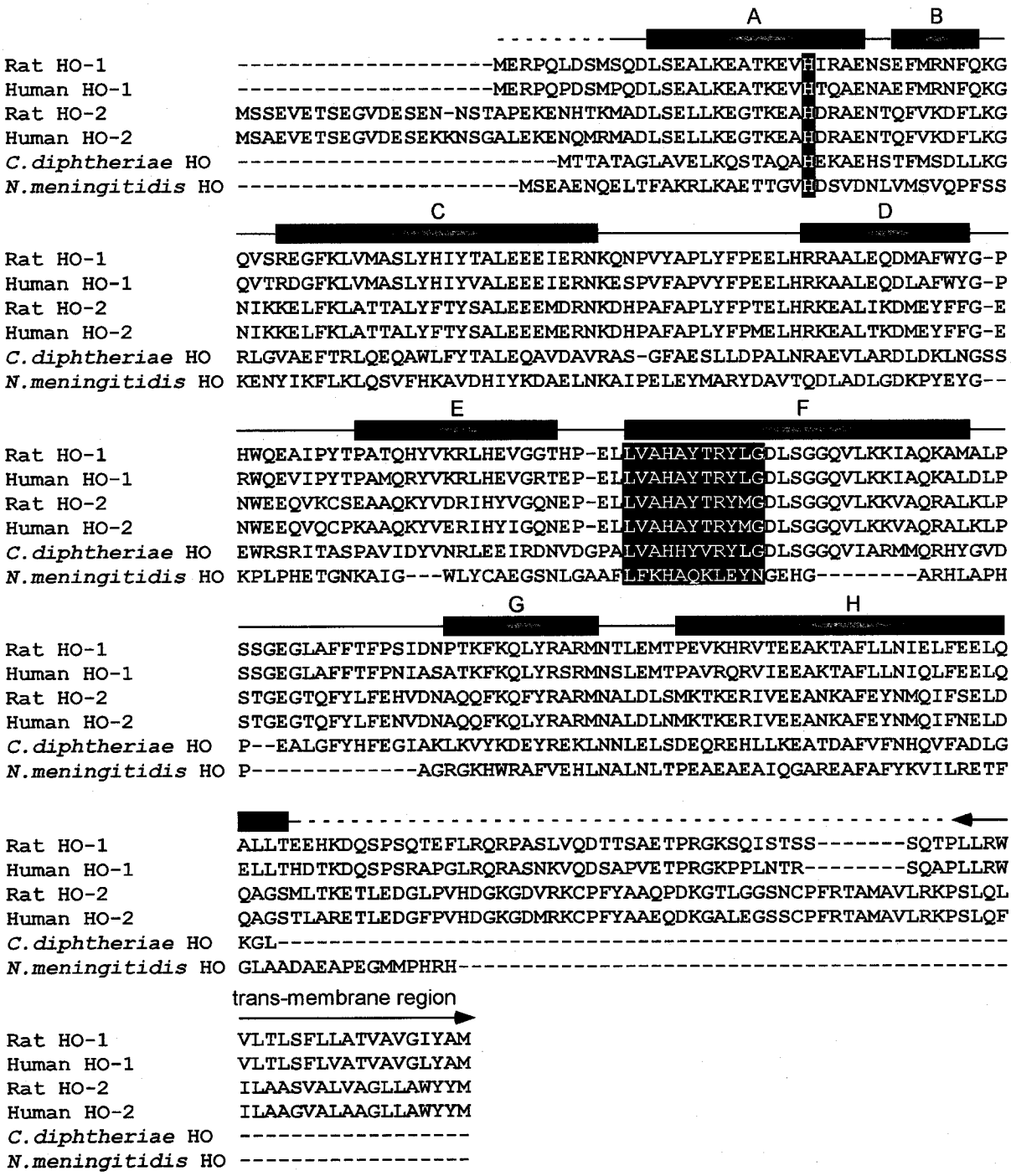

Figure 1-7. **Amino acid sequence alignment of mammalian HO-1 and HO-2, *Corynebacterium diphtheriae* HO, and *Neisseria meningitidis* HO.** Residues highlighted in black are the proximal ligand of heme and the conserved motif, "*heme oxygenase signature*" (consensus pattern; LXAHXYXXYXG), which is not conserved in *N. meningitidis* HO. Gray boxes, black lines, and broken lines indicate α-helices, loops, and disordered regions in rat heme-HO-1, respectively. Arrow indicates the trans-membrane region of mammalian HO.

Chapter 1

Structural basis for the reaction mechanism of HO

INTRODUCTION

As described in the general introduction, notable features of HO reaction are classified into three categories; activation mechanism of O_2 bound to the heme iron, regiospecificity of the reaction, and discrimination between O_2 and CO. This chapter deals with the whole steps of HO reaction including substrate binding and product release.

In the first section, I discuss the substrate incorporation mechanism based on the structural comparison between apo and heme-HO. The incorporation of heme into apoproteins is indispensable for hemoproteins to acquire biological functions. Although most hemoproteins are unstable in the apo-state, such proteins as myoglobin (Mb), cytochrome b_5 (cyt b_5), and cytochrome b_{562} (cyt b_{562}) are partially unfolded, yet they have stable secondary and tertiary structures in their apo-state. In solution these apoproteins can be analyzed by various spectroscopic methods, therefore they are often used as models in studies of heme binding and of protein folding (46-48). HO is not a hemoprotein by nature, but once it binds heme, it behaves like a hemoprotein. The heme-HO complex activates molecular oxygen and accepts reducing equivalents from CPR as heme-containing monooxygenases. It also has spectroscopic features similar to those of Mb (28-31). As described in general introduction, ferric heme-HO primarily consists of α-helices as do many other hemoproteins. Furthermore, HO-1 (33 kD) is larger than sperm whale Mb (17 kD), rat microsomal cyt b_5 (15 kD), and *E. coli* cyt b_{562} (14 kD). Clarification of the structure of apoHO should lead to an understanding of the structures of other hemoproteins. In particular, it should help clarify the structural changes caused by heme binding.

In the second section, I discuss the activation mechanism of O_2 and the structural basis

of the regiospecific hydroxylation based on the structure of N_3^--heme-HO, as an analog of hydrogen peroxide bound form. The HO reaction pathway consists of three sequential oxidation steps utilizing molecular oxygen and reducing equivalents from CPR (19,49). As shown in figure 1-3, the molecular oxygen coordinated to the ferrous heme iron is believed to direct its distal oxygen atom toward the α-*meso* carbon of the heme, and electrophilic addition of the protonated distal oxygen onto the α-*meso* carbon proceeds (17). Chemical studies using various peroxides as substrates of heme-HO show that the acitive oxygen species is not oxo-ferryl (Fe^{4+}=O), as in the cytochrome P450 reactions, but ferric-hydroperoxide (17,18). This scheme requires stereochemical conditions under which the molecular oxygen bound to heme iron is highly bent and directed toward the α-*meso* carbon of the heme. RR spectroscopic analysis has given an angle of nearly 110° for Fe^{2+}·· O-O (50), but the direction of the O-O bond about the Fe^{2+}·· O axis has not been determined. Azide is known to inhibit HO catalysis (2). On azide addition to ferric heme-HO, low-spin shift of the Soret band in the optical spectrum occurs (29,51), indicative that azide coordinates to the ferric heme iron. In the case of Mb, binding mode of azide is similar to that of molecular oxygen (52). It would be conceivable that N_3^--heme-HO is more suitable to a model of hydrogen peroxide bound heme-HO rather than that of O_2 bound heme-HO because the redox state of heme iron of N_3^--heme-HO is same as that of hydrogen peroxide bound heme-HO. The direction of hydrogen peroxide bound to heme-HO is essential for understanding the regiospecific oxidation catalyzed by HO. I therefore determined the crystal structure of N_3^--heme-HO as a mimic of hydrogen peroxide bound form.

In the third section, I discuss the product release mechanism based on the structure of the biliverdin-iron chelate bound form (Figure 1-3a). Although major progress has recently been made in understanding the nature of the first hydroxylation of heme, the mechanisms for the subsequent steps have been still unclear. The final step is known to require O_2 and

reducing equivalents (17,53). It is believed that the reaction mechanism of the final step is similar to that of first hydroxylation step (Figure 1-3b) (54,55), but there is no direct evidence supporting the mechanism in the final step. Furthermore little is known about the mechanism whereby biliverdin is produced from verdoheme and finally released from the enzyme. For further investigation of the HO reaction mechanism, I determined the structure of the biliverdin-iron chelate bound form. In addition, when the crystals of the biliverdin-iron chelate bound form were prepared, HO reaction could be proceeded in the crystal by adding chemical reductant, indicating that HO keeps its activity even in the crystal.

1.1 Heme binding mechanism based on the structure of apoHO

ABSTRACT

HO (apoHO) was crystallized as twinned $P3_2$ with three molecules in an asymmetric unit, and its crystal structure determined at 2.55 Å resolution. Structural comparison of apoHO and its complex with heme (ferric heme-HO) showed three distinct differences. First, the A-helix of the eight α-helices, A-H, in heme-HO, which includes the proximal ligand of heme (His-25), is invisible in apoHO. In addition, the B-helix, a portion of which builds the hemepocket, is shifted toward the heme pocket in apoHO. Second, Gln-38 is shifted toward the position where the α-*meso* carbon of heme is located in ferric heme-HO. Gln-38 Nε is hydrogen-bonded to the carbonyl group of Glu-29 located at the C-terminal side of the A-helix in ferric heme-HO, indicative that this hydrogen bond restrains the angle between the A- and B-helices in ferric heme-HO. Third, the amide group of Gly-143 in the F-helix is directed outward from the heme pocket in apoHO, whereas it is directed toward the distal ligand of heme in ferric heme-HO. This means that the F-helix around Gly-143 must change its conformation to accommodate heme binding. The apoHO structure has the characteristic that the helix on one side of the heme pocket fluctuates, whereas the rest of the structure is similar to that of heme-HO, as observed in such hemoproteins as myoglobin and cytchromes b_5 and b_{562}. These structural features of apoHO suggest that the orientation of the proximal helix and the position of His-25 are fixed upon heme binding.

MATERIALS AND METHODS

Crystallization of apoHO. Truncated rat HO-1 (Met-1~Pro-267) was expressed and purified as described in the general introduction (Figure 1-5, (37,38)). I screened the crystallization conditions of apoHO using Crystal Screen Kit (Hampton Research) with hanging-drop vapor-diffusion method at 277 K. The protein solution was mixed with an equal volume of each reservoir solution and equilibrated against each reservoir solution. Crystals of apoHO were obtained when a reservoir solution containing 2 M ammonium sulfate, 2% PEG 400, 5 mM strontium chloride, and 0.1 M HEPES-NaOH buffer (pH 8.0) was used. The protein concentration used for the crystallization was 20 mg ml^{-1} in 20 mM Tris-HCl buffer (pH 7.4) containing about 50 mM KCl. Rod-shaped crystals appeared after one day and grew to maximum size in five days (Figure 2-1).

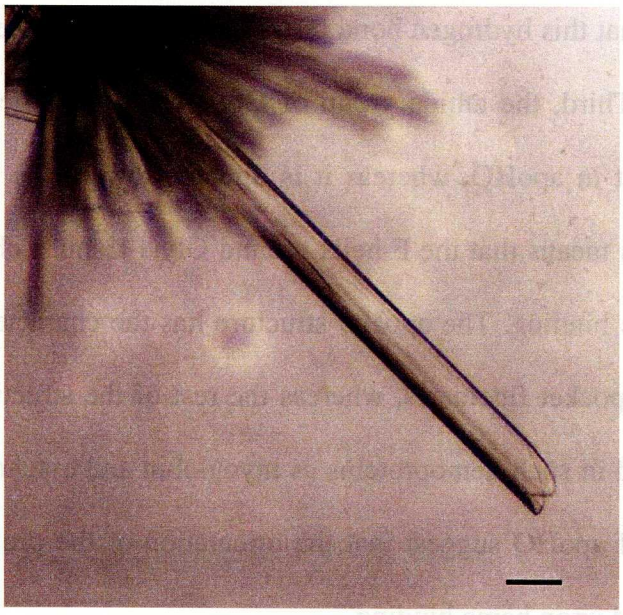

Figure 2-1. **ApoHO crystals.** Scale bar indicates 100 μm length.

Data Collection and Processing. For cryogenic data collection of the apoHO crystal, it was transferred to the artificial mother liquors, to which ethylene glycol was added to 12% (w/v). The crystal in the cryo-loop was cooled immediately with liquid nitrogen and mounted on the 90-degree Goniometer Head Arc (Hampton Research) with nitrogen gas stream at 100 K. Diffraction data were collected at $\lambda = 0.709$ Å at 100 K by synchrotron radiation at the beamline BL41XU of SPring-8 equipped with a MarCCD detector. The distance between the

crystal and CCD was 222 mm. The crystal was oscillated 2.5 degrees per frame, and the total measurement angle was 150 degrees. The dataset was processed, merged, and scaled with MOSFLM (56) and SCALA in the CCP4 package (57,58). The crystallographic data and diffraction statistics are given in Table 1. DETWIN, in the CCP4 package (57,59), and CNS (60) were used to detect crystal twinning and to determine the twinning fraction.

Model building and Refinement. The apoHO structure was determined by the molecular replacement method with CNS (60). The cross-rotation and translation functions were calculated from the protein moiety of the rat ferric heme-HO structure (PDB code, 1DVE). The cross-rotation function gave the orientations of the three apoHO molecules present in an asymmetric unit. The subsequent translation function search gave the position of one of the three apoHO molecules in an asymmetric unit. The position of the second molecule was determined by the translation function fixing the position of the first molecule. After the positions of the two molecules were determined, the same process was used to establish the position of the third molecule.

The apoHO crystals obtained in this study were not single but hemihedrally twinned crystals. Britton plot analysis (61) and an analysis of the cumulative distribution of H (59) were used to determine the twinning fraction. Detwinned data were used in all refinements, the twinning fraction being fixed at 0.45. Test reflections for calculation of the free *R* factor were selected as all the twin-related reflections belonged to the same sets (either the test or working sets) to avoid correlations introduced by twinning (59). Because the electron density corresponding to the A-helix in the ferric heme-HO structure was not clearly visible after simulated annealing refinement, the A-helices of the three molecules in the asymmetric unit were deleted from the model. Non-crystallography symmetry restraints were applied to the initial refinement then in subsequent refinements gradually relaxed. Non-crystallography symmetry restraints were not applied to the final refinement. A few cycles of water picking

and energy minimization refinements were performed. Temperature factors of all atoms were refined individually. All refinements were done using the reflections in the resolution range of 50.0-2.55 Å with CNS (60) and using the twinning option. Program O (62) was used to adjust and model the protein atoms and water molecules. Stereochemical checks of all the models were made with PROCHECK (63). Refinement statistics are given in Table 1.

Table 1 Summary of crystallographic statistics of apoHO

Crystallographic data	
Space group	$P3_2$
Unit cell dimensions (Å)	$a = b$ =70.2, c = 141.5
No. of molecules in asymmetric unit	3
Twinning operator/fraction	*k,h,-l* / 0.45
Diffraction statistics	
Resolution (Å)	30.0 - 2.55
No. of observations	93875
No. of unique reflections	25283
Completeness (%)	99.9 (99.9)*
Mean I/σ	9.9(2.9)*
†R_{sym}	0.059 (0.250)*
Refinement statistics	
††Twinned R/R_{free}	0.202/0.307
†††Detwinned R/R_{free}	0.324/0.394
No. of water molecules	85
Average temperature factors	
molecule A (Å^2)	35.1
molecule B (Å^2)	44.6
molecule C (Å^2)	38.7
Rms deviations from ideality	
bond lengths (Å)	0.009
angles (deg)	1.48

†$R_{sym} = \Sigma_{hkl} \Sigma_i |I_i(hkl) - \langle I(hkl)\rangle| / \Sigma_{hkl} \Sigma_i I_i(hkl)$, $\langle I(hkl)\rangle$ is the mean intensity for multiple recorded reflections.

††Twinned $R = \Sigma|F_{obs}(hkl) - [F_{calc}(hkl)^2+F_{calc}(kh\text{-}l)^2]^{1/2}|| / \Sigma |F_{obs}(hkl)|$.

†††Detwinned $R = \Sigma |F_{detwin}(hkl) - F_{calc}(hkl)|| / \Sigma |F_{detwin}(hkl)|$.

Each R_{free} is the R calculated for five percent of the dataset, not including refinements.

* Values in parentheses are for the outermost shell (2.69-2.55 Å).

RESULTS

Determination of the space group and detection of twinning. Because the apparent diffraction pattern of the apoHO crystal had $P\bar{3}m1$ Patterson symmetry (R_{sym} = 0.058) and (00*l*) diffractions were absent when $l \neq 3n$, I firstly assigned the space group of the crystal as $P3_121$ or $P3_221$. When the space group of the crystal was assumed to $P3_221$, two of the apoHO molecules in the asymmetric unit, determined by the molecular replacement method, severely interfered with each other. When the space group was assumed to be $P3_2$, the three molecules in the asymmetric unit were favorably packed. In this case, the R and R_{free} factors in the refinements were not decreased (R/R_{free} = 0.35/0.4), even though the model was well-fitted to the $2F_o$-F_c map. The apparent space group of $P3_221$ suggested that the crystal of the $P3_2$ space group may be a perfect twin, with a twinning operator of *k,h,-l* (64). To determine the twinning fraction, Britton plot analysis (61) and a plot of the cumulative distribution of H (59) were applied to the diffraction intensity data. Figure 2-2 shows that this crystal is a twin with a twinning fraction of 0.45.

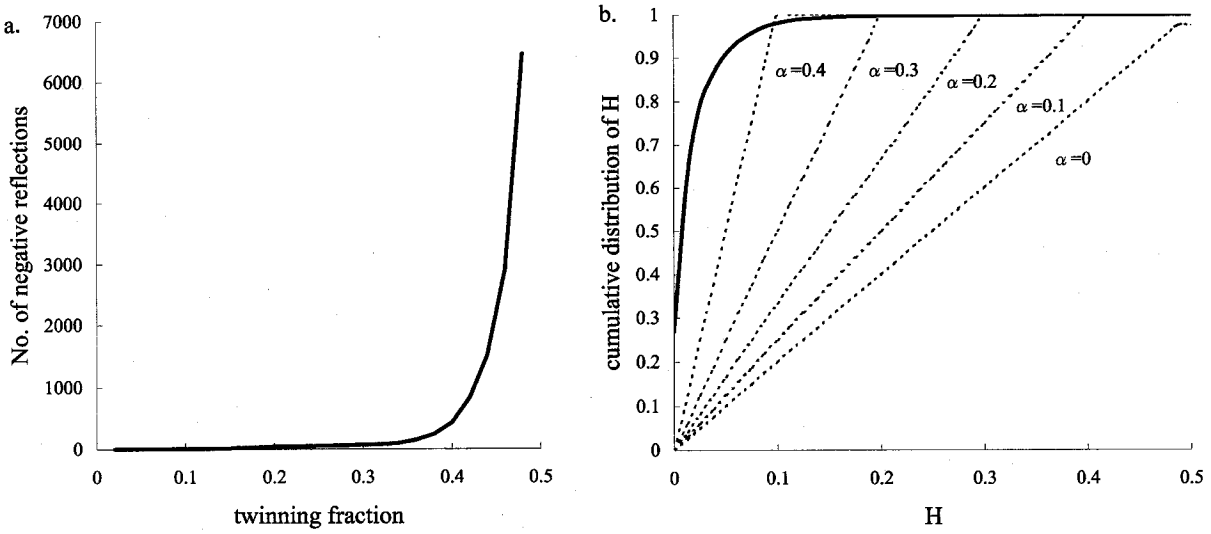

Figure 2-2. **Detection of hemihedral twinning and determination of the twinning fraction.** a. Britton plot analysis. The solid line represents the number of negative reflections of the data for apoHO in several estimated twinning fractions. When twinning fraction was over-estimated, the number of negative reflections were drastically increased. b. Analysis using the cumulative distribution of H. Dotted curves show the expected cumulative distribution of H for several twinning fractions. The solid line represents the data for apoHO. The twinning operator is *k,h,-l* in both plots.

Because it was a mimetic perfect twinning crystal, I averaged the twin-related reflection intensities to simulate perfect twinning and used this averaged data for refinement on the assumption that the crystal had a perfect twinning (65). It should be noted that such refinement procedures were heavily biased toward a Fourier synthesis map from the model. I therefore refined the model with a twinning fraction of 0.45.

Overall structure. The apoHO structure has been refined to a twinned *R* factor of 0.202 and a twinned free *R* factor of 0.307 at 2.55 Å resolution. For statistical reasons, the difference between the *R* and R_{free} factors in the presence of a twin can be higher than in the usual case (65,66). There were three molecules (A, B, and C) in the asymmetric unit. The final model had 4752 protein atoms and 85 water molecules. Approximately 30 N-terminal residues of the 267-residue protein, corresponding to the A-helix in ferric heme-HO, were deleted from the model because they were not ordered. The last 40 and several residues were also disordered, as seen in ferric heme-HO. The electron density of molecule B is discontinuous between residues 143 and 144. For molecule A residues 31-222, for B residues 30-142 and 145-223, and for C residues 30-225 could be built.

Superposition of the structures of molecules A-C is shown in Figure 2-3. The three molecules have similar folds that mainly consist of α-helices, as evidenced by the low value (0.67 Å) of the overall rms deviation for Cα atoms. The plot of the rms deviations of the apo-forms (Figure 2-3c, *solid line*) shows that residues with a large deviation (> 1.5 Å) are localized in the B-helix and B-C loop, and in the middle of the F-helix. A comparison of the overall structure of molecule A of apoHO with that of ferric heme-HO (Figure 2-3b) shows that the helices that form the heme pocket of ferric heme-HO (i.e., the A-, B-, and F-helices) fluctuate or are distorted in the apo-state, whereas the remainder of the apoprotein, including the C-, D-, E-, G-, and H-helices, has essentially the same folding as that of ferric heme-HO. When the rms deviations of the Cα atoms were calculated by combining the datasets for ferric

heme-HO and apoHOs (Figure 2-3c, *dashed line*), residues in the B-helix, B-C loop, and in the middle of the F helix had larger values than those calculated for apoHOs. In addition, deviation increased for the residues in F-2 (in this section, L120-D140 and G143-M155 are named F-1 and F-2 segments, respectively). The greatest part of the variance between the apo and holoproteins therefore is localized around the hemepocket.

Distal helix. An electron density map of molecule C around the hemepocket is shown in Figure 2-4a. In ferric heme-HO, the F-helix covers the distal surface of the heme, with closest access of Gly-139 and Gly-143 to a water or hydroxyl ligand (36). In contrast, the F-helix in apoHO, especially at the F-2 segment, shifts away from the heme pocket, although it remains bent (Figure 2-4b). The main-chain conformation of a few residues around Gly-143 changes from an α-helix to a random coil. The amide group of Gly-143 in molecule A is directed away from the heme pocket, whereas the carbonyl group of Gly-139 still points in the same direction as that in ferric heme-HO. The F-helix in molecule B fluctuates markedly, Gly-143 and Gly-144 being disordered. In molecule C, the F-helix adopts a conformation similar to that in molecule A, but the position of Gly-139 is altered in order for its carbonyl group to turn aside from the heme pocket.

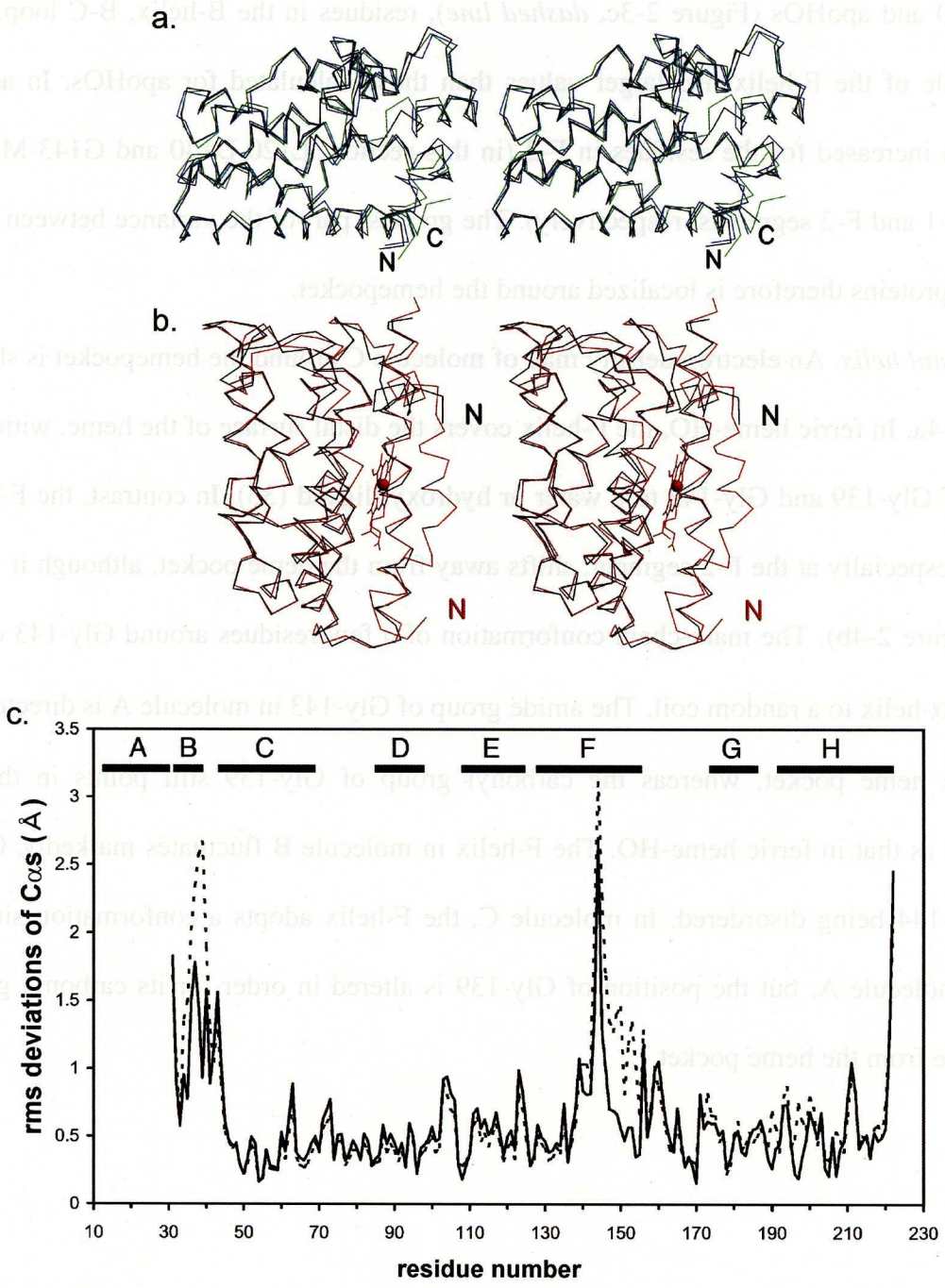

Figure 2-3. **Comparisons of three molecules of rat apoHO and heme-HO.** a. Stereo view of the Cα traces of molecules A (black), B (blue), and C (green) of rat apoHO in the asymmetric unit. Superposition was done to minimize the square deviations of the Cα atoms among all the amino acids. The N- and C-termini of the ordered segments respectively are shown as N and C. b. Stereo view of the Cα traces of molecule A of rat apoHO (black) and rat heme-HO (red). Superposition was done to minimize the square deviations of the Cα atoms among all the amino acids except the B- and F-helices. N-termini of the ordered segments of both molecules are shown in their respective colors as the letter N. c. Plot of the rms deviations of Cα atoms among apoHOs (*solid line*) and between apoHOs and heme-HO (*dashed line*). Solid horizontal bars indicate the helices in heme-HO. These figures were prepared with MOLSCRIPT (125) and RASTER3D (126).

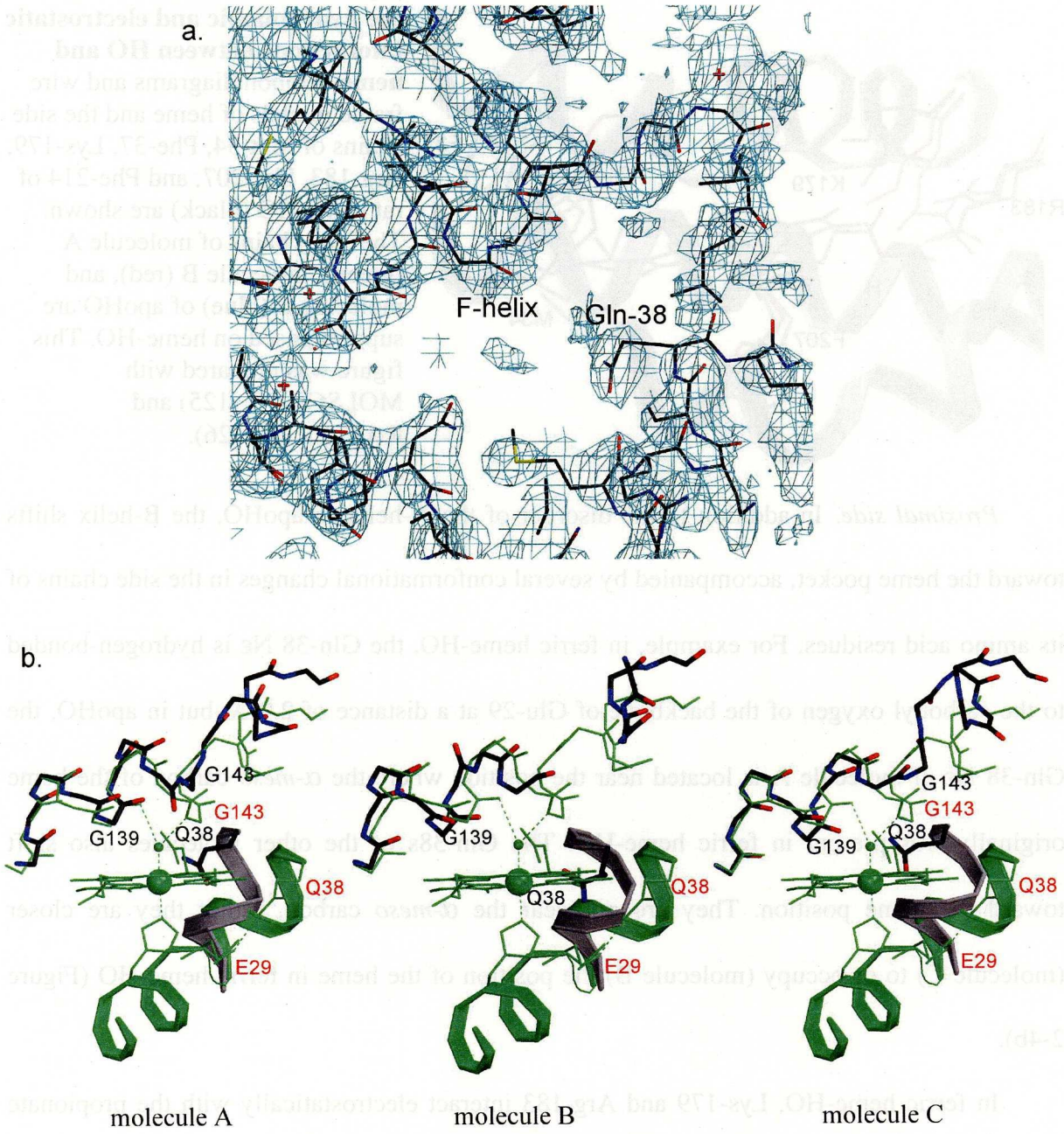

Figure 2-4. **Structural comparisons between apoHO and the HO-heme complex.** a. σ_A weighted $2F_o$-F_c map contoured at 1.3σ (cyan) superimposed on the wire-frame model of molecule C of apoHO around the hemepocket. b. Superpositions of the models near the heme pocket of molecule A of apoHO (carbon; black, oxygen; red, nitrogen; blue) and rat HO-heme (green). Both molecules are shown as wire-frame models. Dashed lines indicate hydrogen bonds or coordinate bonds. These figures were prepared with MOLSCRIPT (125), CONSCRIPT (127), and RASTER3D (126).

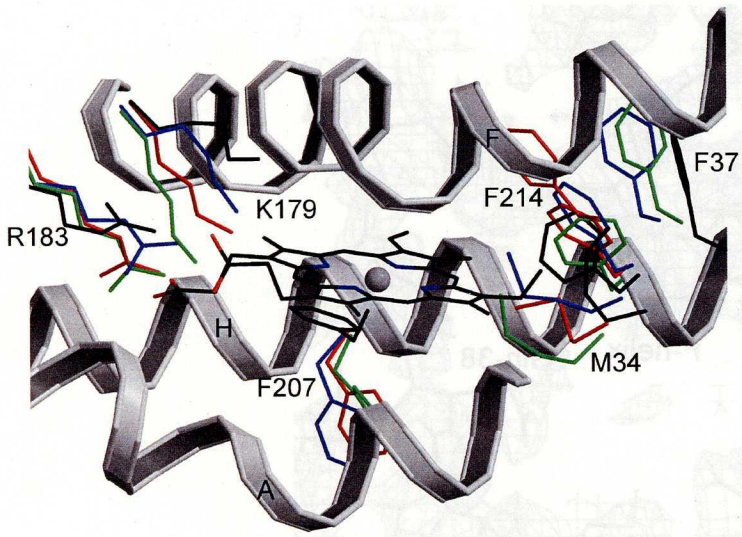

Figure 2-5. **Structural changes in the hydrophobic and electrostatic interactions between HO and heme.** Ribbon diagrams and wire frame models of heme and the side chains of Met-34, Phe-37, Lys-179, Arg-183, Phe-207, and Phe-214 of rat heme-HO (black) are shown. The side chains of molecule A (green), molecule B (red), and molecule C (blue) of apoHO are superimposed on heme-HO. This figure was prepared with MOLSCRIPT (125) and RASTER3D (126).

Proximal side. In addition to the disorder of the A-helix in apoHO, the B-helix shifts toward the heme pocket, accompanied by several conformational changes in the side chains of its amino acid residues. For example, in ferric heme-HO, the Gln-38 Nε is hydrogen-bonded to the carbonyl oxygen of the backbone of Glu-29 at a distance of 2.9 Å, but in apoHO, the Gln-38 Nε of molecule A is located near the position where the α-*meso* carbon of the heme originally was present in ferric heme-HO. The Gln-38s of the other molecules also shift toward the heme position. They are not near the α-*meso* carbon, rather they are closer (molecule C) to or occupy (molecule B) the position of the heme in ferric heme-HO (Figure 2-4b).

In ferric heme-HO, Lys-179 and Arg-183 interact electrostatically with the propionate group of the heme (36,40). The Arg-183 of the three apoHO molecules and the Lys-179 of molecule C of apoHO have approximately the same conformations as those in ferric heme-HO (Figure 2-5), but the side chains of Lys-179 in molecules A and B are flipped at the Cα atom. As a result, Lys-179 Nε more closely approaches the position at which the propionate group of the heme originally was present in ferric heme-HO (Figure 2-5). In ferric heme-HO, Met-34, Phe-37, and Phe-214 form a hydrophobic wall opposite the α-*meso* heme edge (36,40). These apoHO residues roughly retain their conformations, but Met-34 and

Phe-37 approach the inside of the heme pocket due to the B-helix shift. In particular, the Phe-37 in molecule B is much closer to the position of the heme in ferric heme-HO than is the Phe-37 of the other apoHO molecules (Figure 2-5). The side chain of Phe-207, present under the α-*meso* edge of the heme (36,40), is flipped at the Cα atom and points down the position of the A-helix in ferric heme-HO (Figure 2-5). As a result, the fluctuations and distortions in apoHO lead to the exposure of the heme binding pocket to solvent. The hemepocket of apoHO therefore should be more easily accessible for heme binding.

Core structure. The Cα atoms of residues 44-138 and 155-220 in apoHO can be superimposed on the Cα atoms of the corresponding residues in ferric heme-HO with a low rms deviation of 0.55 Å, indicating there is little change in the core structure of HO whether or not heme is present. An extended hydrophobic cluster is formed along the interfaces of the C-, E-, F-1-, and H-helices (Figure 2-6a). Aliphatic and aromatic residues of the two loops between the C- and D-helices and between the F-and G-helices also participate in this hydrophobic interaction. The D- and G-helices exist outside of the core, but both establish van der Waals contacts with the C-helix and the first half of the F-helix, respectively, by forming hydrophobic interfaces. In addition to these hydrophobic interactions, both the helix-helix and helix-loop interfaces are stabilized by a number of hydrogen-bonded or electrostatic pairs: Tyr-58 and Asp-140, Glu-62 and Arg-86, Glu-66 and Tyr-78, Trp-96 and Gly-163, Arg-117 and Glu-202, Arg-198 and Glu-127, Asn-210 and Arg-136, Glu-216 and Thr-108, and Glu-216 and Ala-110 (Figure 2-6b).

Like ferric heme-HO, the surface of the heme-binding side of apoHO is charged positively and the opposite one negatively (Figure 2-7). This feature is important for interaction with CPR. The surface charge distribution of apoHO is essentially the same as that of ferric heme-HO. CPR therefore would contact HO even in the apo state, but it remains to be explained how this interaction is involved in heme oxygenase catalysis.

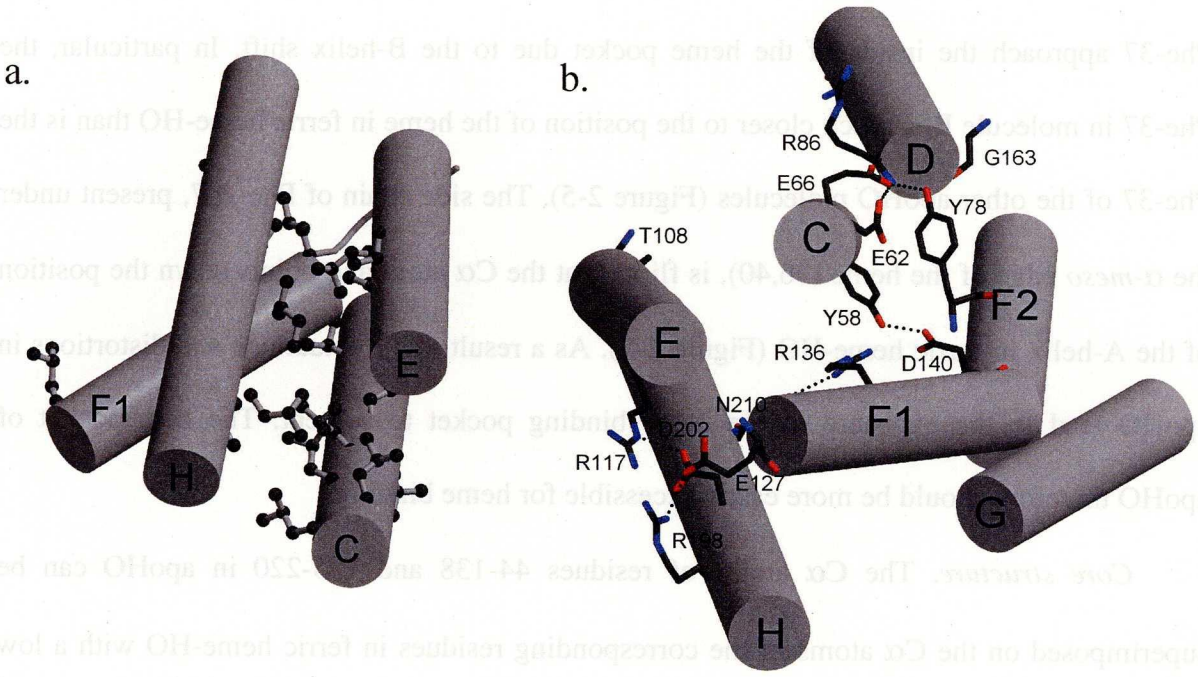

Figure 2-6. **Schematic representations of the core structure of apoHO.** a. The hydrophobic core of HO is shown. The C, E, F-1, and H helices are shown as cylinders. Hydrophobic residues (Leu, Ile, Val) in these helices are shown as ball-and-stick models. b. C-H helices in apoHO are shown as cylinders. Hydrogen bondings and electrostatic interactions conserved among the rat heme-HO and apoHOs are represented by dotted lines. Side chains involved in these interactions are shown as wire frame models. These figures were prepared with MOLSCRIPT (125) and RASTER3D (126).

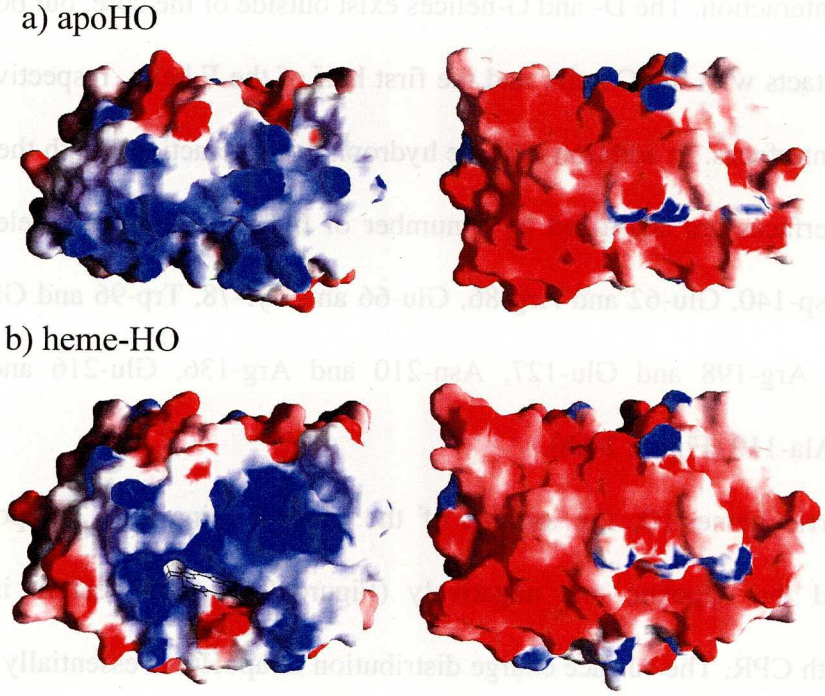

Figure 2-7. **Electrostatic potential of rat HO.** Molecular surfaces colored by electrostatic potential were shown (blue: positive, red: negative). Left and right show the heme binding surface and its opposite, respectively. Heme binding surface is positively charged in apoHO and heme-HO. These figures were prepared with GRASP (128).

DISCUSSION

The major differences in the crystal structures of ferric heme-HO and apoHO are limited to the helices directly involved in heme binding. The proximal helix, A, in apoHO is not visible in this analysis. The distal helix, F, partially fluctuates; its middle portion becomes a random coil and the latter half (Val-146~Ala-151) varies in conformation among the three apo forms. In contrast, both helices in ferric heme-HO are stabilized by a number of interactions with heme; i.e., coordination of the imidazole side chain of the proximal His-25 to the heme iron, an electrostatic interaction between the $N\zeta H_3^+$ group of Lys-18 and the propionate groups of the heme, and the hydrogen bonds between the backbones of the distal glycines and the distal water ligand of the heme. Other electrostatic interactions occur between the basic side chains of Lys-179 and Arg-183 and the propionate groups of heme. These electrostatic interactions present in rat HO-1 are also conserved in human HO-1 (40). Interestingly, the mutation of Arg-183 to Glu or Asp was found to cause changes in the α-regioselectivity of the heme oxygenase reaction (45). It is noteworthy that the basic side chains of Lys-179 and Arg-183 in apoHO maintain an orientation similar to those in the holo-state. Furthermore, in the holoprotein, a hydrogen bond between the backbone of Glu-29 in the A-helix and the side chain of Gln-38 in the B-helix appears to contribute to the formation of the heme pocket. A previous study showed that replacement of the proximal His-25 with Ala led to the loss of HO activity, but this substitution did not significantly affect the molecule's heme-binding capability, indicative that these stated additional interactions, rather than the coordination of His-25 to heme, are crucial in the initial stage of heme binding (43).

When all these findings are considered, they suggest a possible induced-fit model for the binding of heme to HO (Figure 2-8). Before heme binding, the A-helix assumes a random conformation such that the heme pocket is exposed to the solvent. The side chain of Gln-38

partially occupies the binding site. Once heme binds to the heme pocket, Gln-38 and the B-helix shift away from the pocket to avoid steric hindrance between the heme and Gln-38. The electrostatic interaction between the propionate groups of heme and the side chains of Lys-179 and Arg-183 would facilitate the correct orientation of the heme. Gln-38 Nε then forms a hydrogen bond to Glu-29 O of the A-helix, and the angle between the A- and B-helices is fixed. Finally, Lys-18 and the propionate groups of the heme form a salt bridge, and His-25 Nε ligates to the heme iron. The structural features of the heme pocket are well conserved in rat and human HO-1s, suggesting that mammalian enzymes use a similar mechanism to incorporate the heme substrate.

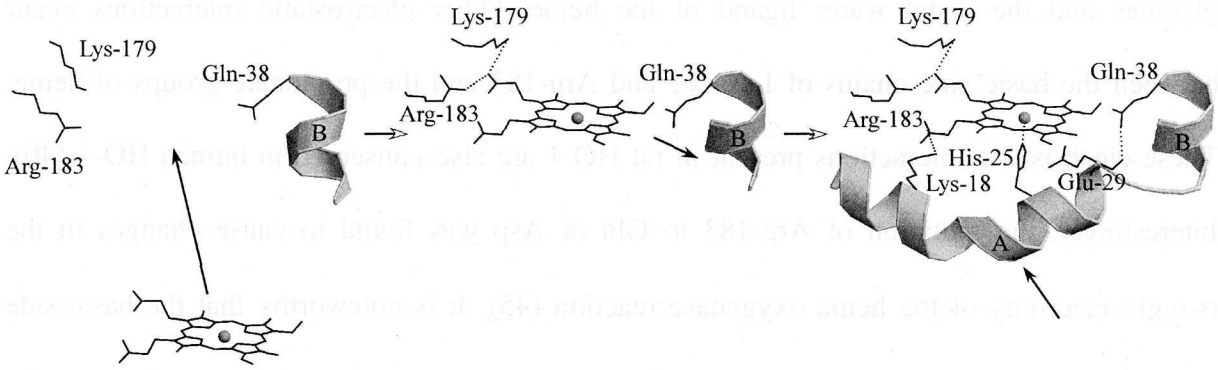

Figure 2-8. **The proposed mechanism of heme binding to apoHO.**

Recentrly, the crystal structure of the *Neisseria meningitides* HO in complex with them was determined (41). Gln-38 is conserved among mammalian HO-1s, but is substituted for Val in *N. meningitidis* HO. This substitution suggests that the binding mechanism of the heme of *N. meningitidis* HO may differ somewhat from that in our proposed model (Figure 2-8). In *N. meningitidis* heme-HO, there is a C-terminal loop at the position where the B-helix is in ferric heme HO. The A-helix should be stabilized by the interaction between the A-helix and the C-terminal loop via hydrogen bonding (Asp-28 Nδ - Met-208 O) in *N. meningitidis* heme-HO. In mammalian HO-1s, the segment which corresponds to the C-terminal loop in the *N. meningitidis* heme-HO is disordered, but its structure probably differs from that of the

N. meningitidis heme-HO because there is no sequence similarity between the mammalian HO-1 and *N. meningitidis* HO in this region (Figure 1-7). Mammalian HO-1s are membrane-bound proteins that span the membrane of the endoplasmic reticulum at the C-terminus, and *N. meningitidis* HO is a soluble protein (67). This difference is thought to be responsible for the structural difference at the C-termini.

The kinking and flexibility of the distal helix are believed to be crucial factors for heme oxygenase catalysis. An asymmetric unit of human ferric heme-HO crystals has "closed" and "open" forms, which differ in the distance between the distal helix and heme plane (40). The opening of the active site has been inferred to allow substrate binding and product release, while the closing of this site would enforce regioselectivity and facilitate the reaction. In apoHO, the three molecules in the asymmetric unit have different conformations in the segment that corresponds to the F-2 segment in ferric heme-HO. Moreover, a few residues around Gly-143 have changed their secondary structures to a random coil, indicative that this segment forms an unstable conformation in apoHO. The flexibility of this segment differs from that at the kinked site (Leu-141~Ser-142), causing an overall shift of the F-2 segment as seen in the structures of heme-HOs (36,40,41). The primary factor that determines the flexibility in apoHO probably is the absence of heme because this segment has direct contact with the heme plane, and the distal ligand of the heme iron is hydrogen-bonded to the Gly-143 in rat heme-HO (36). Unlike the proximal and distal helices, the remainder of HO retains its structure, irrespective of whether or not heme is bound. Five helices (C, D, E, G, and H) and part of the F-helix assemble to form the extended hydrophobic core. This core structure most likely provides stability for the overall structure of the enzyme thereby minimizing conformational change both on the binding of the substrate and release of the product.

It should be noted that, consistent with the structure of apoHO, the known structures of

the apoproteins cyt b_5 (68,69) and cyt b_{562} (70) have a similar feature in common; one of the axial helices fluctuates greatly, whereas the other remains folded. Studies of several of apoMb properties have indicated that apoMb is in the molten-globule state (71) and that one side of its heme pocket (F-helix) is disordered (72). Although HO, Mb, cyt b_5, and cyt b_{562} show a similar structural changes around the heme pocket upon heme binding, there is no similarity in their overall structures; HO (36,40,41), Mb (73), cyt b_{562} (74) are all α proteins with different folding motifs and cyt b_5 (75) consists mainly of anti-parallel β sheets and α helices. This finding suggests that there is a common feature between the pathways to maturation of the three b-type hemoproteins and the heme binding in heme-HO is inserted into the opened heme pocket of the apoprotein, fixes the orientation of the disordered helix, and stabilizes the conformation of the heme pocket.

Poulos *et al.* have recently determined human apoHO-1 structure (76). F-helix conformation and the disruption of hydrogen bond between Gln-38 and Glu-29 are similar to our result, but A-helix in their structure is ordered. This difference may be caused by the difference of crystal packing; A-helix in their crystal was interacted with other apoHO molecules, but estimated A-helix regions in our crystal were free from the interaction of other apoHO molecules.

1.2 Hydroxylation mechanism of heme based on the structure of ferric heme-HO bound to azide

ABSTRACT

Heme oxygenase (HO) catalyzes physiological heme degradation consisting of three sequential oxidation steps that use molecular oxygen and reducing equivalents. I determined the crystal structure of rat ferric heme-HO-1 complex bound to azide at 1.9 Å resolution. The azide bound to heme iron are directed toward the α-*meso* position of the heme. Azide shows bent-binding mode as well as the binding mode of molecular oxygen based on RR spectroscopic analysis using isotope shift. The azide is surrounded by residues of the distal F-helix, only the direction to the α-*meso* carbon being open. This indicates that regiospecific oxidation of the heme is primarily caused by steric constraint between the molecular oxygen bound to heme and the F-helix. The azide interacts with Asp-140, Arg-136, and Thr-135 through a hydrogen bond network involving five water molecules on the distal side of the heme. This network, also present in ferric heme-HO, may function in molecular oxygen activation in the first hydroxylation step. From the orientation of azide in its bound form, hydrogen peroxide, the active oxygen species of the first reaction, bound to ferric heme-HO is inferred to have a similar orientation suitable for direct attack on the α-*meso* carbon

MATERIALS AND METHODS

Crystallization of N_3^--heme-HO. Ferric heme-HO was prepared as described in the general introduction (Figure 1-5, (37-39)). N_3^--heme-HO was prepared by adding sodium azide to ferric heme-HO at the final concentration of 5 mM. The crystallization condition of N_3^--heme-HO was screened with Crystal Screen (Hampton Research) by the hanging-drop vapor-diffusion method. The protein solution was mixed with an equal volume of each reservoir solution and equilibrated. Crystals of N_3^--heme-HO were obtained at 293 K when the reservoir solution contained 4 M sodium formate. The protein concentration for crystallization was 18 mg ml^{-1} in 50 mM potassium phosphate buffer (pH 7.0) containing 5 mM sodium azide. Hexagonal rod-shaped crystals appeared after three days and grew to maximum size in a few weeks (Figure 3-1).

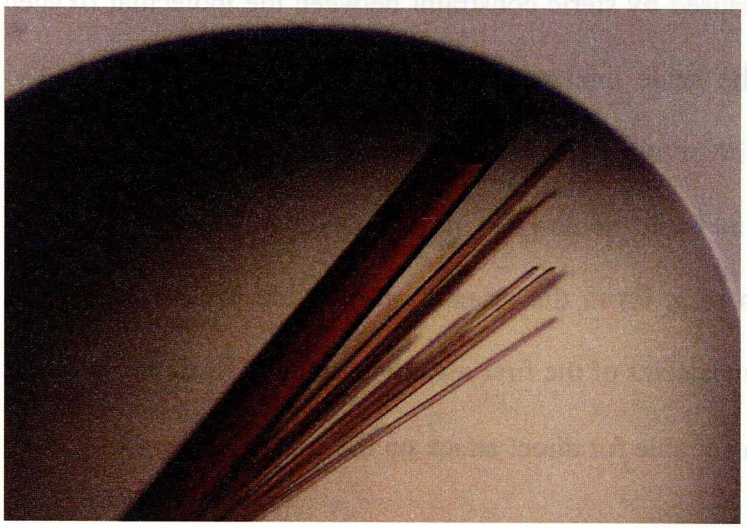

Figure 3-1. **Crystals of N_3^--heme-HO**

Data Collection and Processing. The N_3^--heme-HO crystal soaked for a few seconds in a crystallization solution containing 50 mM sodium azide immediately changed to bright red. The crystal was then handled with a cryo-loop and flash-cooled with a nitrogen gas stream at 100 K. Diffraction data were collected at 100 K using synchrotron radiation (λ = 1.000 Å) at the beamline BL40B2 of SPring-8 and an ADSC Quantum4R detector. Diffraction data were processed, merged, and scaled with HKL2000 (77). Crystallographic data and

diffraction statistics are given in Table 2.

Model building and Refinement. The structure of N_3^--heme-HO was determined by the molecular replacement method with CNS (60), in which the protein moiety of the rat heme-HO-1 complex (PDB code, 1DVE) was the search model. Cross-rotation function gave a unique solution. A subsequent translation search with the above solution located the N_3^--heme-HO molecule in an asymmetric unit. Rigid body, simulated annealing, and temperature-factor refinements were applied to the solution based on 20.0-2.5 Å resolution data. The structure was revised by alternately adjusting the model with XtalView (78) and simulated annealing and temperature-factor refinements for 20.0-2.2 Å resolution data. The heme was clearly seen in the electron density map and was included in the subsequent refinement. A few cycles of water picking and energy minimization refinements were done on the 20.0-1.9 Å resolution data. Two azide ions were located in the F_o-F_c map; one is bound to the ferric heme iron, the other to Arg-27 located on the molecular surface. Lastly, they were included in the energy minimization refinement, in which the geometry of the azide ions was restrained but neither the $Fe^{3+}\cdots$ N-N angle nor $Fe^{3+}\cdots$ N distance was restrained. All refinements were done with CNS (60). The stereochemical check of the model was made with PROCHECK (63). Refinement statistics are given in Table 2.

ESR measurement of N_3^--heme-HO. The concentration of the ferric heme-HO complex was 600 uM in 50 mM potassium phosphate buffer (pH 7.0) containing 6 mM sodium azide. X-band ESR spectra were recorded at 13 K using a JEOL ESR spectrometer (JES FE3X) equipped with a JEOL liquid helium cryostat (ES-LTR5X). The instrumental conditions were: modulation frequency, 100 kHz; modulation amplitude, 2 mT; microwave frequency, 8.93 GHz; and microwave power, 1 mW. The microwave frequency was calibrated with a microwave frequency counter (Advantest) and the magnetic field strength determined with a JEOL NMR counter (JEOL ES-OC1).

Table 2 Summary of crystallographic statistics of N_3^--heme-HO

Crystallographic data	
Crystal system	Trigonal
Space group	$P3_221$
Unit cell dimensions (Å)	$a = b = 65.0$, $c = 120.3$
No. of molecules in an asymmetric unit	1
Diffraction statistics	
Resolution (Å)	20-1.9
No. of observations	169,506
No. of unique reflections	23,376
Redundancy	7.25
Completeness (%)*	97.9 (96.1)
Mean I_o/σ	11.6
R_{sym}†,*	0.054 (0.325)
Refinement statistics	
R/R_{free}††	0.189/0.219
No. of protein/heme atoms	1718/43
No. of inhibitors/water molecules	2/186
Rms deviation from ideality	
bond lengths (Å)	0.005
Angles (deg)	1.09
Ramachandran plots	
Most favored (%)	93.7
Additionally allowed (%)	6.3

† $R_{sym} = \Sigma_{hkl} \Sigma_i |I_i(hkl) - \langle I(hkl)\rangle| / \Sigma_{hkl} \Sigma_i I_i(hkl)$, $\langle I(hkl)\rangle$ is the mean intensity for multiple recorded reflections.

†† $R = \Sigma||F_{obs}(hkl) - F_{calc}(hkl)||/\Sigma |F_{obs}(hkl)|$.

R_{free} is the R value calculated for five percent of the dataset not included refinements.

* Values in parentheses are for the outermost shell (1.93-1.90Å).

RESULTS

Overall structure. The structure of N_3^--heme-HO was refined by use of the 1.9 Å resolution data to an R/R_{free} of 0.189/0.219. Ser-10 and Glu-223 are additionally disordered as compared with ferric heme-HO. The structure of N_3^--heme-HO consists mainly of α-helices and is very similar to that of ferric heme-HO (Figure 3-2), overall rms deviation for Cα atoms being 0.32 Å. Deviation of the heme iron in N_3^--heme-HO and ferric heme-HO is 0.21 Å. Although parts of the F-G (Ala-156~Glu-162) and G-H (Glu-190~Val-195) loops differ in the conformations between N_3^--heme-HO and ferric heme-HO, the differences should be due to the crystal packing force because these loops are located on the molecular surface and are in contact with other molecules in the crystal. The A-, B-, and F-helices, which form the heme pocket of N_3^--heme-HO, have the same conformations as in ferric heme-HO, and this heme also does not change position on azide binding.

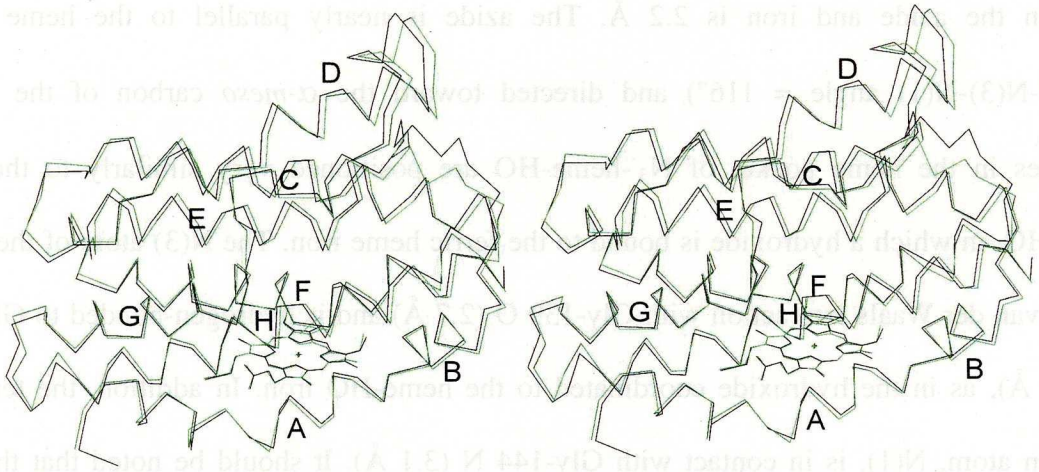

Figure 3-2. **Structural comparison of heme-HO and N_3^--heme-HO.** Stereo diagram of Cα traces; heme-HO (black), N_3^--heme-HO (green). Models are superimposed to minimize rms deviations of the Cαs of all the amino acid residues. Alphabets represent helices in heme-HO. These figures were prepared with MOLSCRIPT (125) and RASTER3D (126).

Heme orientation. The structure of N_3^--heme-HO was analyzed at a higher resolution than that of the structure of rat heme-HO (36), permitting a more detailed description of the manner of heme binding to HO-1. Close examination of the heme's electron density indicated that it binds to rat HO-1 in two different orientations, which are related by 180° rotation about

the α-γ axis of the heme, which agrees with an NMR report (79). In addition, residual electron density was present near one of the two propionate groups, exposed to the solvent, indicative of double conformers. Double conformers for one propionate group in heme have been reported in *N. meningitidis* heme-HO (41). The two orientations of the heme and two conformations of the propionate group would not affect the regiospecificity of HO catalysis because the α-*meso* carbons in both orientations are at the same position. The present refinement includes only the major orientation of the heme and conformation of the propionate group, because it is still difficult at the present resolution to determine the ratios of the two alternative orientations and conformers.

N_3^--heme-HO heme pocket. An electron density map around the heme pocket of N_3^--heme-HO is given in Figure 3-3a. The F_o-F_c map shows elongated density on the distal side of the heme, assignable to the azide coordinated to the ferric heme iron. The distance between the azide and iron is 2.2 Å. The azide is nearly parallel to the heme plane ($\angle Fe^{3+}$-N(3)-N(1) angle = 116°) and directed toward the α-*meso* carbon of the heme. Residues in the heme pocket of N_3^--heme-HO are positioned very similarly to those of heme-HO, in which a hydroxide is bound to the ferric heme iron. The N(3) atom of the azide is in a van der Waals interaction with Gly-139 O (2.7 Å) and is hydrogen-bonded to Gly-143 N (2.8 Å), as in the hydroxide coordinated to the heme-HO iron. In addition, the terminal nitrogen atom, N(1), is in contact with Gly-144 N (3.1 Å). It should be noted that the five water molecules involved in the hydrogen-bonding network at the distal pocket of N_3^--heme-HO are located in almost identical positions as those in heme-HO, rms deviation being less than 0.6 Å. Azide interacts with the carboxyl group of Asp-140 via W1 and W2 and with the carbonyl groups of Thr-135 and Arg-136 via W1 and W3 (Figure 3-3b).

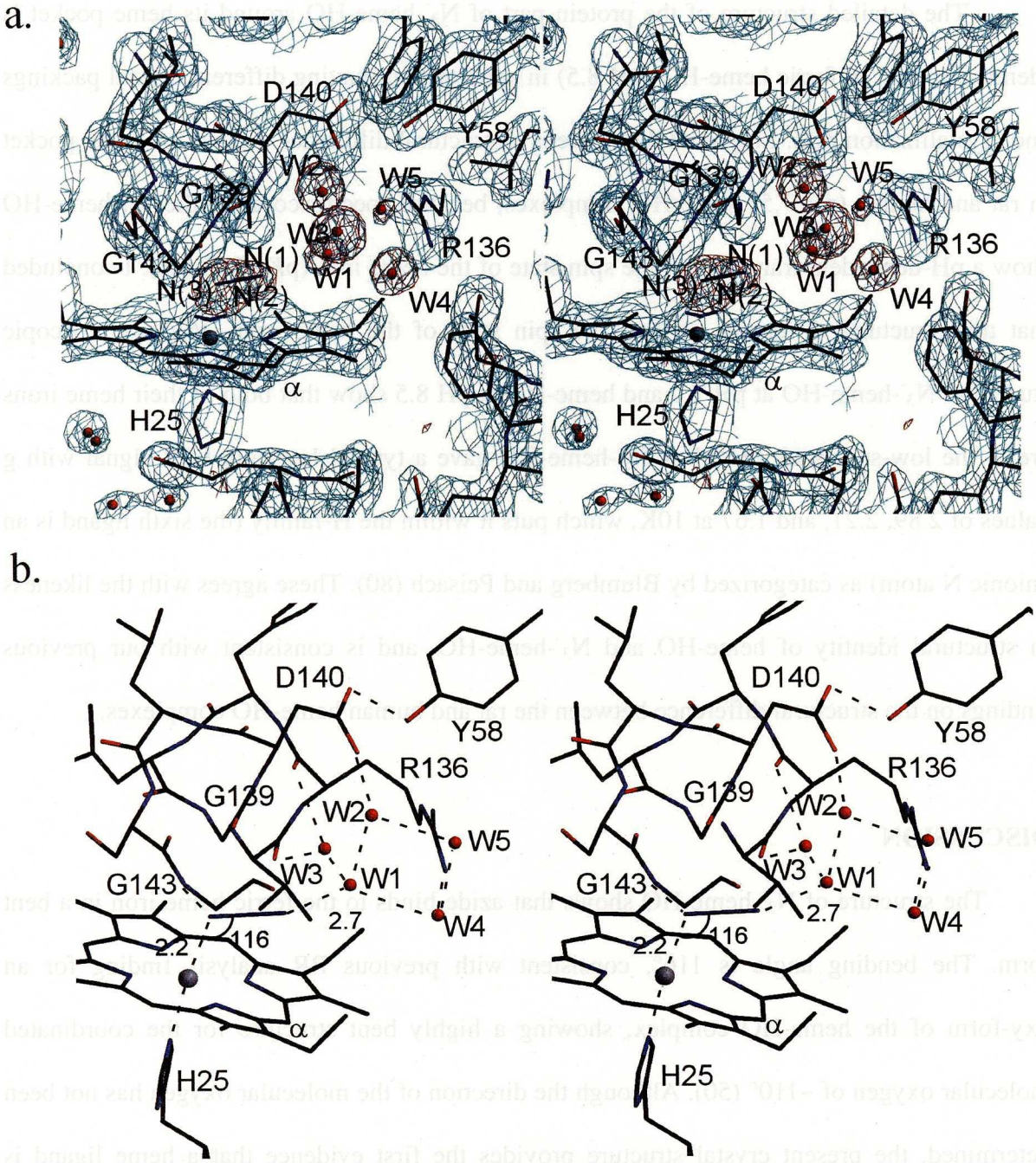

Figure 3-3. **Structure of N_3^--heme-HO around the heme pocket.** a. Stereo diagram showing σ_A weighted $2F_o$-F_c map contoured at 1.5σ (cyan) superimposed on the heme pocket of the wire-frame model of N_3^--heme-HO. Red shows a σ_A weighted F_o-F_c map contoured at 3.5σ, calculated by omitting the azide and five water molecules. b. Stereo diagram showing the hydrogen bond network on the heme's distal side in N_3^--heme-HO. Dashed lines indicate both hydrogen and coordinate bonds. Distances shown are in angstrom units. The Fe^{3+}·· N-N angle is in degrees. Water molecules involved in the hydrogen bond network are labeled W1-W5. Distances are azide N(1)·· W1; 2.7 Å, W1·· W2; 2.6 Å, W2··Asp-140 O; 3.0 Å, Asp-140 Oδ·· Tyr-58 Oη; 3.0 Å, Asp-140 Oδ·· Arg-136 Nη; 3.0 Å, W3·· Thr-135 O; 3.0 Å, W3·· Arg-136 O; 2.8 Å, W1·· W3; 2.8 Å, W1·· W4; 2.8 Å, and W2·· W5; 2.7 Å. These figures were prepared with MOLSCRIPT (125), CONSCRIPT (127), and RASTER3D (126).

The detailed structure of the protein part of N_3^--heme-HO around its heme pocket is identical to that of ferric heme-HO (pH 8.5) in spite of their having different crystal packings and crystallization pHs. I reported that there is a structural difference around the heme pocket in rat and human (pH 7.5) heme-HO complexes, because spectroscopic studies of heme-HO show a pH-dependent transition of the spin state of the heme iron (p*Ka* 7.6) (28). I concluded that this structural difference reflects the spin state of the heme iron (36). Spectroscopic studies of N_3^--heme-HO at pH 7.0 and heme-HO at pH 8.5 show that both of their heme irons are in the low-spin state (51). Rat N_3^--heme-HO gave a typical low-spin ESR signal with g values of 2.89, 2.21, and 1.67 at 10K, which puts it within the H-family (the sixth ligand is an anionic N atom) as categorized by Blumberg and Peisach (80). These agrees with the likeness in structural identity of heme-HO and N_3^--heme-HO, and is consistent with our previous findings on the structural difference between the rat and human heme-HO complexes.

DISCUSSION

The structure of N_3^--heme-HO shows that azide binds to the ferric heme iron in a bent form. The bending angle is 116°, consistent with previous RR analysis finding for an oxy-form of the heme-HO complex, showing a highly bent structure for the coordinated molecular oxygen of ~110° (50). Although the direction of the molecular oxygen has not been determined, the present crystal structure provides the first evidence that a heme ligand is actually directed toward the α-*meso* carbon of the heme bound to HO. Both the highly bent coordination and the α-*meso* orientation of the heme ligand are required for the first hydroxylation step of the HO reaction, because chemical studies of heme analogs in a complex with HO suggest that the active oxygen species, hydroperoxide, directly attacks the α-*meso* carbon of heme in the first step (Figure 1-3b, (17,18)). The N_3^- bound structure therefore should provide a suitable model for studying the regiospecifity of the HO reaction.

Several interactions between the azide and heme-HO are involved in determining the direction of both ligands about the Fe-ligand axis. The major interactions are van der Waals interactions with Gly-139 and Ser-142 and hydrogen bond interaction with Gly-143 N. CPK modeling of the residues surrounding the azide and heme (Figure 3-4) does in fact show that the azide is forced to direct its terminal nitrogen, N(1), toward the α-*meso* carbon.

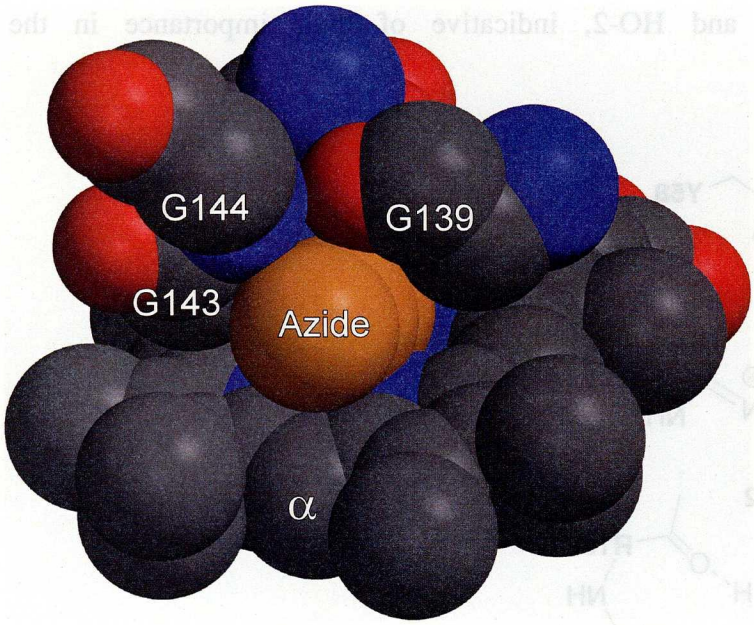

Figure 3-4. **Interaction between HO and azide.** CPK model showing Gly-139, Ser-142, Gly-143, Gly-144, heme, and the azide. Carbons, nitrogens, and oxygens of heme and protein, respectively, are shown in gray, blue, and red. Azide atoms are shown in orange. The figure was prepared with MOLSCRIPT (125) and RASTER3D (126).

Another important finding is that the hydrogen-bonding network at the distal pocket in heme-HO is highly conserved even in the azide-binding states. Similar hydrophilic interactions occur at the distal pockets in heme complexes with human HO-1 (40) and *N. meningitidis* HO (41), in which water or a hydroxy ligand exists. The hydrogen-bonding network reported here should help stabilize accommodation of the distal ligand, a hydrogen bond acceptor, located 2.7 Å from W1 (Figure 3-3). The explanation of hydrogen-bonding interactions is shown schematically in Figure 3-5. The carboxylate group of Asp-140, forms a salt bridge to the side chain of Arg-136 and interacts with the hydroxy group of Tyr-58, making W1 anionic through a hydrogen-bonding relay intermediated by W2. In addition, the hydrogen-donating ability of W1 is enhanced by the carbonyl groups of Thr-135 and Arg-136 via W3. W1 therefore is a potent hydrogen donor to the coordinated azide, and the terminal

nitrogen atom, N(1), becomes positively charged. Moreover, the positive charge on N(1) is increased by the negative charge of the iron-bound nitrogen atom, N(3), which is hydrogen-bonded to the amide group of Gly-143. Taking this molecular polarization into account, an asymmetric resonance structure is dominant for the azide bound to heme-HO, as previously proposed for the Mb bound to azide (52). Tyr-58, Arg-136, and Asp-140 are all conserved in mammalian HO-1 and HO-2, indicative of their importance in the hydrogen-bonding network.

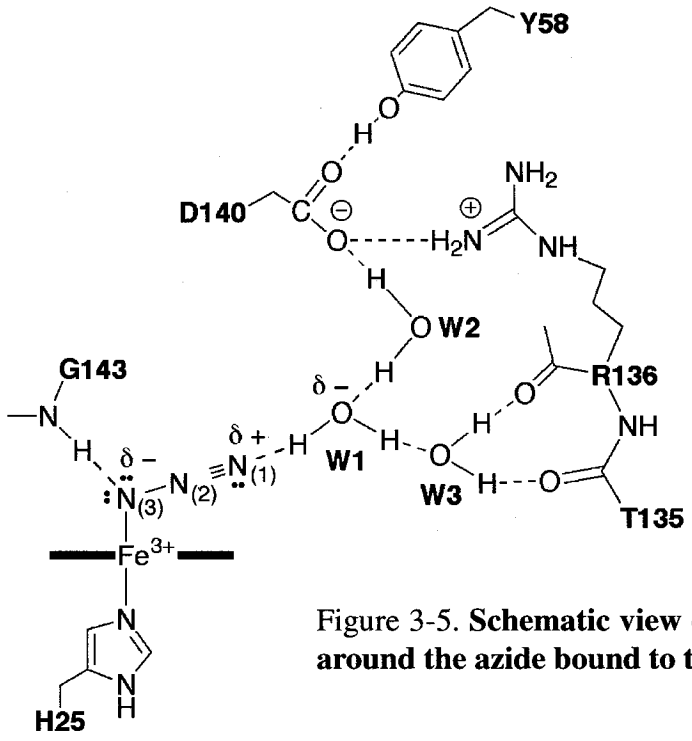

Figure 3-5. **Schematic view of hydrogen-bonding interactions around the azide bound to the ferric heme iron.**

Conceivably, the hydrogen-bonding network facilitates formation of ferric hydrogen peroxide by providing a proton to the peroxide produced by reduction of the molecular oxygen bound to the ferrous heme iron in the first HO reaction step. Like the azide, hydrogen peroxide is probably directed toward the α-*meso* carbon in a way that minimizes van der Waals repulsion with the distal residues. Although peroxide is shorter than azide, hydrogen-bonding between the peroxide and W1 should occur by minimal rearrangement of the bridging water molecules. Indeed, the distance between W1 and the hydroxy ligand in

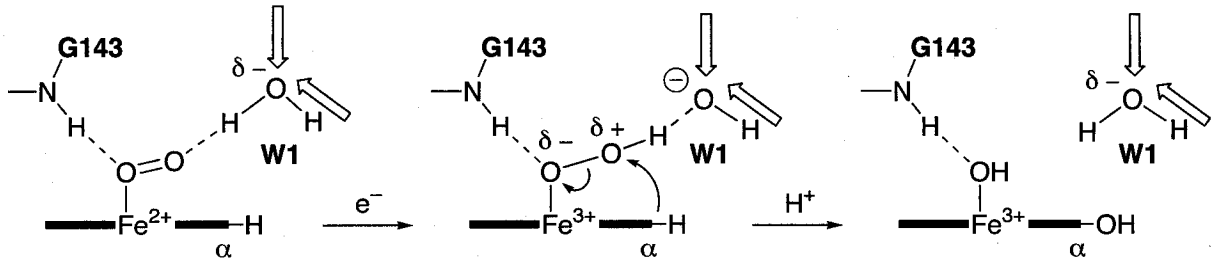

Figure 3-6. **A possible mechanism of protonation and activation of the peroxide bound to heme.** *Open arrows* represent the hydrogen-bonding network that enhances the hydrogen-donating ability of W1.

heme-HO is 4.0 Å (36) and the O-O distance of hydrogen peroxide is estimated as 1.46 Å. Accordingly, the distal oxygen of hydrogen peroxide acquires a positive charge through the hydrogen-bonding network, as well as through the amide group of Gly-143, resulting in stabilization of the negatively charged proximal oxygen. Increased electrophilicity of the distal oxygen should be favorable for oxidation of the α-*meso* carbon of the heme. Recent findings of site-directed mutagenesis analysis of the polar residues around the distal pocket of heme-HO show that the D140A mutant completely lost heme degradation activity (81,82) and that in the R136A mutant heme degradation was much slower than in the wild type HO (82). An ESR and ENDOR study by Davydov *et al.* showed that one-electron radiolytic cryoreduction of the oxy-ferrous form of the heme-HO complex at 77 K yields a hydroperoxoferri-HO species, evidence of prompt proton transfer from the distal hydrogen-bonding network to reduced molecular oxygen (83). More recently, they reported that the annealing of this species to 200 K resulted in formation of an active hydroperoxo intermediate with a second well-defined ^{1}H ENDOR signal (84). This intermediate directly formed an α-hydroxyheme product. They speculated that the second proton might have been part of a hydrogen bond that functions in the activation of the O-O bond for cleavage. It is noteworthy that the second proton detected in the ENDOR spectroscopy may be the amide proton of Gly-143, and it is expected to interact with the proximal oxygen of the hydrogen peroxide based on the hydroxide-bound heme-HO (36) and current N_3^--heme-HO structures.

Based on these findings, a possible mechanism of protonation and activation of the peroxide bound to heme is proposed (Figure 3-6).

1.3 Products release mechanism based on the structure of HO in complex with biliverdin IXα-iron chelate

ABSTRACT

The crystal structure of rat HO-1 in complex with biliverdin-iron chelate (biliverdin(Fe)-HO-1), the immediate precursor of the final product, biliverdin, has been determined at 2.4 Å resolution. The electron density in the heme pocket clearly showed that the tetrapyrrole ring of heme is cleaved at the α-*meso* edge. Like the heme bound to HO, biliverdin-iron chelate is located between the distal and proximal helices, but its accommodation state appears to be less stable in light of the disordering of the solvent-exposed propionate and vinyl groups. The middle of the distal helix is shifted away from the center of the active site in biliverdin(Fe)-HO-1, increasing the size of the heme pocket. The hydrogen-bonding interaction between Glu-29 and Gln-38, considered to restrain the orientation of the proximal helix in the heme-HO-1 complex, was lost in biliverdin(Fe)-HO-1, leading to relaxation of the helix. Biliverdin has a distorted helical conformation with the lactam oxygen atom of its pyrrole ring-A interacting with Asp-140 through a hydrogen-bonding solvent network. Owing to the absence of a distal water ligand, the iron atom is five-coordinated with His-25 and four pyrrole nitrogen atoms. The coordination geometry deviates considerably from a square-pyramid, suggesting that the iron may be readily dissociated. I speculate that the opened conformation of the heme pocket facilitates sequential product release, first iron then biliverdin, and that owing to biliverdin's increased flexibility iron release triggers its slow dissociation.

MATERIALS AND METHODS

Preparation of the biliverdin(Fe)-HO-1 crystal. Biliverdin(Fe)-HO-1 crystals were prepared by soaking CN^--heme-HO-1 crystals, which were prepared as shown in the section 2.1, in a solution of 4 M sodium formate and 50 mM potassium phosphate (pH 7.4), with 100 mM sodium ascorbate as the reducing agent, until the crystal color changed to green (about 3 hours) (Figure 4-1). A small crystal (50 μm wide) was used for the data collection because large crystals (more than 100 μm wide) were apt to crack or dissolve during preparation.

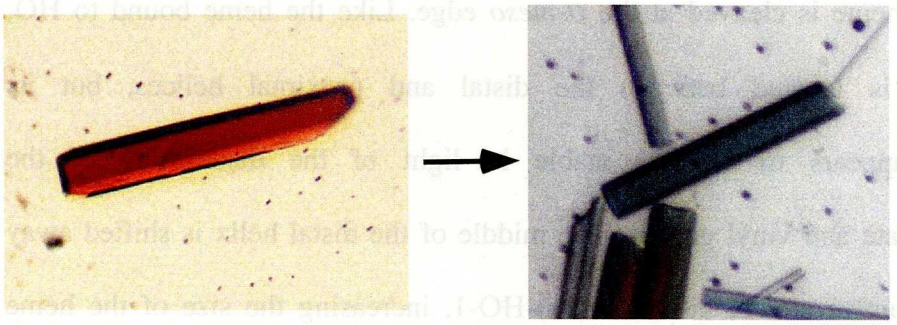

Figure 4-1. **HO reaction in crystal**

Data Collection and Processing. The biliverdin(Fe)-HO-1 crystal was held in a cryo-loop and flash-cooled in a nitrogen gas stream at 100 K. Diffraction data were collected at 100 K using synchrotron radiation (λ = 1.000 Å) at the beamline BL41XU of SPring-8 and a MarCCD system. The crystal to CCD distance was 130 mm. The crystal was oscillated 1.5° with an exposure time of 40 s per frame, the total measurement angle being 120°. Diffraction data were processed, merged, and scaled with MOSFLM (56) and SCALA (57,58). Crystallographic data and diffraction statistics are given in Table 3.

Model building and Refinement. Because the biliverdin(Fe)-HO-1 crystal was isomorphous with the CN^--heme-HO-1 crystal, the structure of biliverdin(Fe)-HO-1 was determined using the structure of the protein moiety of CN^--heme-HO-1 (39). Rigid-body, simulated annealing, and temperature-factor refinements were applied to the model using the 50.0 - 2.4 Å resolution data. XtalView (78) was used to revise the structure. In this step, the cleaved tetrapyrrole ring was clearly visible in the electron density map. After one cycle of

water picking and energy minimization refinement, an additional electron density appeared around the N-terminal residue (Gln-11), to which the model from Ser-7 to Ser-10 was fitted. After one cycle of water picking, energy minimization, and temperature-factor refinements, the model of biliverdin(Fe) moiety was fitted to the σ_A weighted F_o-F_c map in the hemepocket. Lastly, energy minimization and temperature-factor refinements were applied to the model, including biliverdin(Fe). Neither the torsion angles of the tetrapyrrole rings in the biliverdin(Fe) moiety nor the coordination bonds to the heme iron were restrained in the refinements. All refinements were done with CNS (60). The stereo-chemical check of the model was carried out with PROCHECK (57,63). Refinement statistics are given in Table 3.

Table 3 Summary of crystallographic statistics of biliverdin(Fe)-HO

Crystallographic data	
Crystal system	Trigonal
Space group	$P3_221$
Unit cell dimensions (Å)	$a = b = 65.4$, $c = 121.3$
No. of molecules in an asymmetric unit	1
Diffraction statistics	
Resolution range (Å)	50-2.4
No. of observations	88285
No. of unique reflections	12207
Redundancy	7.2
Completeness (%)*	99.7 (99.7)
Mean I_o/σ	7.1 (2.2)
R_{sym}†,*	0.090 (0.343)
Refinement statistics	
R/R_{free}††	0.194/0.239
No. of protein/biliverdin(Fe) atoms	1729/40
No. of water molecules	74
Rms deviations from ideality	
bond lengths (Å)	0.006
angles (deg)	1.14
Ramachandran plot	
Most favored (%)	92.7
Additionally allowed (%)	7.3

† $R_{sym} = \Sigma_{hkl}\Sigma_i |I_i(hkl) - \langle I(hkl)\rangle| / \Sigma_{hkl}\Sigma_i I_i(hkl)$, $\langle I(hkl)\rangle$ is the mean intensity for multiple recorded reflections.

†† $R = \Sigma|F_{obs}(hkl) - F_{calc}(hkl) / \Sigma|F_{obs}(hkl)|$.

Each R_{free} is the R value calculated for ten percent of the dataset not included in the refinement.

* Values in parentheses are for the outermost shell (2.53-2.40Å).

RESULTS

Protein Structure. The structure of biliverdin(Fe)-HO-1 was refined using 2.4 Å resolution data to the R factor of 0.194 and the free R factor of 0.239. Six residues at the N-terminus and 46 residues at the C-terminus are disordered in the biliverdin(Fe)-HO-1 crystal. Main-chain atoms from Ser-7 to Met-9 were ordered as compared to heme-HO-1, but the side-chain of Met-9 was disordered. The structure of biliverdin(Fe)-HO-1 consists of eight helices, A through H, and is similar to that of heme-HO-1 (Figure 1-6), the root mean square deviation for Cα atoms being 0.26 Å. The biliverdin(Fe) is wedged between A- and F-helices at a position corresponding to the heme in heme-HO-1. The plot of the deviations of Cα atoms between biliverdin(Fe)-HO-1 and heme-HO-1 (Figure 4-2, *solid line*) shows that residues with a large deviation (> 0.8 Å) are localized in the middle of the F-helix and in the FG and GH loops. These two loops are located on the molecular surface and can easily adopt different conformations depending on the crystal packing force. Indeed, the structures of heme-HO-1 and N_3^--heme-HO-1, although determined from different space groups, differ in the conformation of these two loops, but the rest of their structures are similar. In particular, the heme pocket structure and positions of the water molecules involved in the distal hydrogen-bonding network, considered essential for catalysis (81,82), are well conserved as shown in the section 1.2. The plot of the deviations for the Cα atoms between biliverdin(Fe)-HO-1 and N_3^--heme-HO-1 (Figure 4-2, *dashed line*) (both isomorphous crystals) shows a large deviation only in the middle of the F-helix. Therefore, essential structural differences between the substrate (heme)- and product (biliverdin(Fe))-bound forms are chiefly restricted to the middle of the F-helix.

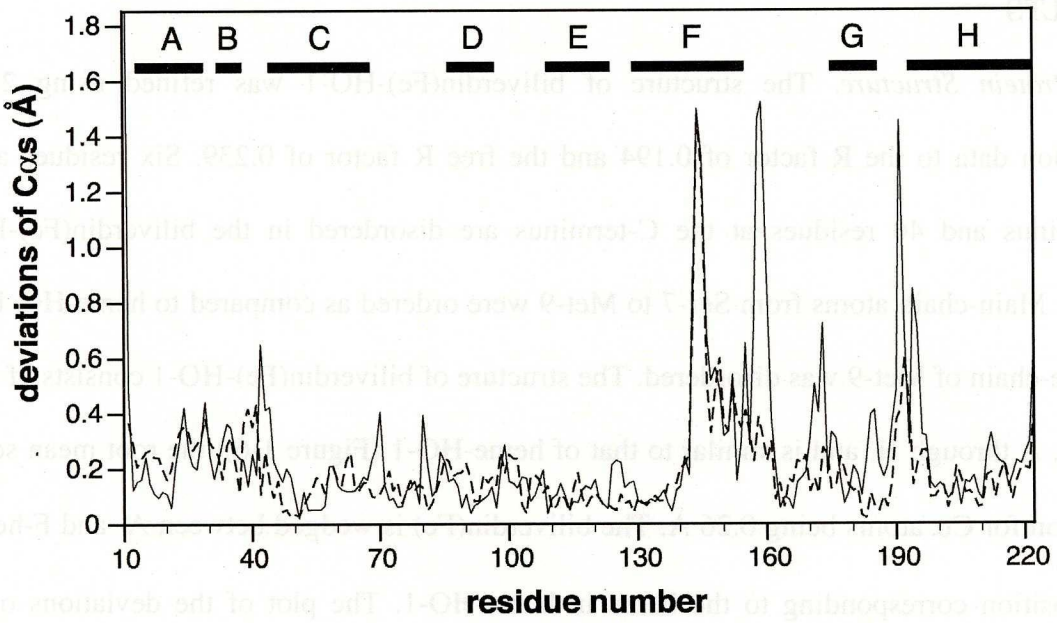

Figure 4-2. **Plots of the deviations of Cα atoms between biliverdin(Fe)-HO-1 and heme-HO-1 (*solid line*) and between biliverdin(Fe)-HO-1 and N_3^--heme-HO-1 (*dashed line*).** Solid horizontal bars represent the helices in heme-HO-1.

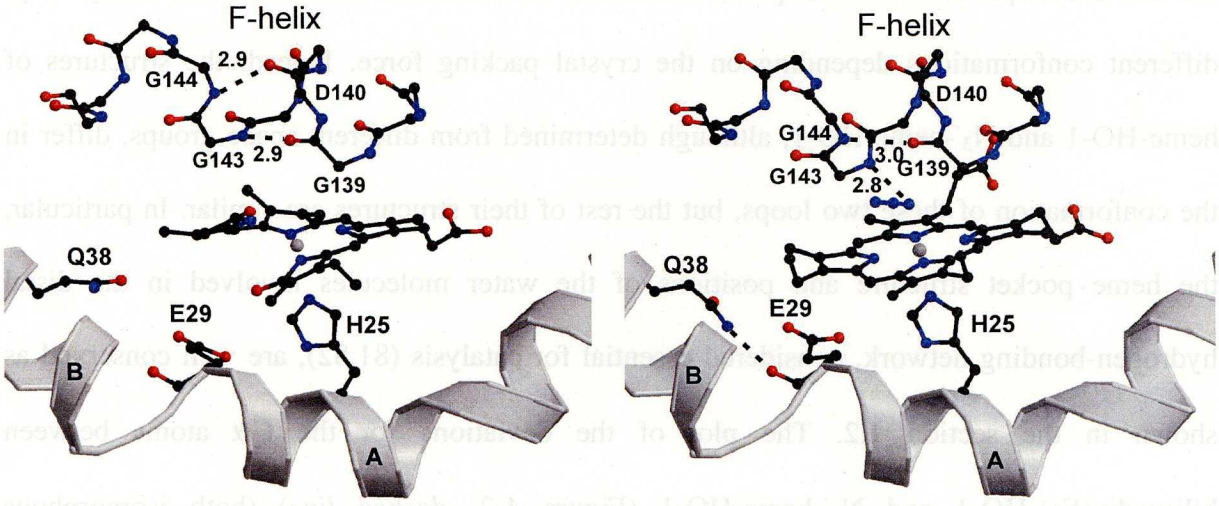

Figure 4-3. **Comparison of the hemepocket structures of biliverdin(Fe)-HO and N_3^--heme-HO-1.** Ball and stick models of the hemepockets of biliverdin(Fe)-HO (*left*) and N_3^--heme-HO (*right*). For clarity, in the F-helix only main-chain atoms are shown. Dashed lines indicate hydrogen bonds that stabilize the two conformers. Numerals show distances between atoms in angstrom units. This figure was prepared with MOLSCRIPT (125) and RASTER3D (126).

Table 4 Selected distances (Å) of atoms at the distal heme pocket.

		G139 O–Fe	G143 N–Fe	G139 O –G143 N	G139 O –G144 N	D140 O –G144 N
rat	biliverdin(Fe)-HO	4.9	5.2	2.9	3.8	2.8
	heme-HO	5.1	4.3	3.1	2.9	3.8
	N_3^--heme-HO	5.0	4.3	3.2	3.0	3.8
human	heme-HO closed form	4.8	5.3	3.2	4.3	3.1
	heme-HO opened form	4.9	6.0	3.1	4.8	2.9

Distal helix. The F-helix of biliverdin(Fe)-HO-1 was bent (~50°) at Leu-141 and Ser-142, as in heme-HO-1 and N_3^--heme-HO-1, but the middle of the helix, Gly-143 to Gln-145, was shifted away from the heme pocket as compared to that in heme-HO-1 and N_3^--heme-HO-1. The distance between Gly-143 N and the iron atom was elongated by 0.9 Å in biliverdin(Fe)-HO-1 as compared to that in heme-HO-1 and N_3^--heme-HO-1, whereas the distance between Gly-139 O and the iron atom showed no change in the three structures (Table 4). Notably, in biliverdin(Fe)-HO-1 the amide group of Gly-143 was directed toward the carbonyl group of Gly-139, forming an α-helical hydrogen-bond (2.9 Å). The backbones of Gly-144 and Asp-140 were also hydrogen-bonded (2.8 Å) (Figure 4-3, *left*). In N_3^--heme-HO-1, however, the amide group of Gly-143 is pointed toward the distal ligand forming a hydrogen bond (2.8 Å), and the amide group of Gly-144 and the carbonyl group of Gly-139 face each other at a distance suitable for hydrogen-bonding (3.0 Å). Moreover, the distance between Gly-144 N and Asp-140 O (3.8 Å) is too great to form a hydrogen bond (Figure 4-3, *right*). This unique conformation is also observed in heme-HO-1 (36).

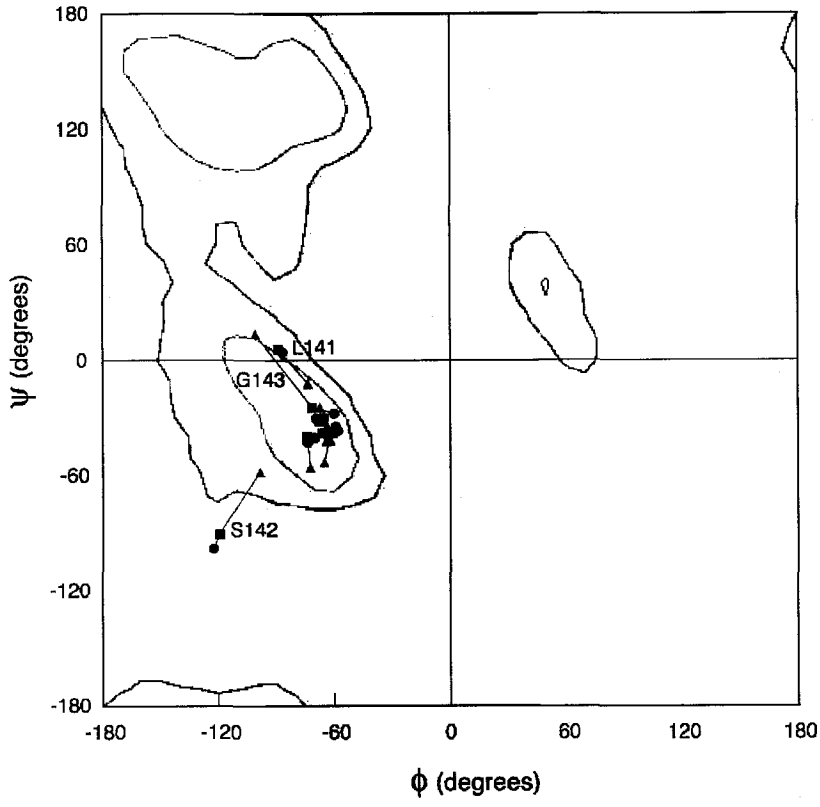

Figure 4-4. **Ramachandran plot for residues around the kinked point of the distal helix.** Plots of Leu-138 through Val-146 residues are joined within the corresponding residues of heme-HO (n), N_3^--heme-HO (l), biliverdin(Fe)-HO (▲).

Ramachandran plots (85) for the residues from Leu-138 to Val-146 may clarify the difference in the F-helix conformations between heme-HO-1 and biliverdin(Fe)-HO-1 (Figure 4-4). In heme-HO-1 and N_3^--heme-HO-1, all the residues examined fell within the region for a right-handed α-helical conformation except for Leu-141 ((ϕ, ψ) = (-89°, 6°) in heme-HO-1, (ϕ, ψ) = (-87°, 4°) in N_3^--heme-HO-1) and Ser-142 ((ϕ, ψ) = (-120°, -90°) in heme-HO-1, (ϕ, ψ) = (-123°, -98°) in N_3^--heme-HO-1); the former was on the periphery of the α-helical region and the latter was outside of the region. Leu-141 ((ϕ, ψ) = (-74°, -12°)) in biliverdin(Fe)-HO-1, was also on the periphery of the region, but the dihedral angles of Ser-142 ((ϕ, ψ) = (-98°, -58°)) less deviated from the α-helical region as compared to those in heme-HO-1 and N_3^--heme-HO-1. Furthermore, the dihedral angles of the following Gly-143 ((ϕ, ψ) = (-101°, -14°)) differed distinctly from those of heme-HO-1 and N_3^--heme-HO-1 ((ϕ, ψ) = (-71°, -25°) in heme-HO-1, (ϕ, ψ) = (-60°, -28°) in N_3^--heme-HO-1). The dihedral angles of the other biliverdin(Fe)-HO-1 residues were similar to those in heme-HO-1 and

N_3^--heme-HO-1. That is, the deviations of the dihedral angles between the heme and biliverdin(Fe) complexes with HO are limited to two consecutive amino acid residues, Ser-142 and Gly-143. Thus, the conformational change in the backbone at these residues in biliverdin(Fe)-HO-1 caused the outward shift of F-helix from the heme pocket after this kink and also brings about rearrangement of the hydrogen bonds in the kinked region.

Proximal helix. The proximal helix of biliverdin(Fe)-HO-1 is shifted slightly away from the heme pocket as compared to the helices in heme-HO-1 and N_3^--heme-HO-1. The His-25 ligand of biliverdin(Fe)-HO-1 maintains a conformation similar to those of heme-HO-1 and N_3^--heme-HO-1, and the distance between the iron chelated by biliverdin and Nε of His-25 (2.4 Å) is roughly comparable to the corresponding distances in heme-HO-1 (2.3 Å) and N_3^--heme-HO-1 (2.1 Å) (Figure 4-3). In heme-HO-1 and N_3^--heme-HO-1, the amide side-chain of Gln-38 of the B-helix is close enough to form a hydrogen bond with the carbonyl group of the backbone of Glu-29 in the A-helix (2.9 Å in heme-HO-1, 2.7 Å in N_3^--heme-HO-1), indicative that it contributes to fixing the two helices on the proximal side of the heme. In biliverdin(Fe)-HO-1, however, the side-chain of Gln-38 is no longer hydrogen-bonded to the main-chain of Glu-29 (distance between Gln-38 Nε and Glu-29 O is 4.4 Å) and has moved closer to the pyrrole ring-A of biliverdin(Fe). A similar conformational change in the side-chain of Gln-38 occurs in apo-HO as shown in the section 1.1.

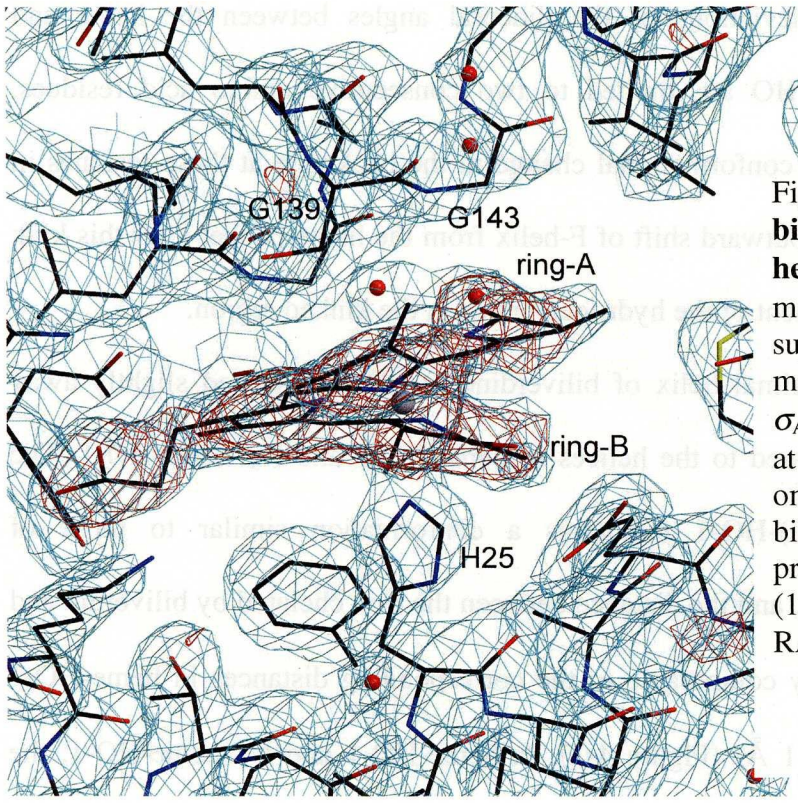

Figure 4-5. **Electron density of biliverdin(Fe)-HO around the hemepocket.** σ_A weighted $2F_o$-F_c map contoured at 1.2σ (*cyan*) superimposed on the wire-frame model of biliverdin(Fe)-HO. The σ_A weighted F_o-F_c map contoured at 3.5σ (*red*) was calculated by omitting the contribution of biliverdin(Fe). This figure was prepared with MOLSCRIPT (125), CONSCRIPT (127), and RASTER3D (126).

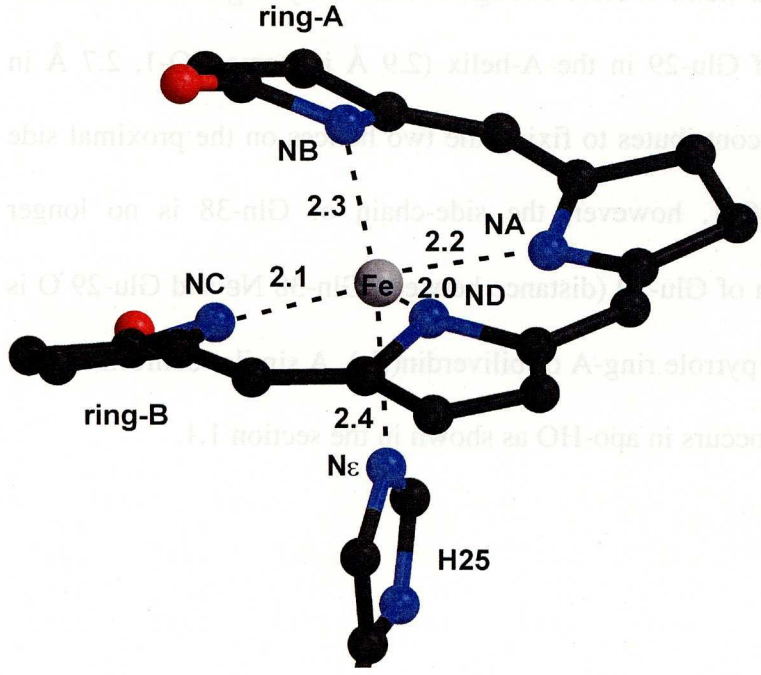

Figure 4-6. **Coordination geometry of the iron atom in biliverdin(Fe)-HO-1.** Dashed lines indicate coordination bonds to the iron. Numerals show distances between atoms in angstrom units. Side chains of biliverdin(Fe) were not shown for clarity. This figure was prepared with MOLSCRIPT (125) and RASTER3D (126).

Biliverdin-iron cheleate structure. The wire-frame model around the hemepocket of biliverdin(Fe)-HO-1 is shown in Figure 4-5. The F_o-F_c map was clearly assignable to the electron density of biliverdin(Fe), consistent with the fact that heme cleavage occurs at the

α-*meso* carbon. One propionate group of the biliverdin(Fe) adopted the same conformation as that of the heme in heme-HO-1 and was buried in the heme pocket, whereas the other group, which is exposed to the solvent in heme-HO-1, was disordered. The vinyl group of pyrrole ring-A, which is also exposed to solvent in heme-HO-1, was not visible. In addition, the temperature factors for the ring-A atoms are higher than those for the other three rings' atoms. Taking into account that all four pyrrole rings of the heme in heme-HO-1 have similar temperature factors, the biliverdin(Fe) in biliverdin(Fe)-HO-1 appears to be accommodated less tightly in the heme pocket than the heme in heme-HO-1. Biliverdin was in helical conformation with the lactam oxygen atoms of ring-A and ring-B that respectively point upward and downward. By nature, biliverdin assumes a helical structure to avoid collision with the lactam oxygen atoms. The helical pitch of the biliverdin in biliverdin(Fe)-HO-1, defined as the distance between the two oxygen atoms, was 3.4 Å, comparable to that (3.34 Å) in the crystal structure of biliverdin dimethyl ester (86). A crystallographic study of the iron(III) complex of octaethylbilindione (OEB) (87), a chemical model of biliverdin(Fe), showed that it forms a dimeric structure, $\{Fe^{III}(OEB)\}_2$, in which each iron is five-coordinate with bonds to four nitrogen atoms in one tetrapyrrole unit and with a bond to a lactam oxygen atom in the partner. Each OEB molecule in $\{Fe^{III}(OEB)\}_2$ has the analogous helical pitch of 3.22 Å, but relatively shorter helical pitches have been reported in biliverdin crystallized with proteins; for apoMb (88), 2.9-3.0 Å and biliverdin IXβ reductase (89), 2.8 Å. The iron atom in biliverdin(Fe) has no distal ligand, unlike the heme iron of heme-HO-1 whose distal ligand is a water molecule or hydroxide. The coordination geometry to the iron atom is shown in Figure 4-6. The distances between the iron atom and the nitrogen atoms of the four pyrrole rings vary considerably, from 2.0 to 2.3 Å, as do the coordination angles of the four nitrogen atoms about the Fe-Nε axis (N_A-Fe-Nε; 91.4°, N_B-Nε-Fe; 130.9°, N_C-Fe-Nε; 84.5°, N_D-Fe-Nε; 96.3°). This asymmetry of the iron coordination reflects the distorted helical

structure of the biliverdin in biliverdin(Fe)-HO-1; the exposed ring-A deviates markedly from the mean plane through the biliverdin(Fe) molecule to the distal side, whereas the buried ring-B is shifted slightly from the plane to the proximal side.

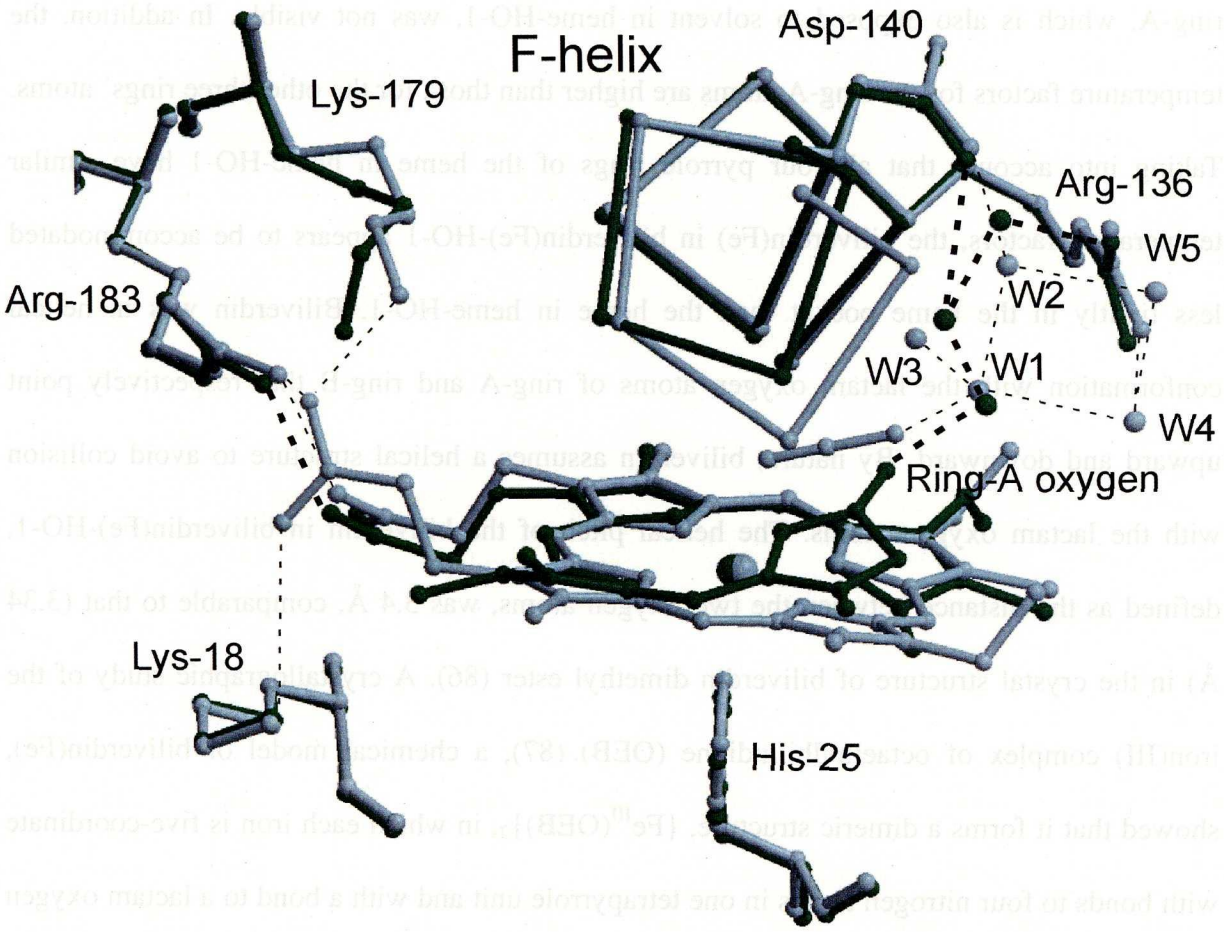

Figure 4-7. **Comparison of the distal hydrogen bond networks in biliverdin(Fe)-HO (*green*) and N_3^--heme-HO (*light blue*).** W1 through W5 indicate the water molecules in N_3^--heme-HO. Dashed lines indicate hydrogen bonds (*thin lines*: in N_3^--heme-HO, *bold lines*: in biliverdin(Fe)-HO). This figure was prepared with MOLSCRIPT (125) and RASTER3D (126).

Protein-biliverdin interactions. In biliverdin(Fe)-HO-1, the carbonyl group of Gly-139 and the amide group of Gly-143 are no longer in contact with the iron atom due to the outward shift of the F-helix and absence of the distal ligand. The α-*meso* edge of the heme in heme-HO-1 faces a hydrophobic wall formed by Met-34, Phe-37, and Phe-214. These residues remain unchanged in biliverdin(Fe)-HO-1. On the opposite side of the heme in

heme-HO-1, Lys-179, Arg-183, and Lys-18 interact electrostatically with the propionate groups of the heme. In biliverdin(Fe)-HO-1, despite disordering of one of the two propionate groups, these basic residues retain conformations similar to those in heme-HO-1. In the distal heme pocket of heme-HO-1, five water molecules (W1~W5) form a hydrogen-bonding network with Asp-140, Arg-136, and Thr-135. This network is completely conserved in N_3^--heme-HO-1, and W1 is hydrogen bonded with the azide ligand (Figure 4-7). In biliverdin(Fe)-HO-1, three of the five water molecules (W1~W3) form a hydrogen-bonding network with Asp-140 and Arg-136 (Figure 4-7). It should be noted that W1 in biliverdin(Fe)-HO-1 is close enough to form a hydrogen bond (2.6 Å) with the ring-A oxygen of biliverdin. On the proximal side of biliverdin there are no water molecules, and the ring-B oxygen does not interact with the protein moieties.

DISCUSSION

Conformational change in the distal helix. One of the intriguing features of the HO-1 structure is the kinked conformation of the distal F-helix, which furnishes α-selectivity to the HO reaction (36,39-41). This helix is in close contact with the heme in the holo state (36,39) but partially fluctuates in the apo state (90), indicative that the flexibility of this helix facilitates both substrate binding and product release. The biliverdin(Fe)-HO-1 structure presented here clearly shows that the conformation of F-helix changes to open the heme pocket when the α-*meso* edge of heme is cleaved. This is the first evidence that conformational change in the F-helix actually occurs during the HO reaction. The amide group of Gly-143 is in close contact with the heme distal ligand in heme-HO-1, whereas in biliverdin(Fe)-HO-1 its direction is altered to form a hydrogen bond with the carbonyl group of Gly-139, resulting in the outward shift of Gly-143 and the next several residues from the heme pocket. This movement is attributable to steric hindrance between F-helix and pyrrole

ring-A; Gly-143 will collide with ring-A unless the backbone conformation of the F-helix changes. Another possible factor for re-direction of the amide bond of Gly-143 in biliverdin(Fe)-HO-1 is loss of the distal water ligand in biliverdin(Fe). Such ligand-dependent conformational changes are consistent with the presence of two conformers, opened and closed forms, in an asymmetric unit of human heme-HO-1 crystals (40) grown at pH 7.5, which is near the pK_a of the water ligand bound to the heme iron. Previous RR studies of heme-HO-1 complexes suggested that the distal ligand exchange from water to hydroxide occurs at pK_a, accompanied by high-to-low spin transition of the heme iron (28,29).

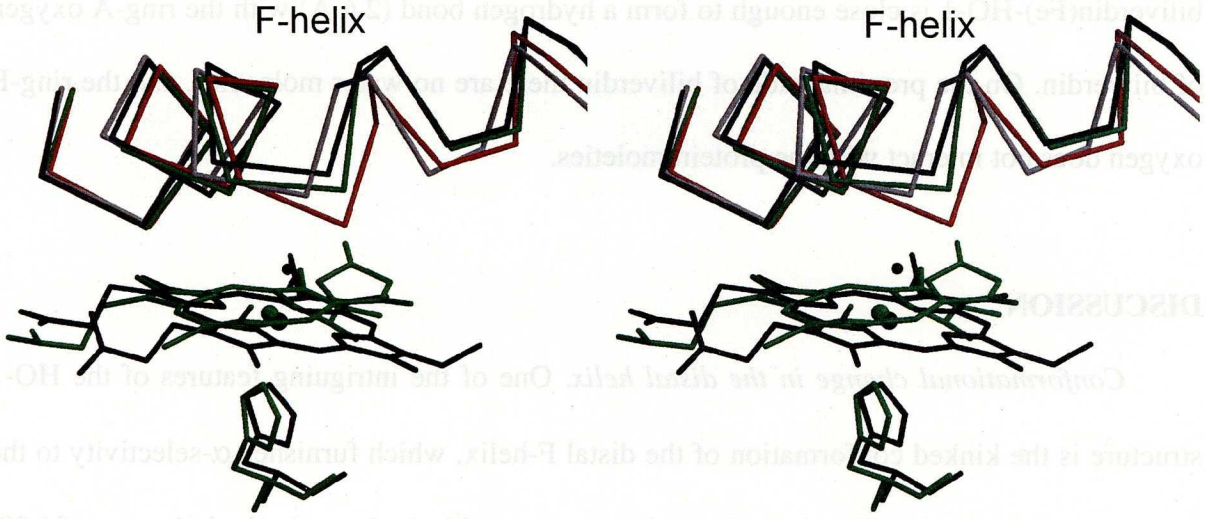

Figure 4-8. **Superimposition of Cα traces of the distal helices of biliverdin(Fe)-HO (*green*), N_3^--heme-HO (*red*), and the closed (*gray*) and opened (*black*) forms of human heme-HO.** Wire-frame models of biliverdin(Fe) and His-25 in biliverdin(Fe)-HO are shown as well as the heme and heme ligands in the human heme-HO-1 open form. All models were superimposed to minimize the rms deviations of Cαs of all the amino acid residues. This figure was prepared with MOLSCRIPT (125) and RASTER3D (126).

Comparison with human HO-1 structures. Structural comparison of biliverdin(Fe)-HO-1 with human heme-HO-1 molecules (Figure 4-8) shows that the distal helix conformation of biliverdin(Fe)-HO-1 is similar to that of the open form (molecule B) of human heme-HO-1, consistent with the fact that this human iso-form has an open heme pocket with loose interaction between the distal helix and heme (40). In this iso-form, as in

biliverdin(Fe)-HO-1, hydrogen bonds are formed between Gly-139 O and Gly-143 N and between Asp-140 O and Gly-144 N (Figure 4-3, Table 4). Interestingly, the distal helix of the other human iso-form, the closed form (molecule A), has a conformation similar to that in biliverdin(Fe)-HO-1 rather than to the conformations in heme-HO-1 and N_3^--heme-HO-1. No hydrogen bond exists between Gly-139 O and Gly-144 N in either human HO-1 iso-form. This agrees with contacts between the distal helix and heme being less tight in the human HO-1 closed form as compared with rat HO-1 complexes with heme. The human closed form therefore is considered to be a conformation intermediate between that of the rat heme-HO-1 and human opened form (36,40), and the biliverdin(Fe)-HO-1 structure should be in the conformational group with an open heme pocket.

Dissociations of iron and biliverdin. Iron release is believed to occur before biliverdin dissociation (25). The coordination geometry of the iron in biliverdin(Fe)-HO-1 showed substantial distortion from either of the two ideal forms, square-pyramid and trigonal-bipyramid, for five-coordinate metal clusters, indicative of the susceptibility to lose iron. The iron coordination in $\{Fe^{III}(OEB)\}_2$ (87) approximates a trigonal-bipyramid, but that compound is readily demetalated; the iron site has a partial occupancy of 0.56, therefore the crystal is apparently comprised of a mixture of $\{Fe^{III}(OEB)\}_2$ and $\{Fe^{III}(OEB)\ (H_2OEB)\}$ wherein one of the iron ions is lost. Although the iron site was fully occupied in the biliverdin(Fe)-HO-1 crystal we studied, iron was partially lost when the crystal was over-incubated with sodium ascorbate. Conceivably, the distorted geometry of iron coordination in biliverdin(Fe)-HO-1 could facilitate the release of the iron from biliverdin(Fe). Based on early work on the degradation of the heme bound to HO in a reaction system with ascorbate (25), the iron in the biliverdin(Fe)-HO-1 crystal is probably in the ferric state. A kinetic study of the HO reaction (91) showed that product release from HO first requires the reduction of Fe^{3+}-biliverdin to Fe^{2+}-biliverdin; on reduction of iron, rapid release of iron

occurs and the slower dissociation of biliverdin follows. Reduction of the iron in biliverdin(Fe)-HO-1 may not affect its distorted geometry because the iron(II) complex of a methoxy derivative of OEB, $\{Fe^{II}(OEBOMe)\}_2$ (92), has a structure very similar to that of $\{Fe^{III}(OEB)\}_2$. The superior solubility of ferrous to ferric iron may be favorable for iron release (91,93).

The nature of the binding of biliverdin(Fe) in the heme pocket of HO, together with the structure of the heme pocket in the apo state (90), gives an insight into a possible mechanism for the final product release from the enzyme. Upward movement of the distal helix and relaxation of the proximal helix allow the active site to be opened, but several residues (Met-34, Phe-37, Phe-214, Lys-179, and Arg-183) that surround the biliverdin(Fe) in biliverdin(Fe)-HO-1 have conformations similar to those in heme-HO-1 and N_3^--heme-HO-1. Conserved interactions between the biliverdin(Fe) and protein moieties of HO are consistent with the finding that even in the apo state these residues roughly retain their conformations. The position of biliverdin(Fe) also remains unchanged in comparison to the heme positions in heme-HO-1 and N_3^--heme-HO-1. The binding of biliverdin(Fe) in the heme-HO pocket, however, is less tight than that of the heme; the porpionate and vinyl groups that are exposed to the solvent are invisible in biliverdin(Fe)-HO-1. The loose accommodation of biliverdin is accounted for by the opened conformation of the distal helix and the decreased rigidity of the tetrapyrrole due to α-*meso* cleavage. As stated above, the helical pitch of the biliverdin(Fe) in biliverdin(Fe)-HO-1 is longer than that of the biliverdin bound to apoMb (88). In contrast to the partial exposure of the biliverdin in biliverdin(Fe)-HO-1, the biliverdin in the biliverdin-apoMb complex is buried in the Mb heme pocket. Comparison of both biliverdin structures bound to proteins shows the marked deviation of ring-A from the mean plane of the tetrapyrrole in biliverdin(Fe)-HO-1, indicative that interaction between the ring-A oxygen atom and distal hydrogen-bonding network produces the distorted helical structure of

biliverdin(Fe). Upon release of the iron, the mechanism of which is unknown, the proximal helix should be more relaxed owing to loss of the coordination bond between the iron and His-25. Iron release therefore would render biliverdin more flexible, impelling it to a less stable accommodation state in the heme pocket. Therefore, the final product release would be mainly caused by the increased flexibility of biliverdin assisted by the widening of the active site. This scheme suggests slow dissociation of biliverdin from the HO active site, which is consistent with the finding that biliverdin release is the rate-limiting step of single turnover in the HO reaction (91,93).

1.4 Conclusions

I determined rat HO-1 structures of apo-state, azide bound heme complex, as an analog of hydrogen peroxide bound heme complex intermediate, and biliverdin-iron chelate complex. ApoHO structure shows the fluctuation of A- and F-helices, components of hemepocket, is caused by lack of heme. Hydrogen bond between Gln-38 and Glu-29 may be a key to fix the HO structure on binding heme. This hydrogen bond is also disrupted in biliverdin-iron chelate complex, indicative of the importance of this bond on substrate binding and product release. Azide bound heme complex structure clearly indicates that the distal ligand bound to heme is directed to the α-*meso* position of heme and that is mainly caused by steric hindrance by unique bending of F-helix. This crucially determines regiospecificity of HO reaction. Hydrogen bonding between azide and water molecules in hemepocket also contributes to fixing the direction of distal ligand, but these water molecules would be involved in the activation of molecular oxygen. Biliverdin-iron chelate complex structure demonstrates that HO reaction really proceeds in crystal as in solution, indicating that rat HO-1 in crystal keeps its activity. Highly distorted structure of biliverdin-iron chelate suggests that iron is easily released to solvent on iron reduction to solubilize in water. The open conformation of F-helix and the disruption of hydrogen bond between Gln-38 and Glu-29 in HO-biliverdin(Fe) may contribute to smooth release of biliverdin. The structures of these reaction intermediate gave a lot of insights in HO reaction, but the structural basis for the steps from α-hydroxyheme to biliverdin-iron chelate is not given. The structures of α-hydroxyheme and verdoheme complexes would be required for further investigation.

Chapter 2

Mechanism of escaping from product inhibition in HO

INTRODUCTION

Chapter 2 deals with the mechanism how HO discriminates between CO and O_2. In HO reaction, CO is produced in its second step (Figure 1-3). HO must proceed its reaction in the atmosphere where CO is locally concentrated, thus the active site of HO may be equipped with a variety of structural devices that allow HO to escape from inhibition by CO.

The affinities of such ligands as CO and O_2 for the heme iron in hemoproteins vary markedly depending on the heme environment. For free heme in organic solvents, the ratio of the CO and O_2 affinities to the heme iron, the ratio of the CO equilibrium constant (K_{CO}) to the O_2 equilibrium constant (K_{O2}), is about 30,000-100,000 (34,94), whereas in Mb, K_{CO}/K_{O2} is 25-41 (34). A number of structural analyses of oxy and carbomonoxy Mb have shown that the discrimination between CO and O_2 by Mb is primarily due to hydrogen-bonding and other polar interactions rather than steric hindrance (34,95-100). Neutron diffraction crystallographic analysis of both forms of Mb indicates that on O_2 binding to the heme in Mb, the Nε atom of the distal histidine (His E7) is protonated and O_2 forms a hydrogen bond with His E7 (96), whereas His E7 Nδ is protonated on CO binding (97). Recent site-directed mutagenesis and spectroscopic analyses, however, suggest that His E7 Nε is protonated and hydrogen bonded to the distal ligand in both ligand-bound forms (98,99). If so, the electrostatic field calculation of heme pocket of Mb indicates good correlations between the electrostatic potentials of the distal ligand, the stretching frequencies of infrared absroption and RR, and the dissociation rate constants of both ligands in wild-type and mutant Mbs (100). Distal pocket polarity therefore would be a key for discrimination between polar O_2 and apolar CO in Mb.

Studies of O_2 and CO bindings to heme-HO, as compared with those of Mb, reported by Ikeda-Saito *et al.* (35), seem exceedingly important; O_2 affinities are very high (K_{O2} = 30-80 μM^{-1}), 30- to 90-fold those for Mb. The O_2 association rate constants are similar to those for Mb (k'_{O2} = 7-20 $\mu M^{-1}s^{-1}$), whereas O_2 dissociation rate constants are remarkably slow (k_{O2} = 0.25 s^{-1}), suggestive of the presence of favorable interactions between the bound O_2 and protein residues in the heme pocket. In contrast, the CO affinity of heme-HO is reported to be similar to that of Mb (35). CO binding to the heme bound to HO is biphasic. The respective K_{CO}/K_{O2} ratios are 5.4 and 1.2 for the fast and slow phases. Thus, HO discriminates much more strongly against CO binding with increased affinity for O_2 than Mb does.

In the first section, I discuss the mechanisms of discrimination between CO and O_2 in heme-HO. The binding geometry of the ligand to the heme iron, in case of end-on binding, is primarily determined by its shape of highest occupied molecular orbiltal (Figure 5-1). This theory predicts that the binding mode of O_2 is similar to that of N_3^- and that of NO, while that of CO is similar to that of CN^-. Indeed, RR spectroscopic analysis has given an angle of nearly 110° for $Fe^{2+}\cdots$ O-O (50) and the bending angle of N_3^- is 116° as described in the section 1.2. To obtain the structural basis of the severe discrimination between O_2 and CO in heme-HO, I determined the structures of ferrous heme-HO, CO-heme-HO, CN^--heme-HO, and NO-heme-HO.

In the second section, I demonstrate the novel mode of cyanide binding in heme-HO. The fact that cyanide binds to the heme iron in unstable fashion at neutral pH suggests the steric contribution of the distal helix to the ligand discrimination depending on its binding mode.

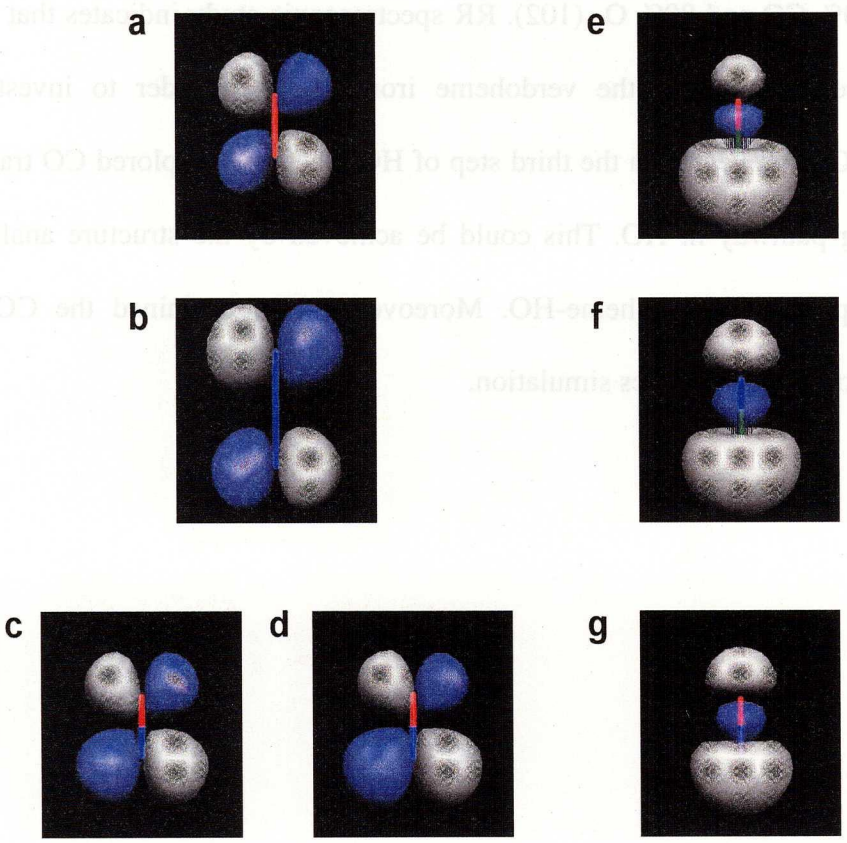

Figure 5-1. **Highest occupied molecular orbital (HOMO) of possible heme ligands.** Fe·· ligand angle is primarily determined by the shape of HOMO of ligand. Each figure shows ligand (stick model, carbon; green, nitrogen; blue, oxygen; red) and its HOMO (sphere). The orbital color shows the each direction of electron spin. Molecular orbitals were caluculated with the program GAMESS (129). a; O_2, b; N_3^-, c; NO (neutral radical), d; NO^-, e; CO, f; CN^-, g; NO^+.

In the third section, I demonstrate the escaping pathway of endogenously produced CO from the hemepocket of HO. One of the notable features of the HO reaction resides in the third step, the oxidation of verdoheme to biliverdin; the reaction can proceed without possible interference by CO that is produced in the second step, the conversion of α-hydroxyheme to verdoheme. The endogenous CO seems never to interfere with the third step in the single turnover reaction (91). A markedly low affinity of CO for the verdoheme bound to HO compared to that for the heme bound to HO (35) would have to do with the mechanism, wherein the possible product inhibition is avoided. However, an excess amount of exogenous CO inhibits the third step; the HO reaction substantially ceases at the verdoheme stage under

a gas phase of 20% CO and 80% O_2 (102). RR spectroscopic study indicates that exogenous CO can be directly bound to the verdoheme iron (103). In order to investigate how interference of CO is prevented in the third step of HO reaction, I explored CO trapping sites and CO releasing pathway in HO. This could be achieved by the structure analysis of the short-time photoproduct of CO-heme-HO. Moreover, I also examined the CO releasing pathway using molecular dynamics simulation.

2.1 Structural basis for the discrimination between molecular oxygen and carbon monoxide in HO

ABSTRACT

Heme oxygenase (HO) catalyzes heme degradation by utilizing O_2 and reducing equivalents to produce biliverdin IXα, iron, and CO. To avoid product inhibition, the heme-HO complex is structured to markedly increase its affinity for O_2 while suppressing its affinity for CO. I determined the crystal structures of rat ferrous heme-HO, heme-HO bound to CO, CN^-, and NO, respectively, at 2.3, 1.8, 2.0, and 1.7 Å resolutions. The heme pocket of ferrous heme-HO has the same conformation as that of the previously determined ferric form, but no ligand is visible on the distal side of the ferrous heme. Fe-CO and Fe-CN^- are tilted, whereas Fe-NO is bent. The structure of heme-HO bound to NO is identical to that bound to N_3^-, which is also bent as in the case of O_2. Notably, in the CO and CN^- bound forms the heme and its ligands shift toward the α-*meso* carbon, and the distal F-helix shifts in the opposite direction. These shifts allow CO or CN^- to bind in tilted fashion without collision between the distal ligand and Gly-139 O and cause disruption of one salt bridge between the heme and basic residue. The structural identity of the ferrous and ferric states of heme-HO indicates that these shifts are not produced on reduction of heme iron. Neither such conformational changes nor a heme shift occurs on NO or N_3^- binding. Heme-HO therefore recognizes CO and O_2 by their binding geometries. The marked reduction of the ratio of CO to O_2 affinities to heme-HO achieved by an increase in O_2 affinity is explained by hydrogen-bonding and polar interactions favorable for O_2 binding, as well as by characteristic structural changes in the CO-bound form.

MATERIALS AND METHODS

Preparation of ferrous heme-HO and ligand-bound crystals. The expression and purification of truncated rat HO-1 (Met1-Pro267), as well as the preparation of its complex with heme, are described in the general introduction (Figure 1-5, (37-39)). Ferric heme-HO was crystallized under conditions similar to those for N_3^--heme-HO with a microcrystal of N_3^--heme-HO as the seed. Ferrous heme-HO crystals were prepared by soaking ferric heme-HO crystals in an anaerobic solution containing an excess amount of sodium dithionite. On reduction, the crystal color immediately became bright red. CN^--heme-HO was prepared by adding potassium cyanide to a ferric heme-HO solution for a final concentration of 10 mM, and crystallized under the same conditions used for N_3^--heme-HO (39), the protein concentration being 40 mg ml^{-1} in 50 mM potassium phosphate buffer (pH 7.0). The CO-heme-HO crystal was prepared by soaking an N_3^--heme-HO crystal in a CO-saturated solution until the crystal became bright red (30 m to 2 h). The CO-saturated solution was prepared just before soaking the crystals; sodium ascorbate at the final concentration of 100 mM was added to the crystallization solution then two cycles of alternate de-gassing (15 m) and CO-bubbling (5 m) were run. The NO-heme-HO crystal was prepared by soaking the N_3^--heme-HO crystal in an NO-saturated solution. The crystal immediately became bright red. The NO-saturated solution was prepared just before soaking the crystals. Sodium dithionite and NOC-12, an NO-donor (Dojindo, Kumamoto, Japan), were added in excess to the crystallization solution, the gas phase of which had been replaced with N_2 in advance by two cycles of alternate de-gassing (15 m) and an N_2-purge (5 m). The ferrous heme-HO, CO-heme-HO and NO-heme-HO crystals on cryo-loop were immediately cooled with liquid nitrogen. The CN^--heme-HO crystal was soaked for a few seconds in crystallization solution that contained 50 mM potassium cyanide, and then the crystal on cryo-loop was flash-cooled under a nitrogen gas stream at 100 K. The CN^--heme-HO crystals became bright red on soaking them in 50 mM potassium cyanide (final pH was 9.2).

Data collection and processing. Diffraction data for the ferrous heme-HO crystal were collected at 100K with an FR-D rotating anode X-ray generator (λ = 1.5418 Å) and R-AXIS IV^{++} imaging plate system (RIGAKU). Its crystal was oscillated by 1.5° per frame at an exposure time of 20 m and total measurement angle of 120°. Diffraction data for CN^--heme-HO were collected at 100 K using synchrotron radiation (λ = 1.000 Å) at the beamline BL40B2 of SPring-8 and an ADSC Quantum 4R detector. Its crystal was oscillated by 1.5° per frame at an exposure time of 120 s and total measurement angle of 60°. Diffraction data for CO-heme-HO and NO-heme-HO were collected at 100 K using synchrotron radiation (λ = 1.000 Å) at the beamline BL41XU of SPring-8 and a MarCCD system. For CO-heme-HO, the crystal was oscillated by 1.5° per frame at an exposure time of 5 s and total measurement angle of 180°. To measure intensities of the overloaded diffractions, the X-ray beam was attenuated to 7%, then the same crystal was oscillated by 3.0° per frame with 3 s exposure. The two datasets were scaled and merged using 50-1.8 Å data for the former and 50-3.5 Å data for the latter. For NO-heme-HO, the exposure time per frame was 6 s and total measurement angle was 120°. To collect low resolution data, the X-ray beam was attenuated to 25%, then intensity data were collected under the same conditions as for CO-heme-HO. The two datasets were scaled and merged using 50-1.7 Å data for the former and 50-3.5 Å data for the latter. These diffraction data were processed, merged, and scaled with MOSFLM (56) and SCALA (57,58) for the ferrous heme-HO and CN^--heme-HO and with HKL2000 (77) for CO-heme-HO and NO-heme-HO. Crystallographic data and diffraction statistics are given in Table 5.

Model building and refinement. Because the CN^--heme-HO crystal was isomorphous with the N_3^--heme-HO crystal (39), its structure was determined by applying rigid body, simulated annealing, and temperature-factor refinements to the structure of its protein moiety using 50.0-2.5 Å resolution data. The structure was revised by alternate adjustment of the

model by XtalView (78) and simulated annealing and temperature-factor refinements using 50.0-2.0 Å resolution data. The heme, clearly present in the electron density map, was included in subsequent refinement. After a few cycles of water picking and energy minimization refinements, the electron density for the stretch of Glu-234~Leu-243 appeared as a separate density and its model was included in subsequent refinement. Lastly, the cyanide ion was located in the F_o-F_c map and included in the energy minimization refinement, in which neither the Fe·· C-N angle nor Fe·· C distance was restrained. The structures of ferrous heme-HO, CO-heme-HO, and NO-heme-HO were refined by the same procedures respectively using 50.0-2.3, 50.0-1.8, and 50.0-1.7 Å resolution data. All the refinements were done with CNS (60). Stereo-chemical checks of the models were made with PROCHECK (57,63). Refinement statistics are given in Table 5.

Table 5 Summary of crystallographic statistics of ferrous heme-HO and heme-HO complexes bound to several ligands

Data set	Ferrous heme-HO	CO-heme-HO	CN^--heme-HO	NO-heme-HO
Space group		$P3_221$		
$a =, b =$	65.3 Å	66.0 Å	65.7 Å	65.4 Å
$c =$	120.5 Å	120.2 Å	119.7 Å	121.1 Å
Resolution (Å)	50-2.3	50-1.8	50-2.0	50-1.7
Unique reflections	13,787	28,853	20,629	32,251
Redundancy	6.4	11.8	3.5	9.5
Completeness (%)[†††]	99.9 (99.9)	99.7 (97.4)	99.3 (99.3)	99.8 (99.5)
R_{merge}[*,†††]	0.102 (0.347)	0.067 (0.315)	0.066 (0.284)	0.052 (0.346)
R/R_{free}[†, ††]	0.186/0.220	0.195/0.214	0.198/0.223	0.201/0.227
Rms deviation from ideality				
bonds (Å)	0.006	0.005	0.006	0.005
angles (°)	1.14	1.24	1.19	1.12
Average B-factors (Å^2)				
main chain	24.7	23.5	23.7	26.5
Side chain	27.2	27.2	26.8	29.5
solvent	35.6	36.7	34.2	39.6
heme	26.7	27.3	24.8	30.7
distal ligand	-	24.3	20.6	32.8

[*] $R_{merge} = \Sigma_{hkl}\Sigma_i |I_i(hkl) - \langle I(hkl)\rangle| / \Sigma_{hkl}\Sigma_i I_i(hkl)$

[†] R-factor $= \Sigma||F_{obs}(hkl)| - |F_{calc}(hkl)|| / \Sigma|F_{obs}(hkl)|$

[††] R_{free} : R values calculated for 5% (ferrous heme-HO and NO-heme-HO) and 10% (CO-heme-HO and CN^--heme-HO) of the dataset not included refinements.

[†††] Values in parentheses are for the outermost shell : 2.42-2.30 Å for ferrous heme-HO, 1.86-1.80 Å for CO-heme-HO, 2.07-2.00 Å for CN^--heme-HO, and 1.76-1.70 Å for NO-heme-HO.

RESULTS

Overall structures. The structures of the ferrous heme-HO, CO-heme-HO, CN^--heme-HO, and NO-heme-HO have been refined, respectively, at 2.3 Å resolution to an R/R_{free} of 0.186/0.220; at 1.8 Å resolution to an R/R_{free} of 0.195/0.214; at 2.0 Å resolution to an R/R_{free} of 0.198/0.223; and at 1.7 Å resolution to an R/R_{free} of 0.201/0.227. In CN^--heme-HO, the C-terminal loop (Glu-234~Leu-243) has become ordered, but the side chains of Glu-234 and Arg-237 are still disordered. This loop is located at the back of the

heme pocket. The distance (30 Å) between Thr-222 and Glu-234 indicates that the disordered segment (Glu-223~Thr-233) assumes an extended conformation. The side chain of Lys-177 is disordered in each of the CO-, CN^-- and NO-heme-HO crystals. In CO-heme-HO and NO-heme-HO, the side chain of Glu-190 is disordered. In CO-heme-HO, the side chains of Glu-19 and Glu-45 are also disordered. In NO-heme-HO, there are several alternate conformations for the side chains on the molecular surface and an additional NO molecule near the side chain of Arg-27. In N_3^--heme-HO, an additional azide molecule was also found to bind to the same site (39). In the ferrous heme-HO structure, no electron density is present on the distal side of the heme iron, consistent with previous spectroscopic study findings (29,30,104).

Structural comparisons of the various forms of heme-HO are shown in Figure 5-2. The overall structure of ferrous heme-HO is identical to that of N_3^--heme-HO (39) (Figure 5-2a) and similar to that of ferric heme-HO (36), the respective root mean square (rms) deviations for the Cα atoms being 0.13 and 0.46 Å. The relatively large rms deviation between the ferrous and ferric heme-HOs is mainly due to the different conformations in the FG and GH loops on the molecular surface; the rms deviation is 0.28 Å when these loops are excluded. The space groups of the ferrous and ferric heme-HO crystals differ and these loops are involved in intermolecular contacts. The structural difference in these loops therefore would be due to the crystal packing force. NO-heme-HO also has the same structure as ferrous heme-HO (Figure 5-2a), the rms deviation being 0.13 Å. The heme position remains unchanged on NO binding to the ferrous iron as it does on N_3^- binding to the ferric iron (39). It may be concluded that neither the oxidation state of the heme iron nor substitution of the distal ligand of heme-HO by NO or N_3^- affects the HO structure.

Superimposition of the ferrous heme-HO and CO-heme-HO structures (Figure 5-2b) shows that on CO binding the heme shifts (0.9 Å) toward the α-*meso* carbon along the α-γ

axis of the heme. The plot of deviations for Cα atoms between ferrous heme-HO and CO-heme-HO (Figure 5-2a) shows marked differences in positions of the A-, B-, F-, and G-helices which constitute the heme binding site of HO. In CO-heme-HO, the proximal A- and following B-helices move in the direction of the α-*meso* carbon together with the heme shift, whereas the distal F- and G-helices shift in the opposite direction; e.g., the Cα atoms of His-25 in the A-helix and Gly-143 in the F-helix are located at 0.5 and 1.1 Å, respectively, from their positions in the ferrous heme-HO. Because no significant structural change occurs in the heme pocket on NO binding to the ferrous heme, these heme shift and conformational changes on CO binding are attributable to the difference in the coordination modes of the ligands.

The structure of CN^--heme-HO, as compared with that of the ferrous heme-HO, also shows large deviations at residues located in the heme pocket (Figure 5-2a). It is similar to the structure of CO-heme-HO; the rms deviation for Cα atoms between the CO- and CN^--bound forms is 0.29 Å. The heme shift, accompanied by movement of the A- and B-helices, in the α-*meso* direction, and repositioning of the F- and G-helices occurs in heme-HO-CN^- as it does in CO-heme-HO. Taking the ferric state of the heme iron in CN^--heme-HO into account, it is conceivable that the binding modes of CO and CN^-, not the redox states of the heme iron, are responsible for these conformational changes.

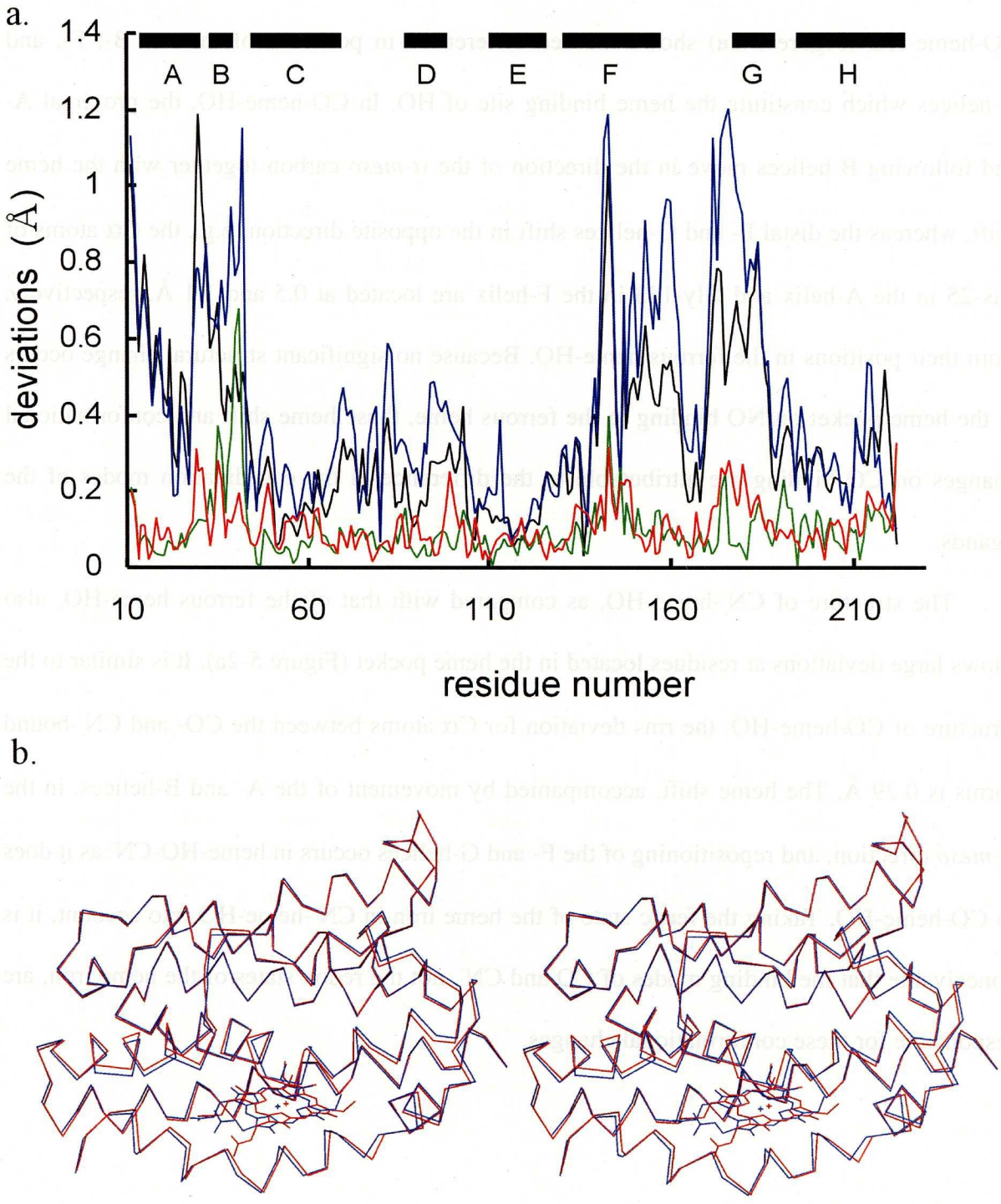

Figure 5-2. **Structural comparisons of various forms of heme-HO.** a. Plots of Cα atom deviations between ferrous heme-HO and ligand-bound heme-HOs; N_3^--heme-HO (*red*), NO-heme-HO (*green*), CO-heme-HO (*black*), and CN^--heme-HO (*blue*). Solid horizontal bars indicate the helices in the ferric heme-HO. b. Stereo diagram of Cα traces of ferrous heme-HO (*blue*) and CO-heme-HO (*red*). The models are superimposed to minimize the rms deviation of the corresponding Cαs of all the amino acid residues. Figure 5-2b was prepared with MOLSCRIPT (125) and RASTER3D (126).

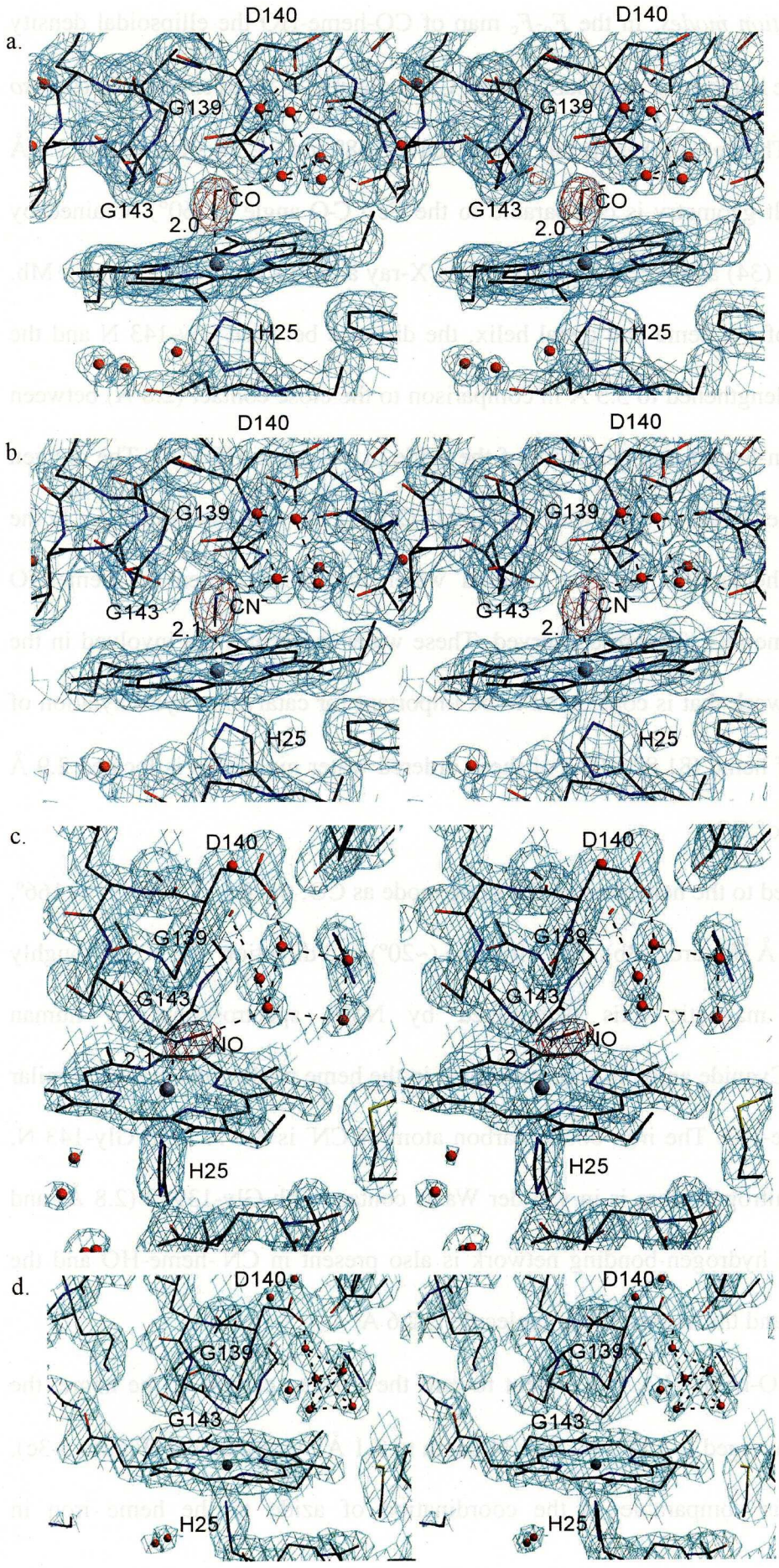

Figure 5-3. **Structures of CO-heme-HO, CN^--heme-HO, NO-heme-HO, and ferrous heme-HO around the heme pockets.** σ_A weighted $2F_o$-F_c (cyan) and F_o-F_c (red) maps superimposed on the wire-frame model are shown in stereo-view. Dashed lines show the hydrogen and coordination bonds involved in stabilization of distal ligand binding. a; CO-heme-HO, b; CN^--heme-HO, c; NO-heme-HO, d; ferrous heme-HO. Each $2F_o$-F_c map is contoured at 1.2 σ, whereas the F_o-F_c map at 5.0 σ was calculated by omitting exogenous ligand bound to the heme iron. Fe···C(CO) and Fe···C(CN^-) distances are in angstrom units. These figures were prepared with MOLSCRIPT (125), CONSCRIPT (127), and RASTER3D (126).

Ligand coordination modes. In the F_o-F_c map of CO-heme-HO the ellipsoidal density on the distal side of the heme iron, assignable to the CO molecule, is tilted toward the α-*meso* carbon (Figure 5-3a). The Fe·· C-O angle has converged to 158° and the Fe·· Clength to 2.0 Å by refinement. This tilt geometry is comparable to the Fe·· C-O angle (~160°) obtained by infrared measurements (34) and recent high-resolution X-ray analysis (95) for CO-bound Mb. Due to repositioning of the heme and distal helix, the distance between Gly-143 N and the carbon atom of CO is lengthened to 3.5 Å in comparison to the close contact (2.8 Å) between Gly-143 N and the iron-bound nitrogen atom of the azide in N_3^--heme-HO (39). The oxygen atom of CO is in van der Waals contact with Gly-139 O (2.9 Å) and Gly-144 N (3.1 Å). In the distal pocket of CO-heme-HO, the five ordered water molecules present in heme-HO (36,40,41) and N_3^--heme-HO (39) are conserved. These water molecules are involved in the hydrogen-bonding network that is considered to be important for catalyzing hydroxylation of the α-*meso* position of heme (81,82). One of these ordered water molecules is located 2.9 Å from the oxygen atom of CO.

CN^- is coordinated to the heme iron in the same mode as CO; the Fe·· C-N angle is 166°, the Fe·· Cdistance 2.1 Å (Figure 5-3b). The tilt angle (~20°) and direction of CN^- are roughly consistent with the magnetic axis determined by NMR spectroscopy for human CN^--heme-HO (105). Cyanide anion is accommodated in the heme pocket in a manner similar to the CO in CO-heme-HO. The iron-bound carbon atom of CN^- is 3.6 Å from Gly-143 N, whereas the terminal nitrogen atom is in van der Waals contact with Gly-139 O (2.8 Å) and Gly-144 N (2.8 Å). A hydrogen-bonding network is also present in CN^--heme-HO and the distance between CN^- and the nearest water molecule is 2.6 Å.

In contrast, in NO-heme-HO, NO is bent toward the α-*meso* carbon of the heme; the Fe·· N-O angle has converged to 125° and Fe·· Nlength to 2.1 Å by refinement (Figure 5-3c). This bent geometry is comparable to the coordination of azide to the heme iron in

N_3^--heme-HO, in which the corresponding angle is 116°and length is 2.2 Å (39). The nitrogen atom of NO is hydrogen-bonded to Gly-143 N (2.8 Å) and in a van der Waals interaction with Gly-139 O (2.9 Å) as is the iron-bound nitrogen of azide in N_3^--heme-HO. The oxygen atom of NO is 2.8 Å from Gly-139 O, 3.2 Å from Gly-144 N, and 2.9 Å from a water molecule in the hydrogen-bonding network.

Water molecules consisting of such distal hydrogen-bonding network are also present in ferrous heme-HO, but the distal ligand is lacking (Figure 5-3d). Electron density for five of the six water molecules in this hydrogen-bonding network is broad (Figure 5-3d), indicative of fluctuation of these water molecules.

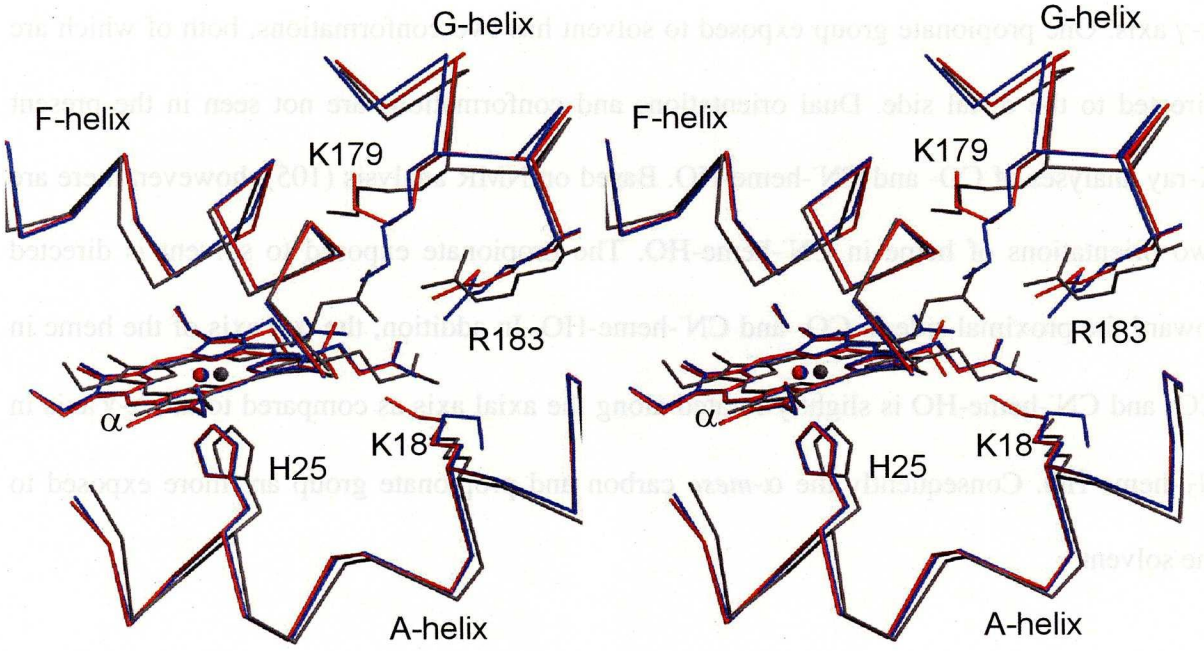

Figure 5-4. **Structural changes on CO binding.** Stereo diagram around the heme pockets of CO-heme-HO (red), CN^--heme-HO (blue), and ferrous heme-HO (gray). The models are superimposed to minimize rms deviations of the Cαs of all the amino acid residues. The A-, F-, and G-helices are shown as Cα traces, and Lys-18, His-25, Lys-179, Arg-183, heme, CO, and CN^- as a wire-frame model. This figure was prepared with MOLSCRIPT (125) and RASTER3D (126).

Interactions of propionate groups with basic residues in the heme pocket. The current structures of the various ligand-binding forms of heme-HO show that the binding modes of

ligands affect the electrostatic interactions of the propionate groups of the heme with side chains that have important roles for the correct accommodation of heme in the active site (36,40). Lys-18, Lys-179, and Arg-183 are clustered near the propionate groups in the ferric (36,40) and ferrous heme-HO complexes and in N_3^--heme-HO (39). The structures of these basic residues are unaffected by the bound NO. The side chains of Lys-179 in CO-heme-HO and Lys-18 in CN^--heme-HO, however, have different conformations and no longer interact with the propionates (Figure 5-4). The present refinement for NO-heme-HO includes only the major orientation of heme, though additional electron density of the heme is observed as in N_3^--heme-HO; the heme has two orientations related to each other by 180° rotation about the α-γ axis. One propionate group exposed to solvent has two conformations, both of which are directed to the distal side. Dual orientations and conformations are not seen in the present X-ray analyses of CO- and CN^--heme-HO. Based on NMR analysis (105), however, there are two orientations of heme in CN^--heme-HO. The propionate exposed to solvent is directed toward the proximal side in CO- and CN^--heme-HO. In addition, the α-γ axis of the heme in CO- and CN^--heme-HO is slightly rotated along the axial axis as compared to the α-γ axis in N_3^--heme-HO. Consequently the α-*meso* carbon and propionate group are more exposed to the solvent.

DISCUSSION

The most notable feature of CO and CN^- binding to the heme bound to HO is gross relocation of the active site accompanied by a heme shift. Although a heme shift on ligand binding has been reported in dimeric clam Hb, it is involved in cooperative ligand binding through residues on the subunit interface that link the heme of one subunit to the proximal helix of the second subunit (106). The tilt geometry of CO or CN^- in the distal pocket of heme-HO would produce steric hindrance between CO or CN^- and the distal helix, if the

locations of both the protein and heme remain unchanged; the oxygen atom of CO or the nitrogen atom of CN^- would collide with Gly-139 O (2.0 Å). To avoid such steric hindrance, the heme and its ligands shift along the α-γ axis of the heme, and the distal F-helix shifts in the opposite direction. These shifts accompany the G-helix shift. Such structural changes disrupt the salt bridge between the heme and protein in heme-HO (Figure 5-4). Most likely gross structural change is induced by ligands such as CO which coordinates to the heme in HO in a tilt manner, as shown in Figure 5-5.

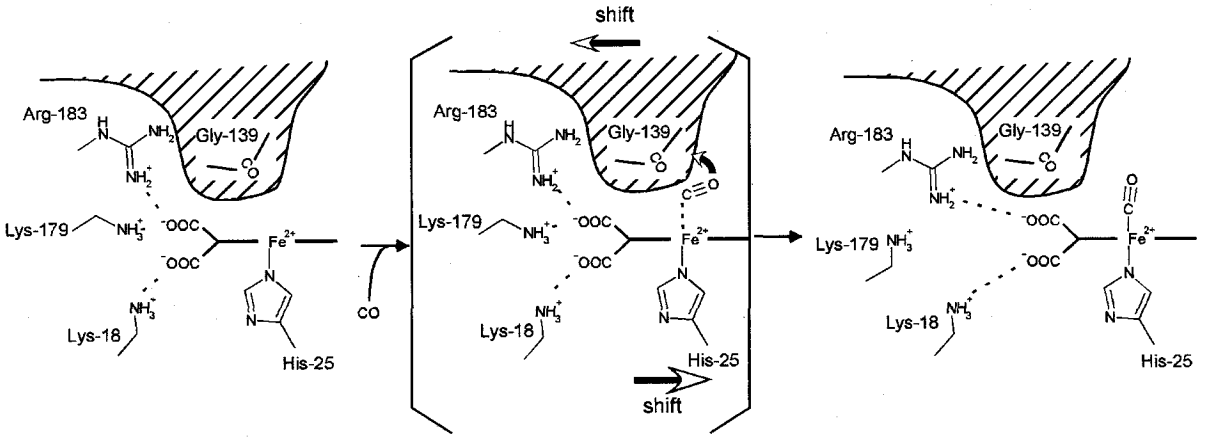

Figure 5-5. **Possible model for CO binding to the heme iron.**

Recent NMR studies of the CN^- bound forms of human HO in complexes with heme (105) and its symmetric derivative (107) show that the central portion of the distal helix is closer to the heme in the solution structure than it is in the crystal structure of human heme-HO, with the position in solution more closely resembling that in the crystal structure of rat heme-HO. The likely movement of the distal helix by ~0.5 Å closer to the heme iron (107) is consistent with a difference in the positions of the distal helix of the crystal structures of rat and human HOs. The distance between Gly-143 N and the heme iron is 4.9 Å in rat CN^--heme-HO in this study, whereas the distances in the two molecules of human heme-HO in an asymmetric unit (40) are 5.3 and 6.0 Å. NMR studies also show that the four-ring aromatic cluster (Tyr-58, Tyr-137, Phe-166, and Phe-167) moves closer to the heme, but no

rearrangement of the aromatic cluster occurs in rat heme-HO on the binding of various ligands, including CN^-.

Unlike CO and CN^-, NO coordinates to the heme iron in bent geometry in NO-heme-HO as does N_3^- in N_3^--heme-HO (39). NO binding to heme-HO causes no significant change in the conformation of the heme binding site or in the heme position. As to the Fe·· N-O angles in the model heme compounds, there are three types depending on the number of metal d-electrons plus the electron in the π^* orbitals of NO (108,109); ~180° in 6 (ferric heme-NO), ~140° in 7 (ferrous heme-NO), and ~120° in 8. In NO-heme-HO, as in NO-bound Mb (108,109), NO is more bent compared to the ideal geometry, indicative of increased π-bonding between the heme iron and NO. O_2 also prefers a bent geometry; a previous RR study of the oxy heme-HO revealed that bound O_2 assumes a bent geometry with an Fe·· O-O angle of ~110° (50). NO-heme-HO, as well as N_3^--heme-HO, therefore, would be a suitable analog for examining the binding mode of O_2 and molecular oxygen activation in the HO reaction. On account of the α-*meso* orientation of NO, the oxygen atom of NO is in close contact with the α-*meso* carbon (3.5 Å), suggesting that the distal oxygen atom of hydrogen peroxide, the active oxygen species for α-*meso* hydroxylation, can easily attack the α-*meso* carbon directly.

Generally, the main factors regulating the CO and O_2 affinities of a hemoprotein are the shape of heme pocket (steric hindrance), hydrogen bonds, and polarity of the heme pocket (110). Studies for O_2 and CO bindings to heme analogs to evaluate these three effects have shown that steric hindrance that bends the Fe·· CO bond decreases the binding affinity for CO whereas the affinity for O_2 is unaffected. Hydrogen bonding to the distal ligand and the polarity in the heme pocket, however, increase the binding affinity for O_2 whereas the affinity for CO is unaffected (110). In the case of HO, strict discrimination between O_2 and CO is mainly brought about by an increase in O_2 affinity that is characterized by a remarkably slow

O_2 dissociation rate constant (35). Comparison of the distal environments of the CO- and NO-bound forms clearly shows that the hydrogen bond between Gly-143 N and NO is present in a bent geometry but such interaction is no longer seen in the tilt geometry (Figure 5-6). Although the biochemical data for the affinity for NO of ferrous heme-HO are not available, its affinity of ferric heme-HO was reported to be higher than that of met Mb (111). The binding affinity of NO to the iron atom of hemoproteins is generally much higher in the ferrous state than in the ferric state (112,113). In addition, NO binding is stabilized by the hydrogen bond to water (Figure 5-3c). Its affinity of ferrous heme-HO would be greater than that of Mb. Because of the highly bent structure for O_2 coordination, Gly-143 N would form a hydrogen bond with the iron-bound oxygen atom of O_2, which would stabilize O_2 coordination to the heme iron thereby decreasing the O_2 dissociation rate constant.

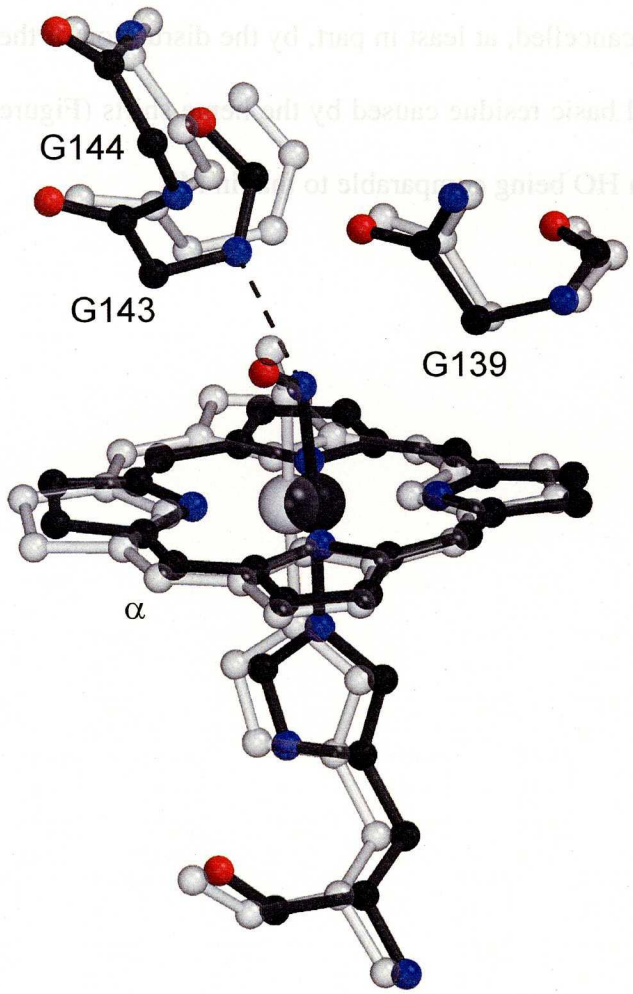

Figure 5-6. **Superimposition of the heme distal sides of CO-heme-HO and NO-heme-HO.** Ball and stick model for heme, ligands, Gly-139, Gly-143, and Gly-144 of NO-heme-HO (carbon and iron are black, nitrogen is blue, and oxygen is red) is superimposed on that of CO-heme-HO (transparent light gray). The dashed line indicates the hydrogen bond between Gly 143 N and the nitrogen atom of NO in NO-heme-HO. The porphyrin substituents are omitted for clarity. The figure was prepared with MOLSCRIPT (125) and RASTER3D (126).

Consequently, I conclude that it is the hydrogen-bonding of Gly-143 N with O_2 which primarily controls ligand discrimination by HO.

Moreover, a series of polar interactions may increase the binding affinity for O_2 of HO. Gly-139 O and Gly-144 N are in van der Waals contact with the ligands in both coordination geometries, indicative that these polar groups may exert a preference for a polar O_2 as compared to an apolar CO. One of the ordered water molecules in the distal hydrogen-bonding network is also located within 3 Å of the distal ligands in both geometries. This hydrophilic network has the ability to donate hydrogen to the heme ligand and has been speculated to be essential for catalyzing hydroxylation of the α-*meso* position of heme (39,81,82). Probably, the polarity of this network also contributes to increase the binding affinity for O_2 in heme-HO. For tilt-type ligands such as CO, however, the stabilization gained by the hydrogen bond between the terminal atom of the ligand and one of the water molecules in the conserved network may be cancelled, at least in part, by the disruption of the salt bridge between the heme propionate and basic residue caused by the heme shifts (Figure 5-4). This may result in the affinity for CO in HO being comparable to that in Mb.

2.2 Two cyanide binding modes in heme-HO

ABSTRACT

As described in the previous section, HO have structural devices to discriminate between O_2 and CO. That is, the structure of HO hemepocket is unfavorable to the ligand binding in tilt-mode. The structure drastically changes depending on the ligand binding modes. Cyanide, as CO, generally binds to the heme iron in tilt-mode. Indeed, at alkaline pH, cyanide binds to heme-HO in tilt-mode as shown in the previous section. However, I demonstrate here that bent-binding mode of cyanide was observed in heme-HO crystal at neutral pH. In this case, neither structural change of the protein nor the heme shift was observed on cyanide binding. This novel cyanide binding mode have not been observed in other ferric hemoproteins to my knowledge. RR spectrum of these crystals and X-ray crystallography illuminating by red laser at cryogenic temperature showed that cyanide bound to heme-HO in bent-mode is readily photolyzed. These results suggest that unstabilization to adopt bent-binding of cyanide in heme-HO is nearly equal to that to disrupt the interactions between the propionate groups of heme and basic residues of HO.

MATERIALS AND METHODS

Crystallographic analysis of CN^--heme-HO. CN^--heme-HO was crystallized as described in the section 2.1 (114). CN^--heme-HO crystals at several pHs were prepared by soaking co-crystallized CN^--heme-HO for a few minutes in each solutions; 5 mM KCN; crystallization solution (4 M sodium formate, 5 mM potassium cyanide, and 50 mM potassium phosphate (pH 6.8)), 10 mM KCN; crystallization solution containing 10 mM potassium cyanide, 20 mM KCN; crystallization solution containing 20 mM potassium cyanide, 40 mM KCN; crystallization solution containing 40 mM potassium cyanide, 50 mM KCN; crystallization solution containing 50 mM potassium cyanide, 5 mM KCN (pH 9.7); crystallization solution replaced potassium phosphate by sodium borate (pH 9.7).

Diffraction data for CN^--heme-HO crystals at several pHs were collected using synchrotron radiation (λ = 0.750 Å) at 100K at the beamline BL41XU, SPring-8 and a MarCCD detector. The distance between the crystal and CCD was 170 mm. To cover wide range of diffraction intensities, two datasets were collected from one crystal within total oscillation angle of 120°; one was collected by oscillating the crystal by 1.5° per frame and the other by 3.0° per frame with attenuated X-ray dose. Diffraction data for CN^--heme-HO crystals in the dark and under illumination by red laser were collected using synchrotron radiation (λ = 1.000 Å) at ~35 K using an open flow He cryostat (115) at the beamline BL44B2 of SPring-8 and a MarCCD detector. For the data collection under illumination, crystal was continuously illuminated for 10 min before and during the data collection by red light produced by a He-Ne laser (15 mW, 632.8 nm; Melles Griot, Irvine, CA). The distance between the crystal and CCD was 130 mm. The crystal was oscillated by 1.5° per frame, total measurement angle of 90°. To increase the signal-to-noise ratio of difference Fourier map, the datasets for CN^--heme-HO in the dark and under illumination were collected from the same crystal under the same conditions. Diffraction data were processed, merged, and scaled with

HKL2000 (77). The model refinements of CN^--heme-HO (pH 6.8) were performed with the program CNS (60). Difference Fourier maps between in the dark and under illumination were calculated using CCP4 suite (57). Diffraction statistics, and refinement statistics are given in Table 6.

RR spectrum. RR scattering was excited at 423.0 nm. The 423.0 nm beam was obtained by doubling the Ti-sapphire laser output at 846.0 nm (repetition rate; 82 MHz, pulse width; 130 fs) with a $KNbO_3$ crystal thermostated at –11 °C. Raman scattering was dispersed by a single polychromator (Ritsu Oyo Kogaku MC-100DG, with a focal length of 1000 mm) and detected by an intensified photodiode array (Princeton Applied Research HQ-1421B). A cylindrical spinning cell (1200 rpm) with an inner diameter of 3 mm was used to avoid local heating of the solution samples. The laser power at the cell was 1.0 mW. A homemade confocal microscopic device was used to crystalline samples. To avoid local heating of the crystalline samples, sample was cooled with the N_2 gas stream through liquid N_2.

Table 6 Summary of crystallographic statistics of CN^--heme-HO

	CN^--heme-HO (pH 6.8)	Photolysis of CN^--heme-HO (pH 6.8)		Photolysis of CN^--heme-HO (pH 9.7)	
Diffraction statistics		In the dark	Laser on	In the dark	Laser on
Resolution range (Å)	50.0 -1.85	20.0-2.0		20.0-2.0	
No. of observations	215,344	108,693	107,876	97,643	92,256
No. of unique reflections	25,213	19,018	19,152	18,922	18,744
Redundancy	8.5	5.7	5.6	5.2	4.9
Completeness (%)*	95.7 (89.3)	92.3 (87.2)	92.8 (92.2)	91.1 (86.9)	90.2 (84.3)
Mean I_o/σ	15.6	13.8	13.4	15.3	17.4
R_{sym} †, *	0.046 (0.335)	0.080 (0.423)	0.083 (0.417)	0.060 (0.400)	0.061 (0.420)
Refinement statistics					
R/R_{free} ††	0.194/0.218	-	-	-	-
Rms deviations from ideality					
bond lengths (Å)	0.006	-	-	-	-
Angles (deg)	1.138	-	-	-	-

† $R_{sym} = \Sigma_{hkl}\Sigma_i |I_i(hkl) - \langle I(hkl)\rangle| / \Sigma_{hkl}\Sigma_i I_i(hkl)$, $\langle I(hkl)\rangle$ is the mean intensity for multiple recorded reflections.

†† $R = \Sigma|F_{obs}(hkl) - F_{calc}(hkl)| / \Sigma|F_{obs}(hkl)|$.

Each R_{free} is the R value calculated for ten percent of the dataset not included in the refinement.

* Values in parentheses are for the outermost shell.

RESULTS AND DISCUSSION

The bent- and tilt-binding modes of cyanide were observed in the crystal depending on the solution conditions as shown in Figure 6-1. The structure of CN^--heme-HO in bent-mode was similar to that of NO-heme-HO where structural shift does not occur, whereas that in tilt-mode was similar to that of CO-heme-HO where structural shift occurs as described in section 2.1. (114). Tilt-binding of cyanide was observed in the KCN concentration of 20-50

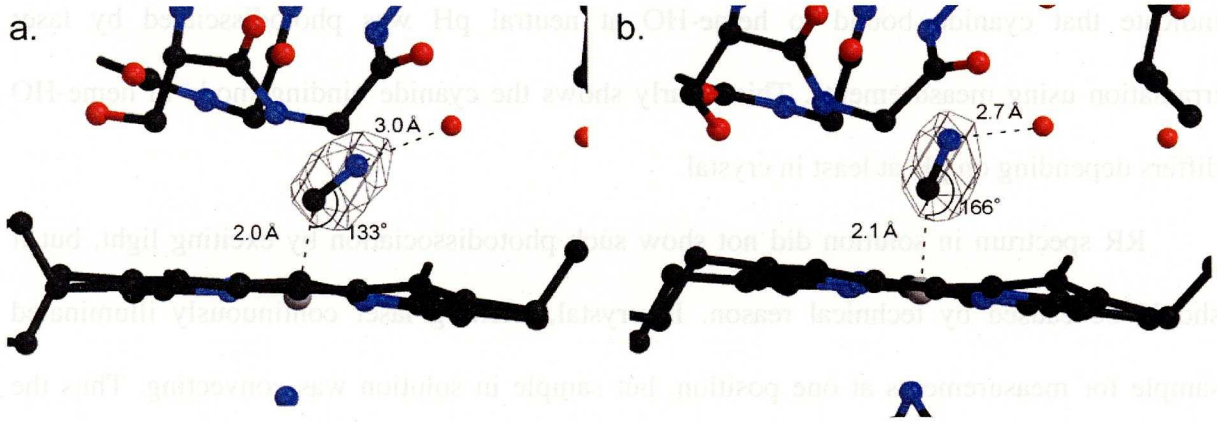

Figure 6-1. **Two different binding modes of cyanide binding in HO. F_o-F_c map omitting distal ligand is superimposed on the ball-and-stick model around heme.** a; Bent binding mode: 5 mM cyanide and pH 6.8. b; Tilt binding mode: 50 mM cyanide and pH 9.7. These figures were prepared with MOLSCRIPT (125), CONSCRIPT (127), and RASTER3D (126).

mM and pH 7.8-9.7, while bent binding was observed in the KCN concentration of 5-10 mM and pH 6.8-7.1. This difference of binding mode would be caused by pH because tilt-binding of cyanide was also observed only when pH was changed to alkaline (pH 9.7). Although determination of the bending angle of distal ligand requires more precise analysis at higher resolution, in heme-HO, two ligand binding modes are clearly determined because it is coupled to the structural change. Tilt-bindng mode of cyanide in solution based on NMR analysis (pH 8.0) is consistent to this result (105,107).

Two ligand binding modes of cyanide in heme-HO were proved by X-ray analysis as shown in the previous paragraph, however, it was not proved that this is also occurred in solution. To study further the two alternative modes of cyanide binding, I measured the high-frequency RR spectrum for CN^--heme-HO both in solution and in crystal. In result, there is no significant difference depending on pH in solution (Figure 6-2 (A)-(F)), whereas drastic difference was observed in crystal depending on pH (Figure 6-2 (G)-(I)). RR spectrum in crystal at alkaline pH was similar to that in solution, but in neutral pH, the spectrum is similar to that of ferric heme-HO solution (29,104). Features of RR spectrum in crystal would

indicate that cyanide bound to heme-HO at neutral pH was photodissciated by laser irradiation using measurements. This clearly shows the cyanide binding mode in heme-HO differs depending on pH at least in crystal.

RR spectrum in solution did not show such photodissociation by exciting light, but it should be caused by technical reason. In crystal, exciting laser continuously illuminated sample for measurements at one position, but sample in solution was convecting. Thus the dose of laser irradiation to the sample for the measurement of RR in crystal was markedly greater than that in solution. In addition, it would be conceivable that two cyanide binding modes could not detect in this RR measurements in solution because RR spectrum in the high-frequency region does not directly reflect the coordination bonds between cyanide and heme iron. RR spectrum in the low-frequency region, which directly reflect the coordination bonds, is required for further study in solution.

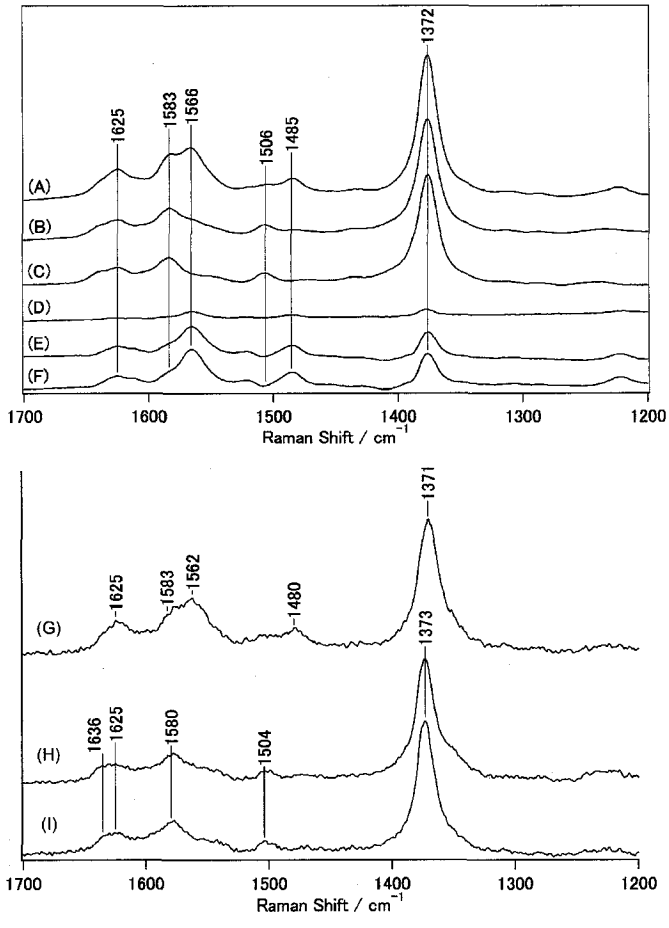

Figure 6-2. **RR spectrum in solutions and crystals.** (A)-(F) are in solutions and (G)-(I) are in crystals. (A): ferric heme-HO, (B): 100 μM KCN (pH 6.8), (C): 50 mM KCN (pH 9.7), (D): (B)-(C), (E): (A)-(B), (F): (A)-(C), (G): 5 mM KCN (pH 6.8), (H): 5 mM KCN (pH 9.7), (I): 50 mM KCN (pH 9.7).

To check that RR spectrum of CN^--heme-HO crystal at neutral pH resembles the photolysis of CN^--heme-HO, I collected the X-ray diffraction data in the dark and under laser illumination. Difference Fourier maps (Figure 6-3) clearly show that cyanide at the distal side of heme at neutral pH was dissociated from heme iron by laser irradiation but not dissociated at alkaline pH under the same experimental conditions. Although the wavelengths of exciting light in RR and X-ray experiments differ, it was shown that cyanide bound to heme iron in bent-mode is readily dissociated by laser irradiation. This indicates that the Fe-CN^- bond of bent-mode is weaker than that of tilt-mode.

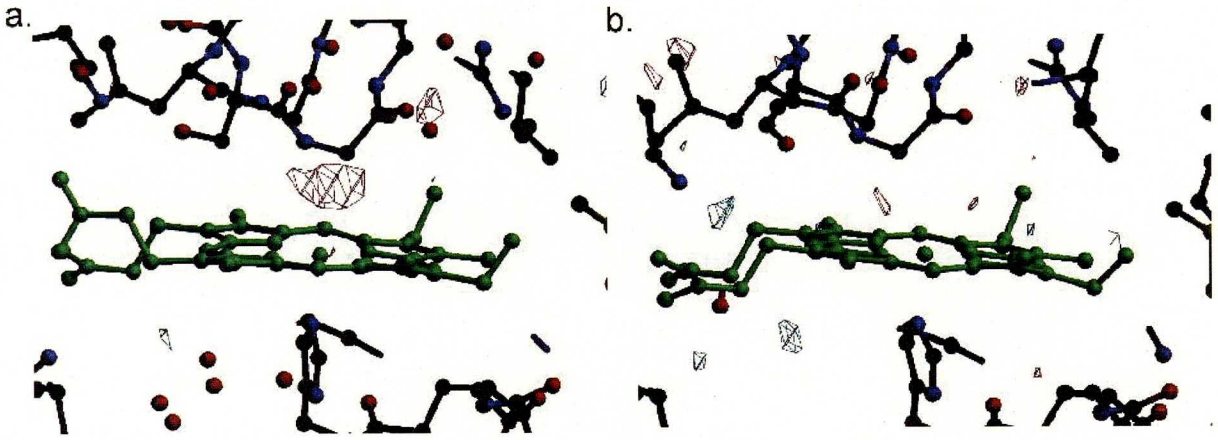

Figure 6-3. **Photo-dissociation of CN^--heme-HO in crystal.** Difference Fourier map calculated between two datasets, in the dark and continuously illuminating by red laser, is superimposed on the ball-and-stick model around heme. Heme is colored green and cyanide model is not included. Positive and negative densities indicate the densities that were increased and decreased, respectively, upon laser irradiation. (red; contoured at -3σ, blue; +3σ). a; 5 mM KCN, pH 6.8, b; 50 mM KCN, pH 9.7. This figure was prepared with MOLSCRIPT (125), CONSCRIPT (127), and RASTER3D (126).

These results indicate that there are two binding modes of cyanide in heme-HO depending on pH at least in the crystal. Unstable bent-binding of cyanide would be forced by the steric hindrance between the distal helix and cyanide. This indicates that the structural change, which occurs in the tilt-binding mode, needs to overcome the energy barrier. Energy to force the bent-binding of cyanide and that to cause the structural change of the heme and distal helix would be nearly equivalent. One reason why the binding-modes of cyanide are

dependent on pH may be that the basic residues in HO and the propionate groups of heme may change their protonated states depending on pH. That is, the change of protonation of these groups may change the strength of the salt-bridges between the propionate group of heme and the basic residues.

2.3 Trapping sites of endogenous carbon monoxide in HO revealed by the photodissociation of ferrous heme-HO bound to carbon monoxide

ABSTRACT

Heme oxygenase (HO) catalyzes physiological heme degradation using O_2 and reducing equivalents to produce biliverdin, iron, and CO. Notably the HO reaction proceeds without product inhibition by CO, which is generated in the conversion of α-hydroxyheme to verdoheme, although CO is known to be a potent inhibitor for HO as for other hemoproteins. In order to probe how the endogenous CO is released from the reaction site, I collected X-ray diffraction data of the crystal of the CO bound form of the ferrous heme-HO complex in the dark and under illumination by red laser at ~35 K. The difference Fourier map indicates that the CO ligand is partially dissociated from the heme by laser irradiation and that CO is trapped in a hydrophobic cavity adjacent to the heme pocket. Taking much weaker affinity of CO for the ferrous verdoheme-HO complex compared to that for the ferrous heme complex into consideration, the CO derived from α-hydroxyheme would be preferentially trapped in the hydrophobic cavity but not coordinated to the iron of verdoheme. This structural device would ensure a smooth progress of the subsequent reaction step, from verdoheme to biliverdin, which requires O_2 binding to verdoheme.

MATERIALS AND METHODS

X-ray crystallographic analysis of CO-heme-HO in the dark and under illumination. Truncated rat HO-1 (Met-1~Pro-267) was expressed and purified as described in the general introduction (Figure 1-5, (39)). CO-heme-HO crystal was prepared as described in the section 2.1 (39,114). CO-heme-HO crystal was handled with a cryo-loop and cooled with liquid nitrogen. The frozen crystals were stocked in liquid nitrogen until the data collection. Diffraction data of CO-heme-HO in the dark and under illumination were collected as well as that of CN^--heme-HO as described in the previous section. Diffraction data were processed, merged, and scaled with HKL2000 (77). The model of photolyzed intermediate was refined with CNS (60), where positions and orientations of photodissociated CO were fixed. CO occupancies of the photolyzed CO-heme-HO were estimated by this difference Fourier map, F_o-F_c map, and refinement where CO occupancies were varied with fixing the temperature factors of CO at reasonable values (25 $Å^2$ for CO bound to the heme iron and 40 $Å^2$ for CO at the site-1 and site-2). The model was refined with the program CNS and CCP4 suite (57). The volumes of the solvent-accessible distal pocket were calculated using the program VOIDOO (116), whereby the probe radius used was 1.4 Å. Crystallographic data, diffraction statistics, and refinement statistics are given in Table 7.

Molecular dynamics simulation. Diffusion pathway of the dissociated CO was simulated using the program NAMD (117). Hydrogen atoms were added automatically to the atoms in CO-heme-HO model using the program CNS (60). Water molecules were additionally generated in the model as wrapping whole protein moiety. Total number of atoms using in the simulation was 9,914. After the energy minimization of the model, molecular dynamics simulation was started at 0 K, then warmed up 50 K per ps until the tempature was reached to 300 K. Force field parameters in the program package CNS were applied for protein and water (TIP3). Parameters for heme was slightly modified from those in the

program package CHARMM22 (118) to accommodate the conformation of heme in CO-heme-HO. Electrostatic interactions beyond 12 Å were omitted from the calculations. Simulation was continued by 200 ps.

Table 7 Summary of crystallographic statistics

Crystallographic data		
Crystal system	Trigonal	
Space group	$P3_221$	
Unit cell dimensions (Å)	$a = b = 65.9$, $c = 120.1$	
No. of molecules in an asymmetric unit	1	
Diffraction statistics	In the dark	Laser on
Resolution range (Å)	20-2.0	20-2.0
No. of observations	102,919	102,900
No. of unique reflections	17,807	17,805
Redundancy	5.8	5.8
Completeness (%)*	84.9 (87.2)	84.8 (87.0)
Mean I_o/σ	18.8	18.6
R_{sym} †,*	0.059 (0.350)	0.060 (0.359)
Refinement statistics of the photolyzed CO-heme-HO		
R/R_{free} ‡	0.207/0.239	
Rms deviations from ideality		
bond lengths (Å)	0.007	
angles (deg)	1.20	

† $R_{sym} = \Sigma_{hkl}\Sigma_i |I_i(hkl) - \langle I(hkl)\rangle| / \Sigma_{hkl}\Sigma_i I_i(hkl)$, $\langle I(hkl)\rangle$ is the mean intensity for multiple recorded reflections.

‡ $R = \Sigma|F_{obs}(hkl) - F_{calc}(hkl)| / \Sigma|F_{obs}(hkl)|$.

Each R_{free} is the R value calculated for ten percent of the dataset not included in the refinement.

* Values in parentheses are for the outermost shell (2.07-2.00Å).

RESULTS AND DISCUSSION

CO trapping site. Difference Fourier map for CO-heme-HO between in the dark and under illumination is shown in Figure 7-1. Positive density on the heme distal side indicates the photolysis of CO-heme-HO by laser irradiation. On the other hand, negative densities were observed at two sites, one above the pyrrole ring of heme (site-1) and another at the hydrophobic cavity adjacent to the heme pocket (site-2). The negative densities in the site-1 and site-2 were found at ~5 and ~10 Å apart from the heme iron, respectively. It would be hard to distinguish whether the density at the site-1 originated from CO or from water. However, CO molecules photodissociated from carbonmonoxy Mb (119-123) and Hb (124) are trapped at the corresponding site. Therefore I consider that the density at the site-1 is due to the CO dissociated from CO-heme-HO on photolysis.

Site-2, which is surrounded by such hydrophobic residues as Met-34, Phe-37, Val-50, Met-51, Leu-54, Leu-147, and Phe-167 (Figure 7-1b), is conserved in the structures of human HO-1 (40,76), *Corynebacterium diphtheriae* HO (HmuO) (PDB ID; 1IW0), but not in the structure of *Neisseria meningitidis* HO (HemO) (41). Rat and human HO-1s and HmuO have a large solvent-accessible distal pocket (Figure 7-2) (44.9 $Å^3$ for rat HO-1, 43.6~59.7 $Å^3$ for human HO-1, 23.2~27.6 $Å^3$ for HmuO), in contrast, that of HemO is very narrow (7.5 $Å^3$). The slightly elongated shape of the density at the site-2 (Figure 7-1b) suggests that it is derived from CO. Although the possibility that water is bound to site-2 cannot be excluded based on the difference map at this resolution, it would be unlikely because of the high hydrophobicity of the site. Moreover, no such density was observed at site-2 in a similar experiment conducted with a crystal of heme-HO bound to CN^- (pH 6.8), although CN^- was photodissociated by laser irradiation (Figure 7-3). This finding suggests that the molecular species occupying site-2 in CO-heme-HO is itself hydrophobic. A series of similar experiments with Mb and Hb (119-124) have confirmed that CO dissociated upon photolysis

is temporarily trapped in the hydrophobic cavity, consistent with our findings with CO-heme-HO. The possibility that the CO generated in the HO reaction escapes into the inner hydrophobic chamber has been raised in the analysis conducted with human heme-HO (40). Thus, we conclude that the photodissociated CO is temporarily trapped in site-2. The present study has reveled that CO dissociated upon irradiation with laser light is trapped at site-2, major site, and site-1, minor site. Our preliminary estimate of CO occupancies showed that about 15% of CO bound to the heme iron was dissociated from heme-HO by laser irradiation and that about 5% and 10% of CO were trapped at site-1 and site-2, respectively.

Site-1 may indicate the travelling pathway to the site-2 of the CO released from CO-heme-HO or the CO formed in the HO reaction. However, trapping CO at the site-2 needs that apolar CO goes through the space occupyied by water molecules forming the rigid hydrogen bonding network, which may need to overcome the large energy barrier. To verify this process, I carried out the molecular dynamics simulation of CO migration in the hemepocket of heme-HO. Predicted pathway of CO in hemepocket was consistent to the CO trapping at site-2 (Figure 7-4); CO reached to the site-2 and trapped.

Trapping CO at site-2 would free from inhibition of O_2 incorporation by CO in the conversion step of verdoheme to biliverdin IXα (Figure 1-3). When iron and biliverdin are released from HO, CO would be readily released from site-2; in the case of rat HO-1, site-2 in the apo state is fully exposed to solvent (90). The affinity of CO for verdoheme-HO is 10,000 times weaker than that for heme-HO (35). Thus, conceivably, binding of the endogenously produced CO to verdoheme-HO would be retarded by trapping CO at site-2.

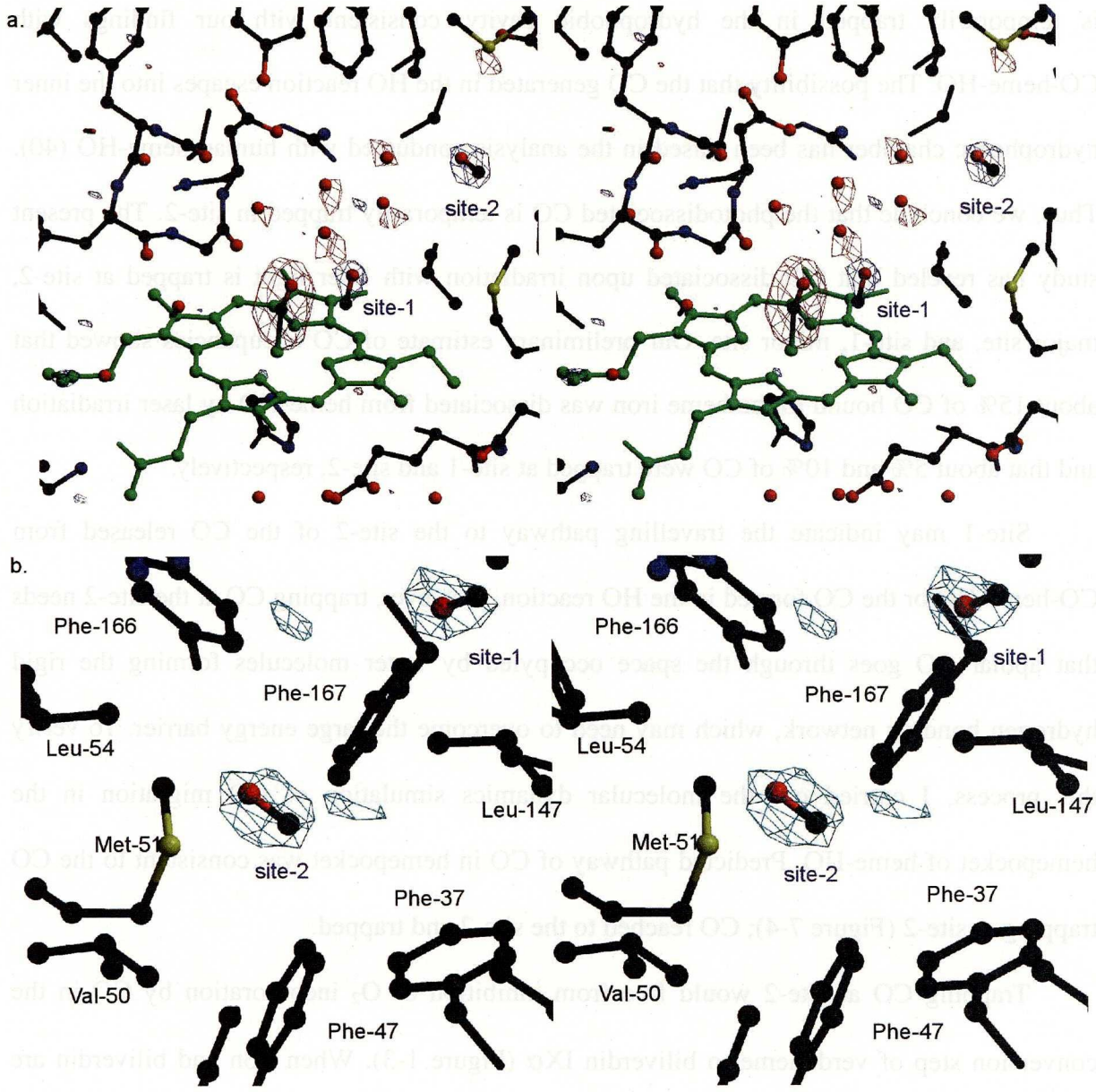

Figure 7-1. **Stereoviews of the difference Fourier map of CO-heme-HO between the dark and laser light-irradiated conditions.** a. The difference Fourier map (red; -3.5σ, blue; +3.5σ) is superimposed on the ball-and-stick model. Heme is colored green for clarity. Positive and negative densities indicate the densities that were increased and decreased, respectively, upon laser irradiation. b. The difference Fourier map (cyan; -3.0σ) is superimposed on the ball-and-stick model around site-2. Only the protein side-chains are shown for clarity. These figures were prepared with MOLSCRIPT (125), CONSCRIPT (127), and RASTER3D (126).

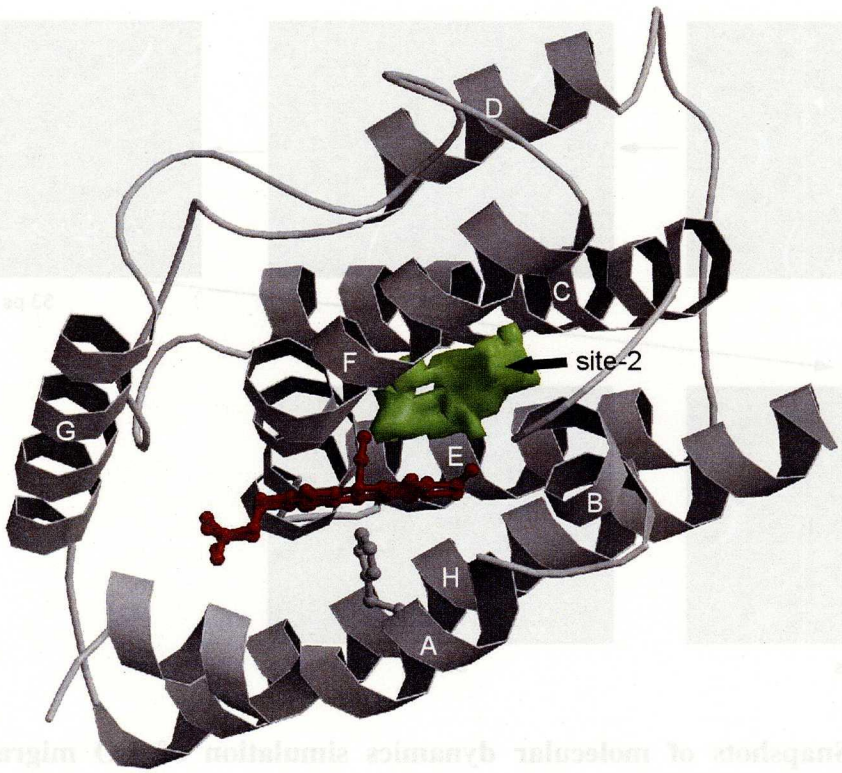

Figure 7-2. **Solvent-accessible cavity of rat CO-heme-HO.** The solvent-accessible cavity on the distal side of the heme moeity is superimposed on the ribbon diagram of rat CO-heme-HO. The letters indicate the appropriate helices in rat heme-HO. Heme and axial ligands are shown as ball-and-stick models. The accessible cavity is colored green. This figure was prepared with MOLSCRIPT (125), CONSCRIPT (127), and RASTER3D (126).

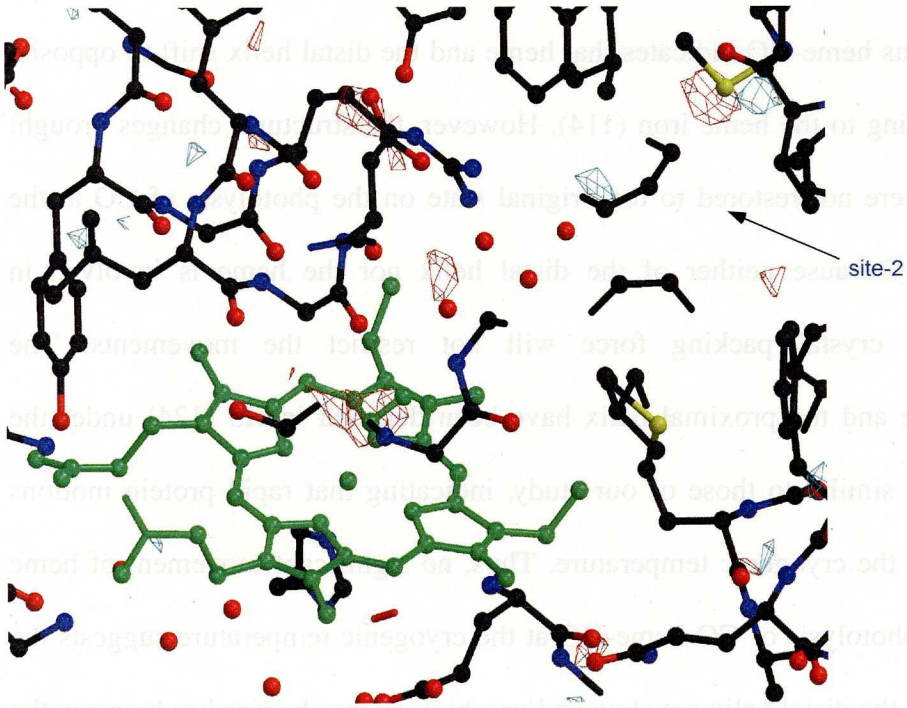

Figure 7-3. **The difference Fourier map of CN^--heme-HO between the dark and laser light-irradiated conditions.** Represantation method of this figure is same to that of figure 7-1a. Red density on the heme iron indicates the photolysis of CN^--heme-HO, while no siginificant density was appeared at the site-2. These figures were prepared with MOLSCRIPT (125), CONSCRIPT (127), and RASTER3D (126).

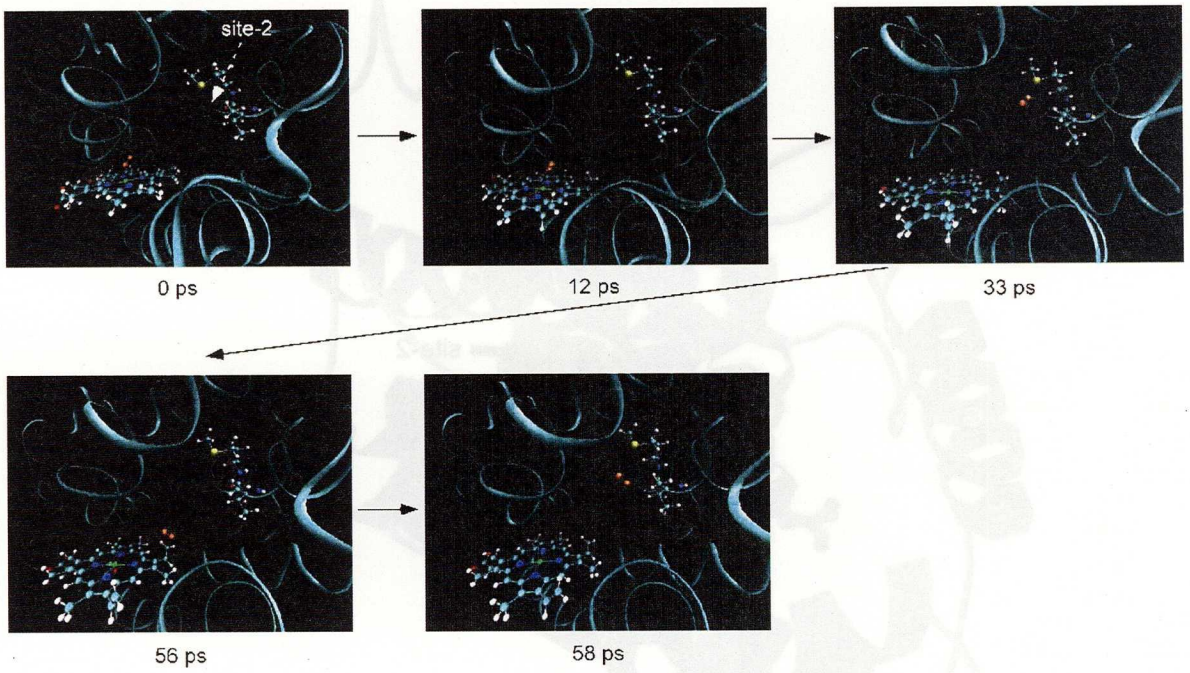

Figure 7-4. **Snapshots of molecular dynamics simulation of CO migration.** Heme, Met-51, Val-50, and CO (orange) were shown in ball-and-stick model. Other moiety was shown in ribbon diagram. After 33 ps from starting the simulation, CO was diffused and trapped in the site-2. Sometimes CO came back near the heme, but almost all times in the simulation CO was trapped in the site-2. This figure was prepared with VMD (130).

Protein and water motions on the photolysis of CO. Structural comparison of CO-heme-HO and ferrous heme-HO indicates that heme and the distal helix shift to opposite direction upon CO binding to the heme iron (114). However, the structural changes brought about by CO binding were not restored to the original state on the photolysis of CO at the cryogenic temperature. Because neither of the distal helix nor the heme is involved in intermolecular contact, crystal packing force will not restrict the movements. The rearrangements of heme and the proximal helix have been detected in Hb (124) under the experimental conditions similar to those of our study, indicating that rapid protein motions can be detected even in the cryogenic temperature. Thus, no significant movement of heme and distal helix on the photolysis of CO-heme-HO at the cryogenic temperature suggests the movements of heme and the distal helix are slow and/or a high-energy barrier lies between the two structures. Indeed, the diffraction data re-measured for the photolyzed crystal stocked in

liquid nitrogen for four months showed the heme iron shifted to the corresponding site in ferrous heme-HO.

On the other hand, water molecules involved in hydrogen bond network, which is considered to be the proton pathway to activate molecular oxygen bound to heme iron, were slightly fluctuated judged from the positive densities observed at the water sites in the difference Fourier map (Figure 7-1a). This could be interpreted as a result of disruption of the hydrogen bond between the oxygen atom of CO and one water molecule upon dissociation of CO from the heme. Similar fluctuation of the water molecules is observed in ferrous heme-HO, wherein the distal ligand of the heme is absent (114).

2.4 Conclusions

The structures of various ligand bound forms of heme-HO complexes demonstrate the structural basis for the discrimination of O_2 against CO in HO. Inherently, CO prefers tilt-binding to the heme iron and O_2 prefers bent-binding. Narrowness of HO hemepocket , which is essential for regiospecific reaction of HO, would cause the steric hindrance of CO binding but not O_2 binding. On CO binding to heme-HO, this hindrance is avoided by heme and distal helix shifts. However, this structural change is accompanied with the disruption of the salt-bridge stabilizing heme position. In addition, O_2 binding would be stabilized by two hydrogen bonds, contributed by the amide group of Gly-143 and water, whereas only one water molecule is hydrogen-bonded to CO bound to the heme. In addition, the polar nature of HO hemepocket would increase the O_2 affinity. The alternative cyanide binding mode depending on pH may indicate that the energy loss of the heme and distal helix shifts is comparable to that of the bent-binding of cyanide. The static discrimination between O_2 and CO in HO is achieved by the binding mode difference between O_2 and CO.

Moreover, the cryo-trapped structure of the photolysis of CO-heme-HO has shown that CO dissociated by laser irradiation is trapped in the hydrophobic cavity which is located 10 Å from the heme iron. The CO trapping would retard CO binding to verdoheme and facilitate O_2 binding which is indispensable for the conversion step of verdoheme to biliverdin IXα. Dynamic discrimination between O_2 and CO in HO is accomplished by the difference of hydrophobicity between O_2 and CO. These two mechanisms explain how HO escapes from the product inhibition by CO.

References

1. Tenhunen, R., Marver, H. S., and Schmid, R. (1968) *Proc. Natl. Acad. Sci. U S A* **61**, 748-755.
2. Tenhunen, R., Marver, H. S., and Schmid, R. (1969) *J. Biol. Chem.* **244**, 6388-6394.
3. Wagener, F. A., Volk, H. D., Willis, D., Abraham, N. G., Soares, M. P., Adema, G. J., and Figdor, C. G. (2003) *Pharmacol. Rev.* **55**, 551-571.
4. Ishikawa, K., Takeuchi, N., Takahashi, S., Matera, K. M., Sato, M., Shibahara, S., Rousseau, D. L., Ikeda-Saito, M., and Yoshida, T. (1995) *J. Biol. Chem.* **270**, 6345-6350.
5. Abraham, N. G., Drummond, G. S., Lutton, J. D., and Kappas, A. (1996) *Cell. Physiol. Biochem.* **6**, 129-168.
6. Ryter, S. W., and Tyrrell, R. M. (2000) *Free Radic. Biol. Med.* **28**, 289-309.
7. Yachie, A., Niida, Y., Wada, T., Igarashi, N., Kaneda, H., Toma, T., Ohta, K., Kasahara, Y., and Koizumi, S. (1999) *J. Clin. Invest.* **103**, 129-135.
8. Stocker, R., Yamamoto, Y., McDonagh, A. F., Glazer, A. N., and Ames, B. N. (1987) *Science* **235**, 1043-1046.
9. Wu, T. W., Carey, D., Wu, J., and Sugiyama, H. (1991) *Biochem. Cell. Biol.* **69**, 828-834.
10. Ryter, S. W., Otterbein, L. E., Morse, D., and Choi, A. M. (2002) *Mol. Cell. Biochem.* **234-235**, 249-263.
11. Slebos, D. J., Ryter, S. W., and Choi, A. M. (2003) *Respir. Res.* **4**, 7.
12. Barañano, D. E., and Snyder, S. H. (2001) *Proc. Natl. Acad. Sci. U S A* **98**, 10996-11002.
13. Friebe, A., Schultz, G., and Koesling, D. (1996) *EMBO J.* **15**, 6863-6868.
14. Beale, S. I. (1994) *Ciba Found. Symp.* **180**, 156-168; discussion 168-171.
15. Schmitt, M. P. (1999) *J. Bacteriol.* **181**, 5330-5340.
16. Sono, M., Roach, M. P., Coulter, E. D., and Dawson, J. H. (1996) *Chem. Rev.* **96**, 2841-2888.
17. Wilks, A., and Ortiz de Montellano, P. R. (1993) *J. Biol. Chem.* **268**, 22357-22362.
18. Wilks, A., Torpey, J., and Ortiz de Montellano, P. R. (1994) *J. Biol. Chem.* **269**, 29553-29556.
19. Yoshida, T., Noguchi, M., Kikuchi, G., and Sano, S. (1981) *J. Biochem. (Tokyo)* **90**, 125-131.

20. Matera, K. M., Takahashi, S., Fujii, H., Zhou, H., Ishikawa, K., Yoshimura, T., Rousseau, D. L., Yoshida, T., and Ikeda-Saito, M. (1996) *J. Biol. Chem.* **271**, 6618-6624.

21. Liu, Y., Moenne-Loccoz, P., Loehr, T. M., and Ortiz de Montellano, P. R. (1997) *J. Biol. Chem.* **272**, 6909-6917.

22. Sakamoto, H., Omata, Y., Palmer, G., and Noguchi, M. (1999) *J. Biol. Chem.* **274**, 18196-18200.

23. Migita, C. T., Fujii, H., Mansfield Matera, K., Takahashi, S., Zhou, H., and Yoshida, T. (1999) *Biochim. Biophys. Acta* **1432**, 203-213.

24. Sakamoto, H., Omata, Y., Hayashi, S., Harada, S., Palmer, G., and Noguchi, M. (2002) *Eur. J. Biochem.* **269**, 5231-5239.

25. Yoshida, T., and Kikuchi, G. (1978) *J. Biol. Chem.* **253**, 4230-4236.

26. Yoshida, T., Takahashi, S., and Kikuchi, G. (1974) *J. Biochem. (Tokyo)* **75**, 1187-1191.

27. Rhie, G., and Beale, S. I. (1992) *J. Biol. Chem.* **267**, 16088-16093.

28. Takahashi, S., Wang, J., Rousseau, D. L., Ishikawa, K., Yoshida, T., Host, J. R., and Ikeda-Saito, M. (1994) *J. Biol. Chem.* **269**, 1010-1014.

29. Sun, J., Wilks, A., Ortiz de Montellano, P. R., and Loehr, T. M. (1993) *Biochemistry* **32**, 14151-14157.

30. Hawkins, B. K., Wilks, A., Powers, L. S., Ortiz de Montellano, P. R., and Dawson, J. H. (1996) *Biochim. Biophys. Acta* **1295**, 165-173.

31. Pond, A. E., Roach, M. P., Sono, M., Rux, A. H., Franzen, S., Hu, R., Thomas, M. R., Wilks, A., Dou, Y., Ikeda-Saito, M., Ortiz de Montellano, P. R., Woodruff, W. H., Boxer, S. G., and Dawson, J. H. (1999) *Biochemistry* **38**, 7601-7608.

32. Torpey, J., and Ortiz de Montellano, P. R. (1996) *J. Biol. Chem.* **271**, 26067-26073.

33. Torpey, J., and Ortiz de Montellano, P. R. (1997) *J. Biol. Chem.* **272**, 22008-22014.

34. Springer, B. A., Sligar, S. G., Olson, J. S., and Phillips, G. N., Jr. (1994) *Chem. Rev.* **94**, 699-714.

35. Migita, C. T., Matera, K. M., Ikeda-Saito, M., Olson, J. S., Fujii, H., Yoshimura, T., Zhou, H., and Yoshida, T. (1998) *J. Biol. Chem.* **273**, 945-949.

36. Sugishima, M., Omata, Y., Kakuta, Y., Sakamoto, H., Noguchi, M., and Fukuyama, K. (2000) *FEBS Lett.* **471**, 61-66.

37. Hidaka, T., Omata, Y., and Noguchi, M. (1996) *Kurume Med. J.* **43**, 313-324.

38. Omata, Y., Asada, S., Sakamoto, H., Fukuyama, K., and Noguchi, M. (1998) *Acta*

Crystallogr. Sect. D Biol. Crystallogr. **54**, 1017-1019.

39. Sugishima, M., Sakamoto, H., Higashimoto, Y., Omata, Y., Hayashi, S., Noguchi, M., and Fukuyama, K. (2002) *J. Biol. Chem.* **277**, 45086-45090.
40. Schuller, D. J., Wilks, A., Ortiz de Montellano, P. R., and Poulos, T. L. (1999) *Nat. Struct. Biol.* **6**, 860-867.
41. Schuller, D. J., Zhu, W., Stojiljkovic, I., Wilks, A., and Poulos, T. L. (2001) *Biochemistry* **40**, 11552-11558.
42. Sun, J., Loehr, T. M., Wilks, A., and Ortiz de Montellano, P. R. (1994) *Biochemistry* **33**, 13734-13740.
43. Ito-Maki, M., Ishikawa, K., Matera, K. M., Sato, M., Ikeda-Saito, M., and Yoshida, T. (1995) *Arch. Biochem. Biophys.* **317**, 253-258.
44. Maines, M. D. (1988) *FASEB J.* **2**, 2557-2568.
45. Zhou, H., Migita, C. T., Sato, M., Sun, D., Zhang, X., Ikeda-Saito, M., Fujii, H., and Yoshida, T. (2000) *J. Am. Chem. Soc.* **122**, 8311-8312.
46. Kamtekar, S., and Hecht, M. H. (1995) *FASEB J.* **9**, 1013-1022.
47. Privalov, P. L. (1996) *J. Mol. Biol.* **258**, 707-725.
48. Banci, L., and Presenti, C. (2000) *J. Biol. Inorg. Chem.* **5**, 422-431.
49. Yoshinaga, T., Sudo, Y., and Sano, S. (1990) *Biochem. J.* **270**, 659-664.
50. Takahashi, S., Ishikawa, K., Takeuchi, N., Ikeda-Saito, M., Yoshida, T., and Rousseau, D. L. (1995) *J. Am. Chem. Soc.* **117**, 6002-6006.
51. Yoshida, T., and Kikuchi, G. (1978) *J. Biol. Chem.* **253**, 4224-4229.
52. Maurus, R., Bogumil, R., Nguyen, N. T., Mauk, A. G., and Brayer, G. (1998) *Biochem. J.* **332**, 67-74.
53. Yoshida, T., and Noguchi, M. (1984) *J. Biochem. (Tokyo)* **96**, 563-570.
54. Yoshida, T., and Migita, C. T. (2000) *J. Inorg. Biochem.* **82**, 33-41.
55. Ortiz de Montellano, P. R. (2000) *Curr. Opin. Chem. Biol.* **4**, 221-227.
56. Leslie, A. G. W. (1982). Joint CCP4 + ESF-EAMCB Newsletter on Protein Crystallography, No. 26, Daresbury Laboratory, Warrinton, U.K.
57. The CCP4 suite: programs for protein crystallography. (1994) *Acta Crystallogr. Sect. D Biol. Crystallogr.* **50**, 760-763.
58. Kabsch, W. (1988) *J. Appl. Crystallogr.* **21**, 916-924.
59. Yeates, T. O. (1997) *Methods Enzymol.* **276**, 344-358.
60. Brünger, A. T., Adams, P. D., Clore, G. M., DeLano, W. L., Gros, P., Grosse-Kunstleve, R. W., Jiang, J. S., Kuszewski, J., Nilges, M., Pannu, N. S., Read,

R. J., Rice, L. M., Simonson, T., and Warren, G. L. (1998) *Acta Crystallogr. Sect. D Biol. Crystallogr.* **54**, 905-921.

61. Britton, D. (1972) *Acta Crystallogr. Sect. A Foundations of Crystallogr.* **28**, 296-297
62. Jones, T. A., Zou, J. Y., Cowan, S. W., and Kjeldgaard. (1991) *Acta Crystallogr. Sect. A Foundations of Crystallogr.* **47**, 110-119.
63. Laskowski, R. A., MacArthur, M. W., Moss, D. S., and Thornton, J. M. (1993) *J. Appl. Crystallogr.* **26**, 283-291
64. Chandra, N., Acharya, K. R., and Moody, P. C. (1999) *Acta Crystallogr. Sect. D Biol. Crystallogr.* **55**, 1750-1758.
65. Redinbo, M. R., and Yeates, T. O. (1993) *Acta Crystallogr. Sect. D Biol. Crystallogr.* **49**, 375-380.
66. Luecke, H., Richter, H. T., and Lanyi, J. K. (1998) *Science* **280**, 1934-1937.
67. Zhu, W., Wilks, A., and Stojiljkovic, I. (2000) *J. Bacteriol.* **182**, 6783-6790.
68. Falzone, C. J., Wang, Y., Vu, B. C., Scott, N. L., Bhattacharya, S., and Lecomte, J. T. (2001) *Biochemistry* **40**, 4879-4891.
69. Falzone, C. J., Mayer, M. R., Whiteman, E. L., Moore, C. D., and Lecomte, J. T. (1996) *Biochemistry* **35**, 6519-6526.
70. Feng, Y., Sligar, S. G., and Wand, A. J. (1994) *Nat. Struct. Biol.* **1**, 30-35.
71. Baldwin, R. L. (1991) *Ciba Found. Symp.* **161**, 190-201; discussion 201-205.
72. Eliezer, D., and Wright, P. E. (1996) *J. Mol. Biol.* **263**, 531-538.
73. Nobbs, C. L., Watson, H. C., and Kendrew, J. C. (1966) *Nature* **209**, 339-341.
74. Arnesano, F., Banci, L., Bertini, I., Faraone-Mennella, J., Rosato, A., Barker, P. D., and Fersht, A. R. (1999) *Biochemistry* **38**, 8657-8670.
75. Muskett, F. W., Kelly, G. P., and Whitford, D. (1996) *J. Mol. Biol.* **258**, 172-189.
76. Lad, L., Schuller, D. J., Shimizu, H., Friedman, J., Li, H., Ortiz De Montellano, P. R., and Poulos, T. L. (2002) *J. Biol. Chem.* **278**, 7834-7843.
77. Otwinowski, Z., and Minor, W. (1997) *Methods Enzymol.* **276**, 307-326.
78. McRee, D. E. (1999) *J. Struct. Biol.* **125**, 156-165.
79. Hernandez, G., Wilks, A., Paolesse, R., Smith, K. M., Ortiz de Montellano, P. R., and La Mar, G. N. (1994) *Biochemistry* **33**, 6631-6641.
80. Blumberg, W. D., and Peisach, J. (1971) in *Advances in Chemistry Series* (Dessy, R., ed) Vol. 100, pp. 271-291, American Chemical Society, Washington D.C.
81. Lightning, L. K., Huang, H., Moenne-Loccoz, P., Loehr, T. M., Schuller, D. J., Poulos, T. L., and de Montellano, P. R. (2001) *J. Biol. Chem.* **276**, 10612-10619.

82. Fujii, H., Zhang, X., Tomita, T., Ikeda-Saito, M., and Yoshida, T. (2001) *J. Am. Chem. Soc.* **123**, 6475-6484.

83. Davydov, R. M., Yoshida, T., Ikeda-Saito, M., and Hoffman, B. M. (1999) *J. Am. Chem. Soc.* **121**, 10656-10657

84. Davydov, R., Kofman, V., Fujii, H., Yoshida, T., Ikeda-Saito, M., and Hoffman, B. M. (2002) *J. Am. Chem. Soc.* **124**, 1798-1808.

85. Kleywegt, G. J., and Jones, T. A. (1996) *Structure* **4**, 1395-1400.

86. Sheldrick, W. S. (1976) *J. Chem. Soc. Perkin Trans. 2*, 1457-1462.

87. Balch, A. L., Latos-Grażyński, L., Noll, B. C., Olmstead, M. M., and Safari, N. (1993) *J. Am. Chem. Soc.* **115**, 9056-9061.

88. Wagner, U. G., Müller, N., Schmitzberger, W., Falk, H., and Kratky, C. (1995) *J. Mol. Biol.* **247**, 326-337.

89. Pereira, P. J., Macedo-Ribeiro, S., Párraga, A., Pérez-Luque, R., Cunningham, O., Darcy, K., Mantle, T. J., and Coll, M. (2001) *Nat. Struct. Biol.* **8**, 215-220.

90. Sugishima, M., Sakamoto, H., Kakuta, Y., Omata, Y., Hayashi, S., Noguchi, M., and Fukuyama, K. (2002) *Biochemistry* **41**, 7293-7300.

91. Liu, Y., and Ortiz de Montellano, P. R. (2000) *J. Biol. Chem.* **275**, 5297-5307.

92. Koerner, R., Latos-Grażyński, L., and Balch, A. L. (1998) *J. Am. Chem. Soc.* **120**, 9246-9255.

93. Ortiz de Montellano, P. R., and Wilks, A. (2001) in *Advances in Inorgranic Chemistry* (Sykes, A. G., ed) Vol. 51, pp. 359-407., Academic Press, San Diego.

94. Collman, J. P., Barauman, J. I., Iverson, B. L., Sessler, J. L., Morris, R. M., and Gibson, Q. H. (1983) *J. Am. Chem. Soc.* **105**, 3052-3064.

95. Vojtěchovský, J., Chu, K., Berendzen, J., Sweet, R. M., and Schlichting, I. (1999) *Biophys. J.* **77**, 2153-2174.

96. Phillips, S. E., and Schoenborn, B. P. (1981) *Nature* **292**, 81-82.

97. Cheng, X. D., and Schoenborn, B. P. (1991) *J. Mol. Biol.* **220**, 381-399.

98. Li, T., Quillin, M. L., Phillips, G. N., Jr., and Olson, J. S. (1994) *Biochemistry* **33**, 1433-1446.

99. Bhattacharya, S., Sukits, S. F., MacLaughlin, K. L., and Lecomte, J. T. (1997) *Biophys. J.* **73**, 3230-3240.

100. Phillips, G. N., Jr., Teodoro, M. L., Li, T., Smith, B., and Olson, J. S. (1999) *J. Phys. Chem. B* **103**, 8817-8829.

101. Fujii, H., Dou, Y., Zhou, H., Yoshida, T., and Ikeda-Saito, M. (1998) *J. Am. Chem.*

Soc. **120**, 8251-8252.

102. Yoshida, T., Noguchi, M., and Kikuchi, G. (1980) *J. Biochem. (Tokyo)* **88**, 557-563.

103. Takahashi, S., Matera, K. M., Fujii, H., Zhou, H., Ishikawa, K., Yoshida, T., Ikeda-Saito, M., and Rousseau, D. L. (1997) *Biochemistry* **36**, 1402-1410.

104. Takahashi, S., Wang, J., Rousseau, D. L., Ishikawa, K., Yoshida, T., Takeuchi, N., and Ikeda-Saito, M. (1994) *Biochemistry* **33**, 5531-5538.

105. La Mar, G. N., Asokan, A., Espiritu, B., Yeh, D. C., Auclair, K., and Ortiz De Montellano, P. R. (2001) *J. Biol. Chem.* **276**, 15676-15687.

106. Royer, W. E., Jr., Hendrickson, W. A., and Chiancone, E. (1990) *Science* **249**, 518-521.

107. Li, Y., Syvitski, R. T., Auclair, K., Wilks, A., Ortiz De Montellano, P. R., and La Mar, G. N. (2002) *J. Biol. Chem.* **277**, 33018-33031.

108. Enemark, J. H., and Feltham, R. D. (1974) *Coord. Chem. Rev.* **13**, 339-406.

109. Scheidt, W. R., and Ellison, M. K. (1999) *Acc. Chem. Res.* **32**, 350-359.

110. Momenteau, M., and Reed, C. A. (1994) *Chem. Rev.* **94**, 659-698.

111. Wang, J., Lu, S., Moenne-Loccoz, P., and Ortiz de Montellano, P. R. (2003) *J. Biol. Chem.* **278**, 2341-2347.

112. Moore, E. G., and Gibson, Q. H. (1976) *J. Biol. Chem.* **251**, 2788-2794.

113. Hoshino, M., Laverman, L., and Ford, P. C. (1999) *Coord. Chem. Rev.* **187**, 75-102

114. Sugishima, M., Sakamoto, H., Noguchi, M., and Fukuyama, K. (2003) *Biochemistry* **42**, 9898-9905.

115. Nakasako, M., Sawano, M., and Kawamoto, M. (2002) *Rev. Sci. Instrum.* **73**, 1318-1320.

116. Kleywegt, G. J., and Jones, T. A. (1994) *Acta Crystallogr. Sect. D Biol. Crystallogr.* **50**, 178-185

117. Kalé, L., Skeel, R., Bhandarkar, M., Brunner, R., Gursoy, A., Krawetz, N., Phillips, J., Shinozaki, A., Varadarajan, K., and Schulten, K. (1999) *J. Comp. Phys.* **151**, 283-312.

118. Brooks, B. R., Bruccoleri, R. E., Olafson, B. D., States, D. J., Swaminathan, S., and Karplus, M. (1983) *J. Comp. Chem.* **4**, 187-217.

119. Chu, K., Vojtěchovský, J., McMahon, B. H., Sweet, R. M., Berendzen, J., and Schlichting, I. (2000) *Nature* **403**, 921-923.

120. Schlichting, I., Berendzen, J., Phillips, G. N., Jr., and Sweet, R. M. (1994) *Nature* **371**, 808-812.

121. Hartmann, H., Zinser, S., Komninos, P., Schneider, R. T., Nienhaus, G. U., and Parak, F. (1996) *Proc. Natl. Acad. Sci. U S A* **93**, 7013-7016.

122. Teng, T. Y., Šrajer, V., and Moffat, K. (1994) *Nat. Struct. Biol.* **1**, 701-705.

123. Šrajer, V., Teng, T., Ursby, T., Pradervand, C., Ren, Z., Adachi, S., Schildkamp, W., Bourgeois, D., Wulff, M., and Moffat, K. (1996) *Science* **274**, 1726-1729.

124. Adachi, S., Park, S. Y., Tame, J. R., Shiro, Y., and Shibayama, N. (2003) *Proc. Natl. Acad. Sci. U S A* **100**, 7039-7044.

125. Kraulis, P. J. (1991) *J. Appl. Crystallogr.* **24**, 946-950.

126. Merritt, E. A., and Bacon, D. J. (1997) *Methods Enzymol.* **277**, 505-524.

127. Lawrence, M. C., and Bourke, P. (2000) *J. Appl. Crystallogr.* **33**, 990-991.

128. Nicholls, A., Sharp, K. A., and Honig, B. (1991) *Proteins* **11**, 281-296.

129. Schmidt, M. W., Baldridge, K. K., Boatz, J. A., Elbert, S. T., Gordon, M. S., Jensen, J. H., Koseki, S., Matsunaga, N., Nguyen, K. A., Su, S., Windus, T. L., Dupuis, M., and Montgomery, J. A. (1993) *J. Comp. Chem.* **14**, 1347-1363.

130. Humphrey, W., Dalke, A., and Schulten, K. (1996) *J. Mol. Graph.* **14**, 33-38.

List of publications

Papers related to this thesis

1. Crystal structure of rat heme oxygenase-1 in complex with heme.

   Sugishima, M., Omata, Y., Kakuta, Y., Sakamoto, H., Noguchi, M. & Fukuyama, K. (2000). *FEBS Lett.* **471**(1), 61-66.

2. Crystal structure of rat apo-heme oxygenase-1 (HO-1): mechanism of heme binding in HO-1 inferred from structural comparison of the apo and heme complex forms.

   Sugishima, M., Sakamoto, H., Kakuta, Y., Omata, Y., Hayashi, S., Noguchi, M. & Fukuyama, K. (2002). *Biochemistry* **41**(23), 7293-7300.

3. Structure and reaction mechanism of heme oxygenase-1.

   Sakamoto, H., Sugishima, M., Omata, Y., Kakuta, Y., Fukuyama, K., Palmer, G. & Noguchi, M. (2002) in *International Congress Series* (Ishimura Y., ed.) Vol. 1233, pp. 177-183, Excerpta Medica, Amsterdam.

4. Crystal structure of rat heme oxygenase-1 in complex with heme bound to azide: implication for regiospecific hydroxylation of heme at the α-*meso* carbon.

   Sugishima, M., Sakamoto, H., Higashimoto, Y., Omata, Y., Hayashi, S., Noguchi, M. & Fukuyama, K. (2002). *J. Biol. Chem.* **277**(47), 45086-45090.

5. Crystal structure of rat heme Oxygenase-1 in complex with biliverdin-iron chelate: conformational change of the distal helix during the heme cleavage reaction.

   Sugishima, M., Sakamoto, H., Higashimoto, Y., Noguchi, M. & Fukuyama, K. (2003). *J. Biol. Chem.* **278**(34), 32352-32358.

6. Crystal structures of ferrous and CO-, CN^--, and NO-bound forms of rat heme oxygenase-1 (HO-1) in complex with heme: structural implications for discrimination between CO and O_2 in HO-1.

   Sugishima, M., Sakamoto, H., Noguchi, M. & Fukuyama, K. (2003). *Biochemistry* **42**(33), 9898-9905.

7. CO trapping site in heme oxygenase revealed by photolysis of its CO-bound heme complex: Mechanism of escaping from the product inhibition.

   Sugishima, M., Sakamoto, H., Noguchi, M. & Fukuyama, K., submitted for publication.

8. Two cyanide binding modes in heme oxygenase.

   Sugishima, M., Oda, K., Ogura, T., Sakamoto, H., Noguchi, M. & Fukuyama, K., in preparation.

Other papers

1. Hydroxyl amine and hydrazine bind directly to the heme iron of the heme-heme oxygenase-1 complex.

   Sakamoto, H., Higashimoto, Y., Hayashi, S., Sugishima, M., Fukuyama, K., Palmer, G. & Noguchi, M., submitted for publication.

2. Crystal structure of novel zinc binding ATP sulfurylase from *Thermus thermophilus* HB8.

   Taguchi, Y.. Sugishima, M. & Fukuyama, K., submitted for publication.

Acknowledgments

I am sincerely greateful to Professor Keiichi Fukuyama (Osaka University) for his supports, encouragement, and fruitful discussions. I also greatly thank to Professor Masato Noguchi, and Drs. Hiroshi Sakamoto and Yuichiro Higashimoto (Kurume University) for their supports, discussions about HO reaction, and ESR measurements of ligand bound forms, Dr. Yoshiaki Omata and Mr. Shunsuke Hayashi (Kurume University) for the construction of the expression vector of HO and NADPH-cytochrome P450 reductase and help for protein purification, Dr. Yoshimitsu Kakuta (Kyusyu University) for his advice on the biochemical and crystallographic work, Professor Takashi Ogura (Himeji Institute of Technology) and Mr. Kenji Oda (Tokyo University) for RR spectroscopy of CN^--heme-HO, Dr. Shin-ichi Adachi (Photon Factory, KEK) for the photolysis techiniques by laser irradiation, and Drs. Masahide Kawamoto, Hisanobu Sakai, Keiko Miura (JASRI), Hisashi Naitow, and Taiji Matsu (RIKEN, Harima) for the synchrotron experiments and microspectrometry of the crystal in SPring-8. And I thank all members of Fukuyama laboratory for their helpful discussions.